CHARACTERIZING EXCITED STATE DYNAMICS AND CARRIER TRANSPORT IN HYBRID ORGANIC-INORGANIC LEAD HALIDE PEROVSKITES VIA ULTRAFAST MICROSCOPY

by

Andrew Hinson Hill

A dissertation submitted in partial fulfillment
of the requirements for the degree

of

Doctor of Philosophy

in

Materials Science

MONTANA STATE UNIVERSITY
Bozeman, Montana

July 2018

DEDICATION

To my family and friends.

ACKNOWLEDGEMENTS

I would be remiss to not first acknowledge my advisor, Dr. Erik Grumstrup, whose counsel and patient tutelage (in matters personal and professional) I am grateful to have received. Members of the Grumstrup research group, past and present, deserve acknowledgement as well. Special thanks are extended to Casey Kennedy and Eric Massaro for years of guidance, companionship, and valuable feedback on all of the manuscripts which make up this dissertation. I also wish to acknowledge Tino Woodburn and Christine Gobrogge, for six years of the best bad advice a friend could ask for.

I would not have made it to graduate school without the timely interventions of several amazing undergraduate professors and mentors. Dr. Diana Cermak insisted I join her synthetic research lab as a sophomore despite earning less than exemplary grades in her undergraduate organic chemistry classes. Time spent in her lab instilled in me the love for research and discovery which propelled me into (and through) graduate school. Dr. Mary Crawford allowed me into her research lab as a junior and showed me that there's more to chemistry than beakers and hot-plates. I owe both Dr. Cermak and Dr. Crawford a debt which I do not imagine ever being able to fully repay.

My family deserves acknowledgement as well for the emotional support they've provided over the last six years. Special thanks to Chester, for refusing to let me give up on myself, to Morgan, for six years of late night phone calls and midnight car rides, and Sean, for a lifetime of friendship and unconditional support. Finally, I wish to thank my parents, without whom none of this would have been possible.

TABLE OF CONTENTS

TABLE OF CONTENTS CONTINUED

LIST OF FIGURES

Figure Page

LIST OF FIGURES CONTINUED

Figure Page

ABSTRACT

Lead tri-halide perovskites have recently emerged as cost-effective alternatives to silicon for use in photovoltaic devices. A large contributor to their reduced cost compared to silicon is the simple solution processed techniques employed in their fabrication. While these methods can produce effective photovoltaic devices, heterogeneity endemic to solution processing makes characterization of tri-halide perovskites a challenging task. Most spectroscopic techniques use large sample interrogation volumes which often results in the indiscriminate sampling of grain boundaries and other heterogeneities which impact the spectroscopic observable. To circumvent this issue, pump-probe microscopy is used to dramatically shrink the sample volume, reducing the contributions from chemical and morphological heterogeneities and providing a more accurate measure of the sample's inherent properties.

This work begins with a study of the recombination and transport dynamics methylammonium lead tri-iodide ($MAPbI_3$) perovskite. After identifying the main recombination pathways and contributions to the transient signal, experimental focus is shifted to the transport properties of $MAPbI_3$. The key contributing factors to the high diffusivities reported in $MAPbI_3$ are found to be strong electron-phonon coupling and a high static dielectric constant which serves to screen carriers from interactions with charged defects and other carriers.

Then the development a new all-optical method capable of uniquely determining the two fundamental parameters that govern carrier transport (the mean scattering time and optical mass of photogenerated carriers) is reported. This method was applied to a series of different perovskite materials including $MAPbI_3$, cesium lead bromide di-iodide ($CsPbBrI_2$), methylammonium lead tri-bromide ($MAPbBr_3$), formamidinium lead tri-bromide ($FAPbBr_3$), and cesium lead tri-bromide ($CsPbBr_3$). The results of these experiments have led to the characterization of the role each perovskite constituent (namely, the identity of the organic cation and the halide stoichiometry) plays in determining the transport properties of the resulting material.

The work presented in this dissertation characterizes the transport properties of lead halide perovskites. Measurements collected across multiple discrete and highly crystalline domains of multiple perovskite species have helped establish a relationship between the functionality and the local structure of these materials. Additionally, the design and first application of a new methodology to disentangle the effects of mean scattering time and the photogenerated carrier mass on carrier transport is reported. This technique will not only continue to aid in the characterization of lead-halide perovskites but will likely also see use on a host of other material systems to advance understanding of carrier transport in a variety of materials.

CHAPTER ONE

INTRODUCTION

1.1 Introductory Remarks

Ultrafast spectroscopy is among the chief methods used to characterize the dynamics of semiconducting materials. This was true as far back as the early-1980's when Shank and Hirlimann worked to characterize the excited state dynamics of single crystalline silicon wafers[1] and it remains true today. While the ubiquity of ultrafast spectroscopy has not changed, the nature of the materials it is used to characterize certainly has. Significant research effort in the past decade across a variety of fields has focused on nanomaterials, which display spatial dimensions on the same order of magnitude (or smaller) as a single wavelength of visible light. Accompanying this increased interest in nanomaterials is a similar escalation of research activity investigating highly spatially heterogeneous materials. In both cases, nano- and microscale structural deformities and chemical heterogeneities have been shown to play significant roles in determining the optical response of the material.[2-9]

The recent growth of the photovoltaic community's interest in lead halide perovskites ($APbX_3$, where A is an organic or inorganic cation and X is any halide anion) is one example of the burgeoning interest in heterogeneous materials. Hybrid organic-inorganic lead halide perovskites were initially discovered to be efficient photovoltaic media by Miyasaka in 2009.[10] In contrast to the canonical photovoltaic material silicon, which requires a significant amount of processing before it can be utilized in a solar cell,

the $MAPbI_3$ and $MAPbBr_3$ (here MA represents the complex organic cation $CH_3NH_3^+$) materials characterized by Miyasaka were prepared by a simple one-step solution deposition process.

Miyasaka's discovery of potential photovoltaic utility of lead halide perovskites marked a promising step towards more cost-effective photovoltaic power. A vast majority of the cost borne by silicon solar cells is tied up in the capital necessary to build the facilities required to process raw silicon ore into silicon of sufficient purity for photovoltaic applications.[11] Assuming lead halide perovskite-based devices could reach a power conversion efficiency (PCE) comparable to silicon (Miyasaka's initial device displayed a PCE of 3.6% compared to silicon's ~22%),[12] they presented a significantly more cost-effective alternative.

Immediately following Miyasaka's work research interest in lead halide perovskites blossomed. The next few years saw a vast amount of research performed on these materials[10, 13-19] in an attempt to characterize their excited state dynamics and identify promising avenues towards optimization of their photovoltaic performance. This research was rewarded in late 2016 by lead halide perovskite based devices displaying power conversion efficiencies upwards of 20%[12] along with promising advances towards their use in a wide range of optoelectronic applications.[20-22]

Despite these promising advances it is clear that the solution processed methods by which lead halide perovskites are typically synthesized play a large role in determining their functionality. Typical synthesis protocols involved a single precursor solution that was spin-coated and annealed into a heterogeneous thin film. This endemic

heterogeneity makes these materials inherently difficult to analyze with traditional spectroscopies, which employ large sample interrogation volumes to generate an experimental observable. The size of their interrogation volumes leads these spectroscopies to average over a significant number of structural and chemical heterogeneities left behind by the relatively "quick-and-dirty" synthetic protocols used to manufacture lead halide perovskites.

These difficulties become apparent when analyzing the perovskite literature. Reported values for benchmark semiconductor properties including carrier diffusion length,[13, 16, 23] exciton binding energies,[24-25] carrier diffusion constant,[15, 26] and defect concentrations[6, 27] vary (often by orders of magnitude) depending on both processing conditions and the spectroscopic technique used to characterize the materials. The extensive variation of the fundamental photophysical parameters seen for lead trihalide perovskites in the literature confirms that heterogeneities play a dominant role in determining the photophysics of these materials.

While it is true that significant progress has been made towards commercially viable perovskite-based devices despite the inconsistencies present in the literature, a more reliable knowledge of the benchmark properties of lead halide perovskites is necessary to reveal clearer routes towards device optimization. Towards this aim, the work presented in this dissertation employs spatially resolved ultrafast microscopy, a form of ultrafast spectroscopy that leverages a microscope objective to dramatically reduce the sample interrogation volumes from 100 μm^2 – 1mm^2 (characteristic of traditional ultrafast spectroscopies) to the Abbe diffraction limit (typically 200 nm^2 – 1

μm^2).[28-30] By reducing the sample interrogation volume ultrafast microscopy is less sensitive to macro-scale morphological heterogeneity, instead affording the experimentalist the opportunity to focus on homogeneous areas of a sample crystallite in an attempt to generate an experimental observable determined largely by the inherent properties of the sample.

Ultrafast microscopy has increasingly been utilized as research efforts have moved towards nanoscale and heterogeneous materials where structural heterogeneities play a determining role in material photophysics. In fact, it is largely *because* of ultrafast microscopy that structural heterogeneity is known to play an outsized role in the photophysics of many materials. In 2012 Huang *et al.* used ultrafast microscopy to identify extensive heterogeneity of carrier recombination rates in organic polymers.[31] Following that, in 2015 Papanikolas *et al.* identified material strain to play a large role in the recombination of electrons and holes in Silicon nanowires.[28] Ultrafast microscopy also boasts impressive sensitivity, with instruments routinely reaching detection limits of $\Delta I/I \approx 10^{-5}$ and one group reporting signal sizes on the order[32] of $\Delta I/I \approx 10^{-7}$.

Additionally, ultrafast microscopy is the only all-optical method of characterization that allows direct imaging of photogenerated charge carrier diffusion, making it an ideal candidate to study charge carrier transport phenomena. Initial characterization of carrier transport in lead-halide perovskites using ultrafast microscopy was conducted by Huang et al.[15] However, the crystallites interrogated by Huang and colleagues were roughly equivalent to the sample interrogation volume, suggesting that grain boundary effects played a significant if not determining role in their measurements.

To circumvent this, our research group developed new solution processed fabrication methods to yield thin film samples consisting of individual crystallites ranging from tens to thousands of square microns, allowing us to observe localized carrier diffusion across single crystalline sections of perovskite crystallite. Throughout this work, various highly crystalline lead halide perovskites were analyzed using ultrafast microscopy to better characterize their innate transport properties by minimizing the effect of structural heterogeneities on experimental observables.

This dissertation is divided into six chapters. The remainder of this chapter will be devoted to a description and discussion of the ultrafast microscopy technique. A discussion of the photophysics relevant to the application of ultrafast microscopy to semiconductors is provided in Section 1.2. Section 1.3 contains information regarding the construction and operation of an ultrafast microscope. Discussion of ultrafast microscopy concludes in Section 1.4 which pertains to of the different imaging modalities typically employed over the course of an ultrafast microscopy experiment. Because this work encompasses experiments performed on a diverse assortment of lead halide perovskites, in-depth discussions of synthetic methods are left for the Chapters in which they are relevant.

Chapter 2 will recount initial characterization of the lead halide perovskite $MAPbI_3$ using ultrafast microscopy and will contain discussions of observed carrier lifetimes, recombination mechanisms, and carrier cooling. Extensive heterogeneity of these properties observed between crystallites and, in some cases, different locations on the same crystallite are also highlighted. Chapter 3 focuses exclusively on carrier

transport in $MAPbI_3$, utilizing diffusion data collected at various carrier densities spanning almost two orders of magnitude to elucidate some mechanisms at play surrounding the surprisingly high diffusivity of $MAPbI_3$. Chapter 4 details the development of a new all-optical methodology capable of disentangling the contributions of photogenerated carrier effective mass and mean scattering time towards determining carrier diffusivity. This methodology is then applied to two different perovskites ($MAPbI_3$ and $CsPbBrI_2$) to rationalize their disparate measured diffusivities. In Chapter 5 carrier transport measurements are performed on a series of lead tri-bromide perovskites with various A-site cations to better understand the role of the cation in carrier transport. Discrepancies in the transport observed in these tri-bromide perovskites are explored further, where we apply the methodology from Chapter 4 to characterize the optical mass and mean scattering time of photogenerated carriers in each species. Finally, in Chapter 6 a summary of the work presented in this dissertation is provided along with several potential future avenues of research.

1.2 Photophysics of Ultrafast Microscopy: Application to Semiconductors

Ultrafast microscopy is a two-beam ultrafast spectroscopy technique also known as pump-probe microscopy. As this moniker suggests, the pump beam is the first to interact with the sample. In the case of the above bandgap excitation of a semiconductor, this pump pulse generates a population of excited state charge carriers, typically in the form of excitons[33-36] (coulombically bound electron-hole pairs) or unbound free

carriers.[37-40] The probe pulse is then used to monitor the spatial and temporal evolution of the photogenerated carriers.

The injection of charge carriers changes the fundamental optical constants of the material,[41-42] known as the refractive index (*n*) and the extinction coefficient (*k*). This change in the optical constants causes a small but detectable change in the intensity of the probe beam as seen by the detector due to the presence of photogenerated carriers created by the pump pulse. At energies below the bandgap energy (the energy required to excited a charge carrier from the valence band to the conduction band), changes to the refractive index (*i.e.* the real part of the dielectric function) dominate the semiconductor optical response.[43-44] Carrier-induced refractive index changes are often analyzed within the context of a Drude model,[43-46] which provides the following expression:[41]

$$\Delta n = -\frac{Ne^2\tau^2}{2m^* n_0 \varepsilon_0 (1+\omega^2\tau^2)} \qquad (1.1)$$

Where N is the photogenerated carrier density (carriers m^{-3}), e is the fundamental charge of an electron, τ is the mean carrier scattering time, m^* is the carrier optical mass, n_0 is the ground state refractive index of the host material, ε_0 is the static permittivity, and ω is the angular frequency of the probe pulse.

In addition to changes in *n*, photoinduced changes to *k* (the imaginary part of the dielectric function) can play a large role in the semiconductor optical response in the form of photoinduced bleaching and photoinduced absorption. A photoinduced bleach is characterized by a *decrease* in the extinction coefficient of the material after photoexcitation. In semiconductors, this phenomenon can be explained by considering

the effect of photoexcitation on the population of band-edge carriers probed slightly on the red-edge of the bandgap.

After photoexcitation of a semiconductor, carriers excited across the band-gap from the valence band into the conduction band preferentially occupy band-edge states after cooling. The injection of charge carriers into the conduction band results in a decrease of the absorption cross section near the band-gap energy, reflecting an increase in the amount of energy required to excite subsequent carriers from the valence band to the conduction band. This phenomenon is shown in Figure 1.1. Photoinduced absorption can be thought of analogously to photoinduced bleaching with the exception that it results in an *increase* in the density of states probed and therefore an *increase* in *k*.

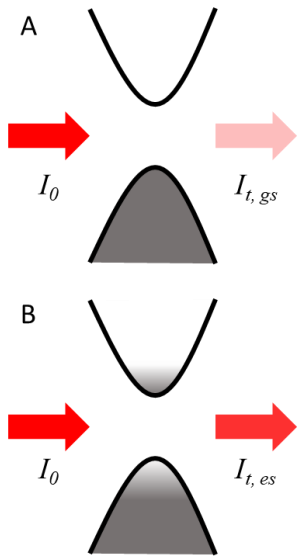

Figure 1.1. Photoinduced bleach of semiconductor. (A) Probe-beam transmitted intensity after passing through a semiconductor at equilibrium. (B) Probe-beam transmitted intensity after passing through a photoexcited semiconductor. Photoexcitation causes a decrease in the density of occupied states at the upper edge of the valence band, reflected by gradient filling of band-shape. This decrease in density of states causes *less* of the probe beam to be absorbed.

Another process by which the density of states along the band edges is changed upon photoexcitation is bandgap renormalization. Bandgap renormalization is the process by which the bandgap of a semiconductor narrows after the injection of charge carriers due to exchange and correlation energies of the generated holes and electrons.[47-48] Narrowing of the bandgap results in an increase in the density of states observed by the probe pulse leading to an *increase* in *k*. Bandgap renormalization is illustrated below in Figure 1.2.

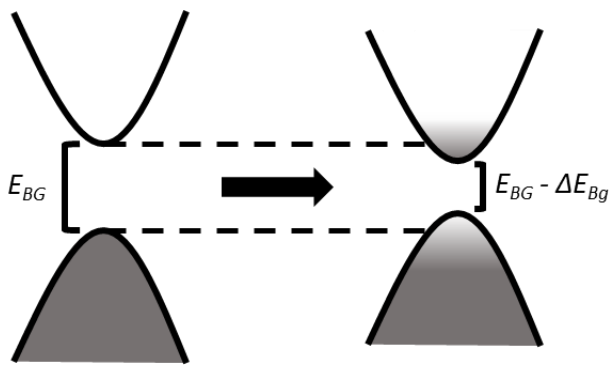

Figure 1.2. Band-gap renormalization occurring after photoexcitation. A decrease in the band-gap leads to an increase in the density of probed states causing an increase in the extinction coefficient of the sample at energies near the band edge.

The imaginary part of the dielectric function, *k*, can also influence the transient response of a semiconductor through free carrier absorption. During this process, the probe pulse induces further excitation of photoexcited carriers from the band-edge to deeper in their respective bands. Within a Drude model this phenomenon can be analyzed by considering the effect of free carriers on the extinction coefficient, *k*:[41]

$$\Delta k = \left(\frac{Ne^2\tau}{2n_0 m^* \varepsilon_0 (1+\omega^2\tau^2)}\right)^{1/2} \quad (1.2)$$

Changes to the extinction coefficient predicted by the Drude model can then be related back to changes in the material absorption coefficient ($\alpha = 4\pi k/\lambda$) due to the presence of photogenerated carriers.

Equations 1.1 and 1.2 lay bare the fact that the optical response of a semiconductor is determined by a host of more fundamental properties, each of which plays an important role in optoelectronic device operation. m^* and τ, for example, play determining roles in both the Drude response and in carrier transport phenomena discussed at length in the subsequent chapters of this work. When considered in concert with other optical effects present in semiconductors after photoexcitation (band-gap renormalization,[49] band-filling,[17] stimulated emission, etc.), it becomes apparent that creative and tactful application of ultrafast spectroscopy allows the explicit determination of many properties of a given sample, making ultrafast spectroscopy an invaluable tool for characterizing the optical properties of semiconductors.

1.3 Ultrafast Microscopy: Instrumentation

The primary instrument used in this thesis is a home built ultrafast microscope (Fig 1.1). To begin a pulse train is generated in a Ti:Sapphire oscillator cavity (SpectraPhysics, MaiTai). This oscillator operates with an 80 MHz repetition rate and generates pulses with a temporal duration of ~70 fs. The fundamental wavelength produced by the oscillator is tunable from the mid-visible to the near infrared (690 nm – 1040 nm). After generation, the pulse train is split into two different pulses termed the

pump pulse and the probe pulse. The path of the pump pulse will be explained first, followed by a discussion of the probe pulse's path.

After the pulses are split the pump pulse is directed towards an acousto-optic modulator (AOM). The AOM is made up of a tellurium dioxide crystal coupled to an RF transducer. When an RF pulse passes through the AOM crystal, mechanical strain is imparted causing a periodic change in the crystal's index of refraction. The coupled laser pulse diffracts off the RF-induced grating, which occurs at the modulation frequency of the driving RF signal. The AOM is used to reduce the repetition rate of the pump pulse from 80 MHz (the fundamental repetition rate) to a lower value, determined by the photophysics of the material being studied. After passing through the AOM, the pump pulse is directed towards a photonic crystal fiber (PCF) for supercontinuum generation, which converts the initially spectrally narrow pulse into a broad continuum spanning the visible to the near-IR. The desired pump wavelength is isolated from the supercontinuum using a thin-film interference filter. After supercontinuum generation, the pulse is sent towards a dichroic beamsplitter and coupled into the back aperture of a microscope objective (Olympus 100X, .9 NA). The sample is mounted at the focal point of the microscope objective on a piezoelectric positioning stage (MadCity Labs) that allows the pump pulse to be positioned over regions of interest.

The probe pulse is also directed towards an AOM immediately after the two pulses are split. This AOM functions identically to the pump AOM but operates at a higher modulation frequency. The modulation frequencies of the two AOMs are different to allow the use of lock-in detection to amplify the transient signal. After passing through

the AOM the probe pulse is then guided to a linear translation stage (to control temporal delay between the pump and probe pulses) followed by a set of galvanometer mirrors (GV). After the GV the probe pulse is sent through a 4f lens system and coupled into the back aperture of the microscope objective. Using the GV mirrors the entrance angle of the probe beam into the back aperture of the microscope objective can be controlled via a computer interface. By changing this entrance angle the spatial location of the focused probe beam on the sample can be controlled independently of the pump.

After the pump and probe pulses interact with the sample, one of two different detection schemes are employed depending on whether the microscope is operating in a transmissive or reflective geometry. In a transmissive geometry, transmitted probe light is collected with a condenser lens and directed towards an amplified photodiode detector. If the microscope is operating in a reflective geometry, a beamsplitter is placed immediately before the GV. Probe light reflected off the surface of the sample is collected and re-collimated by the microscope objective and retraces its original path until the beamsplitter where it is redirected towards an amplified photodiode. In both cases the signal from the photodetector is sent to a lock-in amplifier referenced to the modulation rate of the pump AOM. A schematic of the ultrafast microscope in our laboratory is shown in Figure 1.3.

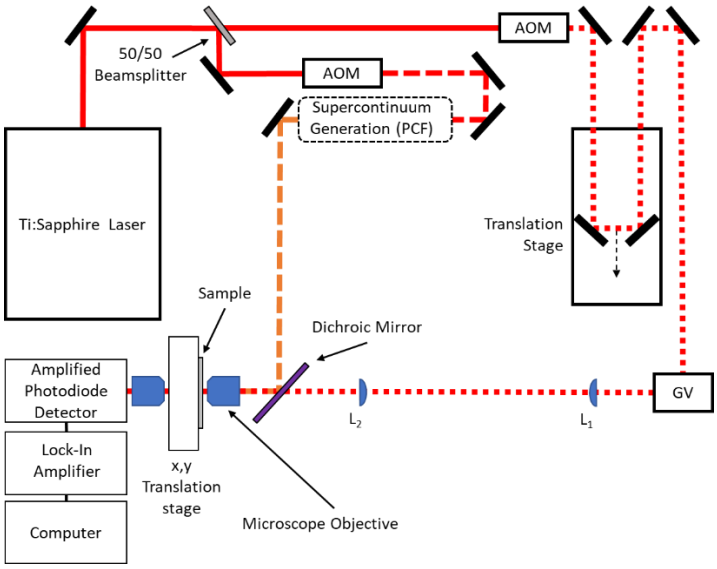

Figure 1.3. Schematic of home built ultrafast microscope operating in a transmissive geometry. AOM: acousto-optic modulator. GV: galvanometer mirror. PCF: photonic crystal fiber.

As mentioned above in Section 1.2, the generation of charge carriers by the pump pulse alters the fundamental optical constants of the material. Changes in a material's optical constants manifest as a change in the intensity of the probe beam as seen by the detector. This effect is demonstrated in Figure 1.4.

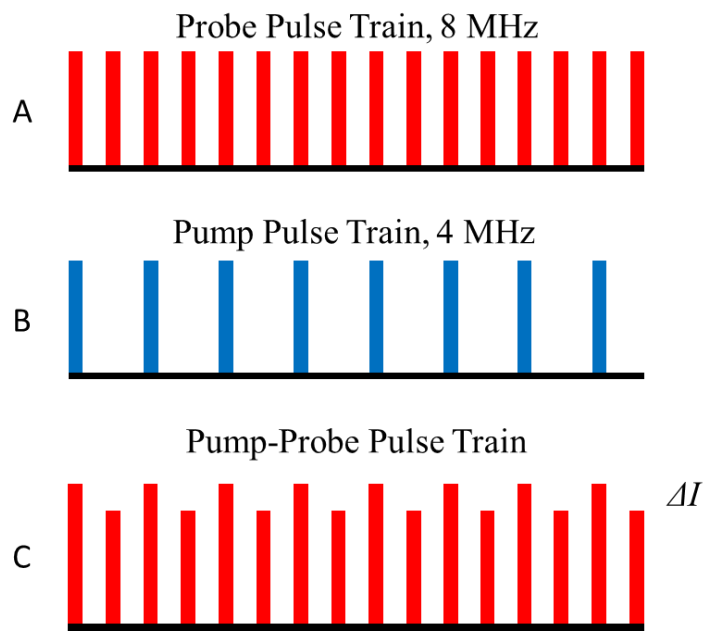

Figure 1.4. Effect of modulated photoexcitation of a semiconductor sample on the probe pulse train in an ultrafast microscopy experiment. (A) Initial probe pulse train before interaction with sample. (B) Pump pulse train used to excite sample. (C) Probe pulse train after interaction with sample. ΔI depicts modulated changes in intensity due to interaction with the photoexcited sample relative to the sample before excitation.

One can infer from panel C of Figure 1.4 that ΔI is expected to be quite small when compared to the fundamental intensity of the probe pulse train, I. In a typical semiconductor excited with a moderate density of photogenerated carriers, ΔI values on the order of 10^{-3} – 10^{-6} can be expected. In order to isolate and amplify this signal, lock-in amplification is used. A lock-in amplifier performs a Fourier transform of the input signal to isolate and amplify contributions to the signal at a single reference temporal frequency.

1.4 Ultrafast Microscopic Imaging

An ultrafast microscope provides the ability to probe the temporal and spatial evolution of photogenerated carriers in a sample. Due to the use of a microscope objective, correlations can be made between the local structure of the sample and the measured optical

response, making ultrafast microscopy an excellent tool for studying heterogeneous materials such as solution-processed lead halide perovskites. The microscope used for the majority of the work presented in this dissertation operates in three different modalities, which are summarized in the following three sections.

1.4.1 Spatially-Overlapped Imaging

In the first operational mode of the microscope, known as spatially overlapped imaging, the magnitude and sign of the transient signal of a large sample area at a single temporal delay can be determined. In this mode, the GV are used to spatially overlap the pump and probe pulses and the desired temporal delay is selected using the linear translation stage. The sample is then raster scanned beneath the overlapped pump and probe pulses using the piezoelectric translation stage, pausing to collect the intensity of the transient signal at each point. An example of a spatially-overlapped image collected from an $MAPbI_3$ domain is shown in panel A of Figure 1.5. A scanning emission micrograph of the same domain is shown in panel B.

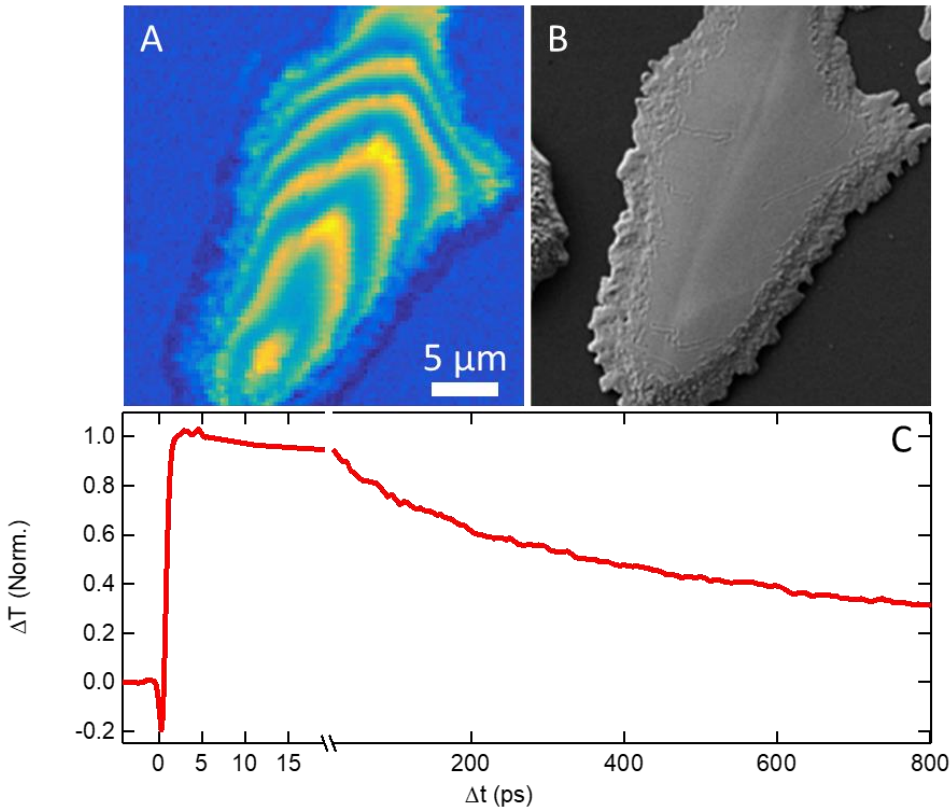

Figure 1.5. Characterization of an $MAPbI_3$ crystallite. (A) Spatially-overlapped image collected at $\Delta t = 4$ ps. (B) Scanning emission micrograph of domain shown in panel A. (C) Spatially overlapped kinetics scan taken from domain shown in panel A.

It is apparent from Figure 1.5 A that the transient signal in these materials is heterogeneous. Much of the variation in the transient response along the bulk of the crystal are caused Fabry-Perot interference[50-51] which causes the magnitude of the transient signal to oscillate as the local thickness of the sample changes. This phenomenon will be revisited and explored in greater detail in Chapter 4 and Chapter 5 of this work. However, we note here that it is imperative to perform measurements on a region of the sample displaying a relatively homogeneous transient response. Failure to do so results in the acquisition of unreliable data due to spatially-dependent sensitivity to photogenerated carriers. For example, comparison of Figures 1.5 A and 1.5 B

demonstrates the transient signal to be less pronounced and more heterogeneous around the edges of the domain consistent with the surface roughness apparent in the SEM image. Data collected in regions with high surface roughness will be influenced more heavily by grain boundary effects likely leading to reduced diffusivity.[9]

1.4.2 Spatially-Overlapped Decay Traces

The lifetime of photogenerated carriers is an important parameter to examine when considering a material for use in any optoelectronic device. Ultrafast microscopy can be used to determine the lifetime of photogenerated carriers by performing what is known as a spatially-overlapped decay trace. To collect a spatially-overlapped decay trace, the pump pulse is first positioned over a region of interest using the piezoelectric translation stage. The galvanometer mirrors are then used to position the probe pulse directly on top of the pump pulse. Temporal separation between the pump and probe pulses is then incrementally increased using the linear delay stage, pausing at each delay time to measure the intensity of the transient signal. An example decay trace taken from an $MAPbI_3$ domain is shown in panel C of Figure 1.5.

Equations 1.1 and 1.2 describe the optical response of the sample to be linear with respect to the number of photogenerated carriers. This is, in general, a good description of the optical response at energies below the band gap. When probing frequencies at or above the bandgap, many-body effects (such as band filling,[45] band gap renormalization,[52] etc.) can contribute to the optical response and complicate data analysis significantly. The data shown in Figure 1.5 C was collected using a probe frequency below the band gap of the sample being studied, suggesting the normalized

signal provides direct information regarding what fraction of the photogenerated carriers have recombined at a given delay time. Data like that shown in Figure 1.5 C can be used to characterize pathways by which charge carriers are decaying. Density dependent recombination (decay kinetics that vary with the fluence of the excitation pulse) can be attributed to either second (bimolecular)[53] or third[54] order (Auger) recombination processes. In heterogeneous materials, density-independent recombination typically corresponds to Shockley-Read-Hall recombination typically consisting of photogenerated carriers recombining through traps created by heterogeneities or imperfections in the sample crystalline lattice.[54]

1.4.3 Spatially-Separated Imaging

The final imaging modality employed by ultrafast microscopy is known as spatially-separated imaging. This imaging method enables direct imaging of the spatial evolution of photogenerated charge carriers and, consequently, the determination of the local ambipolar diffusion constant. Before discussing the specifics of a spatially-separated imaging experiment, a brief review of carrier transport in semiconductors is warranted.

Photoexcitation of the materials studied in this work generates two excited state particles known as electrons and holes. In the presence of an electric field these particles both move through the lattice at a rate determined by their mobility, μ. In the absence of an applied electric field (as is the case in a spatially-separated imaging experiment) carrier transport is determined by the diffusivity of the carriers, D. The mobility and

diffusivity of photogenerated carriers are related to each other through the Einstein relation:[55]

$$D_{am} = \frac{\mu_{am} kT}{q} \qquad (1.3)$$

Here D_{am} is the ambipolar diffusivity, μ_{am} is the ambipolar mobility, k is Boltzmann's constant, T is the temperature of the carrier population, and q is the fundamental charge. The term "ambipolar" is used when considering the contributions of both electrons and holes and can be considered an average of the two.

The ambipolar diffusion constant of a material can, in turn, be related to more fundamental material properties:

$$D_{am} = \frac{\tau kT}{m_{av}} \qquad (1.4)$$

Here, τ is the carrier mean scattering time, and m_{av} is the average mass of the photogenerated carriers. The carrier mean scattering time is determined by how often a carrier experiences a scattering event which alters its momentum state. These scattering events include collisions with impurities in the lattice, coupling to vibrational modes of the lattice, and (in cases of high carrier density) collisions with other charge carriers.[12, 55] The mass of the photogenerated carriers is determined largely by the dispersion of the valence and conduction bands.[41] A more in-depth discussion of these parameters and the extent to which they govern transport in perovskites is left for Chapter 4.

The spatial resolution provided by ultrafast microscopy allows the experimentalist to directly image the diffusion of charge carriers through a sample. Charge carriers are first generated using the pump pulse, and the spatial evolution of those carriers is then monitored using the probe pulse. Initially, the spatial distribution of charge carriers will

take on a shape identical to that of pump pulse and then broaden in time as carriers diffuse away from the excitation spot. In one dimension, the contribution of diffusion to the width of the carrier distribution can be determined by the convolution of the pump and probe beam spatial profile with the linear diffusion equation, the analytical solution of which is given by equation 1.5:

$$I_{\Delta x}(t) = \frac{a_0}{\beta(t)} e^{-4\ln(2)\Delta x^2 / \beta(t)^2} \quad (1.5)$$

Here a_0 is a time-dependent intensity scaling factor, Δx is the location of the center of the excitation pulse, and $\beta(t)$ describes the time-dependent width of the distribution:

$$\beta(t) = ({\gamma_1}^2 + {\gamma_2}^2 + 16\ln(2)\, D \cdot (\Delta t - t_0))^{1/2} \qquad (1.6)$$

Where γ_1 and γ_2 are the full-width at half-maximums of the pump and probe beams, D_{am} is the ambipolar diffusion constant, and Δt is the time after excitation (which occurs at t_0). Examination of Equations 1.5 and 1.6 confirm that the diffusion constant of a material can be extracted from multiple images of a charge carrier distribution taken at several increasing delay times.

To begin a spatially-separated imaging experiment, a spatially-overlapped image of a domain is collected (Figure 1.5 Panel A). From that image a region with a homogeneous transient response is selected to characterize. The delay stage is then moved to the temporal delay corresponding to the highest magnitude of the transient signal (typically $\Delta t \approx 1$ ps – 5 ps) and the galvanometer mirrors are used to raster scan the probe pulse around the area of pump excitation. This process is then repeated at increasing delay times. The result is a series of images that maps out the spatial

distribution of the photogenerated charge carriers with respect to time. An example set of these images is shown in panel C of Figure 1.6.

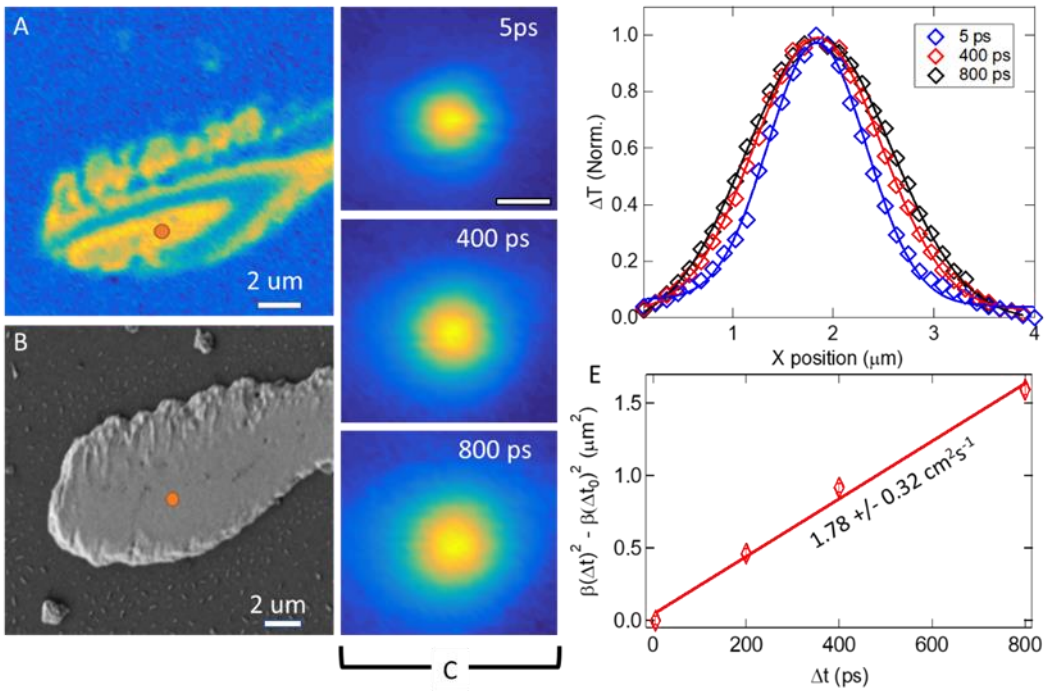

Figure 1.6. Determining the local ambipolar diffusivity of a material using spatially separated microscopy. (A) Spatially overlapped image of perovskite crystallite. Area interrogated shown to scale as orange dot. (B) Scanning electron microscopy image of the domain shown in panel A. (C) Images of photogenerated charge carrier cloud at several different time points, denoted in top-right corner of images. (D) Integrated profiles of data display in panel C which show obvious charge-carrier diffusion. (E) Square of FWHM of photogenerated carrier distribution with respect to time fit to Equation 1.3.

Each individual image is then integrated along either the x- or the y-direction, resulting in a spatial distribution that can be well fit with a Gaussian profile (Eq 1.5) as shown in panel D of Figure 1.6. The square of the full-width-at-half-maximum (FWHM) of each distribution is extracted from the fits and plotted with respect to time. In the limit of diffusive motion, the time dependent change of the FWHM of the distribution is given by Eq. 1.6. A collection of diffusion data is shown in panel E of Figure 1.5. From the

slope of a line of best fit determined by Equation 1.3 the local ambipolar diffusivity of the sample can be obtained.

REFERENCES CITED

(1) Shank, C. V.; Yen, R.; Hirlimann, C. Time-Resolved Reflectivity Measurements of Femtosecond-Optical-Pulse-Induced Phase Transitions in Silicon. *Phys. Rev. Lett.* **1983,** *50*, 454-457.

(2) Massaro, E. S.; Hill, A. H.; Grumstrup, E. M. Super-Resolution Structured Pump–Probe Microscopy. *ACS Photonics* **2016,** *3*, 501-506.

(3) Mehl, B. P.; Kirschbrown, J. R.; House, R. L.; Papanikolas, J. M. The End Is Different Than the Middle: Spatially Dependent Dynamics in Zno Rods Observed by Femtosecond Pump-Probe Microscopy. *J. Phys. Chem. Lett.* **2011,** *2*, 1777-1781.

(4) Blake, J. C.; Eldridge, P. S.; Gundlach, L. Spatial Variation in Carrier Dynamics Along a Single Cdsse Nanowire. *Chem. Phys.* **2014,** *442*, 128-131.

(5) Simpson, M. J.; Doughty, B.; Yang, B.; Xiao, K.; Ma, Y.-Z. Spatial Localization of Excitons and Charge Carriers in Hybrid Perovskite Films. *J. Phys. Chem. Lett.* **2015,** *6*, 3041-3047.

(6) Tian, Y.; Merdasa, A.; Peter, M.; Abedellah, M.; Zheng, K.; Jr., C. S. P.; Pullerits, T.; Yartsev, A.; Sundstrom, V.; Scheblykin, I. G. Giant Photoluminescence Blinking of Perovskite Nanocrystals Reveals Single-Trap Control of Luminescence. *Nano Lett.* **2015,** *15*, 1603-1608.

(7) de Quilettes, D. W.; Vorpahl, S. M.; Stranks, S. D.; Nagaoka, H.; Eperon, G. E.; Ziffer, M. E.; Snaith, H. J.; Ginger, D. S. Impact of Microstructure on Local Carrier Lifetime in Perovskite Solar Cells. *Science* **2015,** *348*, 683-686.

(8) Nah, S.; Spokoyny, B.; Stoumpos, C.; Soe, C. M. M.; Kanatzidis, M.; Harel, E. Spatially Segregated Free-Carrier and Exciton Populations in Individual Lead Halide Perovskite Grains. *Nat. Photonics* **2017,** *11*, 285-288.

(9) Hill, A. H.; Smyser, K. E.; Kennedy, C. L.; Massaro, E. S.; Grumstrup, E. M. In *Transient Absorption Imaging of Carrier Dynamics in Disordered Semiconductors*, 2017; pp 101930W-101930W-8.

(10) Kojima, A.; Teshima, K.; Shirai, Y.; Miyasaka, T. Organometal Halide Perovskites as Visible-Light Sensitizers for Photovoltaic Cells. *J. Am. Chem. Soc.* **2009,** *131*, 6050-6051.

(11) Levelized Cost of New Electricity Generating Technologies. https://www.instituteforenergyresearch.org/studies/levelized-cost-of-new-generating-technologies/ (accessed 1/4/2018).

(12) Li, C.-M.; Sjodin, T.; Dai, H.-L. Photoexcited Carrier Diffusion near a Si(111) Surface: Non-Negligible Consequence of Carrier-Carrier Scattering. *Phys. Rev. B* **1997,** *56*, 15252-15255.

(13) Stranks, S. D.; Eperon, G. E.; Grancini, G.; Menelaou, C.; Alcocer, M. J. P.; Leijtens, T.; Herz, L. M.; Petrozza, A.; Snaith, H. J. Electron-Hole Diffusion Lengths Exceeding 1 Micrometer in Organometal Trihalide Perovskite Absorber. *Science* **2013,** *342*, 641-344.

(14) Zhang, W.; Saliba, M.; Moore, D. T.; Pathak, S. K.; Hörantner, M. T.; Stergiopoulos, T.; Stranks, S. D.; Eperon, G. E.; Alexander-Webber, J. A.; Abate, A.; et al. Ultrasmooth Organic-Inorganic Perovskite Thin-Film Formation and Crystallization for Efficient Planar Heterojunction Solar Cells. *Nat. Commun.* **2015,** *6*, 6142.

(15) Guo, Z.; Manser, J. S.; Wan, Y.; Kamat, P. V.; Huang, L. Spatial and Temporal Imaging of Long-Range Charge Transport in Perovskite Thin Films by Ultrafast Microscopy. *Nat. Commun.* **2015,** *6*, 7471.

(16) Christians, J. A.; Manser, J. S.; Kamat, P. V. Multifaceted Excited State of $CH_3NH_3PbI_3$. Charge Separation, Recombination, and Trapping. *J. Phys. Chem. Lett.* **2015,** *6*, 2086-2095.

(17) Manser, J. S.; Kamat, P. V. Band Filling with Free Charge Carriers in Organometal Halide Perovskites. *Nat. Photonics* **2014,** *8*, 737-743.

(18) Im, J.-H.; Jang, I.-H.; Pellet, N.; Grätzel, M.; Park, N.-G. Growth of $CH_3NH_3PbI_3$ Cuboids with Controlled Size for High-Efficiency Perovskite Solar Cells. *Nat. Nanotechnol.* **2014,** *9*, 927-932.

(19) Kim, H.-S.; Im, S. H.; Park, N.-G. Organolead Halide Perovskite: New Horizons in Solar Cell Research. *J. Phys. Chem. C* **2014,** *118*, 5615-5625.

(20) Tan, Z.-K.; Moghaddam, R. S.; Lai, M. L.; Docampo, P.; Higler, R.; Deschler, F.; Price, M.; Sadhanala, A.; Pazos, L. M.; Credgington, D.; et al. Bright Light-Emitting Diodes Based on Organometal Halide Perovskite. *Nat. Nanotechnol.* **2014,** *9*, 687-692.

(21) Zhang, Q.; Ha, S. T.; Liu, X.; Sum, T. C.; Xiong, Q. Room-Temperature near-Infared High-Q Perovskite Whispering-Gallery Planar Nanolasers. *Nano Lett.* **2014,** *14*, 5995-6001.

(22) Fang, Y.; Dong, Q.; Shao, Y.; Yuan, Y.; Huang, J. Highly Narrowband Perovskite Single-Crystal Photodetectors Enabled by Surface-Charge Recombination. *Nat. Photonics* **2015,** *9*, 679-686.

(23) Xing, G.; Matthews, N.; Sun, S.; Lim, S. S.; Lam, Y. M.; Gratzel, M.; Mhaisalkar, S.; T.C., S. Long-Range Balanced Electron- and Hole-Transport Lengths in Organic-Inorganic CH3NH3PbI3. *Science* **2013,** *342*, 344-347.

(24) Lin, Q.; Armin, A.; Nagiri, R. C. R.; Burn, P. L.; Meredith, P. Electro-Optics of Perovskite Solar Cells. *Nat. Photonics* **2014,** *9*, 106-112.

(25) Sun, S.; Salim, T.; Matthews, N.; Duchamp, M.; Boothroyd, C.; Xing, G.; Sum, T. C.; Lam, Y. M. The Origin of High Efficiency in Low-Temperature Solution-Processable Bilayer Organimetal Halide Hybrid Solar Cells. *Energy Environ. Sci* **2014,** *7*, 399-407.

(26) Tian, W.; Zhao, C.; Leng, J.; Cui, R.; Jin, S. Visualizing Carrier Diffusion in Individual Single-Crystal Organolead Halide Perovskite Nanowires and Nanoplates. *J. Am. Chem. Soc.* **2015,** *137*, 12458-12461.

(27) Dong, Q.; Fang, Y.; Shao, Y.; Mulligan, P.; Qiu, J.; Cao, L.; Huang, J. Electron-Hole Diffusion Lengths > 175 Mm in Solution-Grown $CH_3NH_3PbI_3$ Single Crystals. *Science* **2015,** *347*, 967-970.

(28) Grumstrup, E. M.; Gabriel, M. M.; Pinion, C. W.; Parker, J. K.; Cahoon, J. F.; Papanikolas, J. M. Reversible Strain-Induced Electron-Hole Recombination in Silicon

Nanowires Observed with Femtosecond Pump-Probe Microscopy. *Nano Lett.* **2014,** *14*, 6287-6292.

(29) Grumstrup, E. M.; Cating, E. M.; Gabriel, M. M.; Pinion, C. W.; Christesen, J. D.; Kirschbrown, J. R.; Vallorz, E. L.; Cahoon, J. F.; Papanikolas, J. M. Ultrafast Carrier Dynamics of Silicon Nanowire Ensembles: The Impact of Geometrical Heterogeneity on Charge Carrier Lifetime. *J. Phys. Chem. C* **2014,** *118*, 8626-8633.

(30) Grumstrup, E. M.; Gabriel, M. M.; Cating, E. M.; Pinion, C. W.; Christesen, J. D.; Kirschbrown, J. R.; Vallorz, E. L.; Cahoon, J. F.; Papanikolas, J. M. Ultrafast Carrier Dynamics in Individual Silicon Nanowires: Characterization of Diameter-Dependent Carrier Lifetime and Surface Recombination with Pump–Probe Microscopy. *J. Phys. Chem. C* **2014,** *118*, 8634-8640.

(31) Wong, C. T. O.; Lo, S. S.; Huang, L. Ultrafast Spatial Imaging of Charge Dynamics in Heterogeneous Polymer Blends. *J. Phys. Chem. Lett.* **2012,** *3*, 879-884.

(32) Gao, B.; Hartland, G. V.; Huang, L. Transient Absorption Spectroscopy of Excitons in an Individual Suspended Metallic Carbon Nanotube. *J. Phys. Chem. Lett.* **2013,** *4*, 3050-3055.

(33) Dai, D. C.; Monkman, A. P. Observation of Superfluorescence from a Quantum Ensemble of Coherent Excitons in a Znte Crystal: Evidence for Spontaneous Bose-Einstein Condensation of Excitons. *Phys. Rev. B* **2011,** *84*, 115206.

(34) Zhang, Q.; Liu, X.; Utama, M. I. B.; Zhang, J.; de la Mata, M.; Arbiol, J.; Lu, Y.; Sum, T. C.; Xiong, Q. Highly Enhanced Exciton Recombination Rate by Strong Electron–Phonon Coupling in Single Znte Nanobelt. *Nano Letters* **2012,** *12*, 6420-6427.

(35) Liu, Q.; Wang, Y.; Sui, N.; Wang, Y.; Chi, X.; Wang, Q.; Chen, Y.; Ji, W.; Zou, L.; Zhang, H. Exciton Relaxation Dynamics in Photo-Excited CsPbI3 Perovskite Nanocrystals. *Sci. Rep.* **2016,** *6*, 29442.

(36) de Jong, E. M. L. D.; Yamashita, G.; Gomez, L.; Ashida, M.; Fujiwara, Y.; Gregorkiewicz, T. Multiexciton Lifetime in All-Inorganic $CsPbBr_3$ Perovskite Nanocrystals. *J. Phys. Chem. C* **2017,** *121*, 1941-1947.

(37) Hoffman, C. A.; Jarašiūnas, K.; Gerritsen, H. J.; Nurmikko, A. V. Measurement of Surface Recombination Velocity in Semiconductors by Diffraction from Picosecond Transient Free-Carrier Gratings. *Appl. Phys. Lett.* **1978,** *33*, 536-539.

(38) Ling, Z. G.; Ajmera, P. K.; Kousik, G. S. Simultaneous Extraction of Bulk Lifetime and Surface Recombination Velocities from Free Carrier Absorption Transients. *J. Appl. Phys.* **1994,** *75*, 2718-2720.

(39) Yu, Z. G.; Krishnamurthy, S.; Guha, S. Photoexcited-Carrier-Induced Refractive Index Change in Small Bandgap Semiconductors. *J. Opt. Soc. Am. B* **2006,** *23*, 2356-2360.

(40) Piatkowski, P.; Cohen, B.; Javier Ramos, F.; Di Nunzio, M.; Nazeeruddin, M. K.; Gratzel, M.; Ahmad, S.; Douhal, A. Direct Monitoring of Ultrafast Electron and Hole Dynamics in Perovskite Solar Cells. *Phys. Chem. Chem. Phys.* **2015,** *17*, 14674-14684.

(41) Elliot, R. J.; Gibson, A. F. *An Introduction to Solid State Physics and Its Applications*. The Macmillan Press Ltd.: United Kingdom, 1974.

(42) Pankove, J. I. *Optical Processes in Semiconductors*. Dover Publications, Inc.: New York, 1971.

(43) Sabbah, A. J.; Riffe, D. M. Measurement of Silicon Surface Recombination Velocity Using Ultrafast Pump–Probe Reflectivity in the near Infrared. *J. Appl. Phys.* **2000,** *88*, 6954-6956.

(44) Sabbah, A. J.; Riffe, D. M. Femtosecond Pump-Probe Reflectivity Study of Silicon Carrier Dynamics. *Phys. Rev. B* **2002,** *66*, 165217.

(45) Bennett, B. R.; Soref, R. A.; Alamo, J. A. D. Carrier-Induced Change in Refractive Index of InP, GaAs and InGaAsP. *IEEE J. Quantum Electron.* **1990,** *26*, 113-122.

(46) Henry, C. H.; Logan, R. A.; Bertness, K. A. Spectral Dependence of the Change in Refractive Index Due to Carrier Injection in GaAs Lasers. *J. Appl. Phys.* **1981,** *52*, 4457-4461.

(47) Berggren, K. F.; Sernelius, B. E. Band-Gap Narrowing in Heavily Doped Many-Valley Semiconductors. *Phys. Rev. B* **1981,** *24*, 1971-1986.

(48) Klingshirn, C. *Semiconductor Optics*. 2nd ed.; Springer: Berlin, 2005.

(49) Price, M. B.; Butkus, J.; Jellicoe, T. C.; Sadhanala, A.; Briane, A.; Halpert, J. E.; Broch, K.; Hodgkiss, J. M.; Friend, R. H.; Deschler, F. Hot-Carrier Cooling and Photoinduced Refractive Index Changes in Organic-Inorganic Lead Halide Perovskites. *Nat. Commun.* **2015,** *6*, 8420.

(50) Hecht, E. *Optics*. Pearson Education: San Francisco, CA, 2002.

(51) Born, M.; Wolf, E. *Principles of Optics*. Pergamon Press: London, 1959.

(52) Feneberg, M.; Osterburg, S.; Lange, K.; Lidig, C.; Garke, B.; Goldhahn, R.; Richter, E.; Netzel, C.; Neumann, M. D.; Esser, N.; et al. Band Gap Renormalization and Burstein-Moss Effect in Silicon- and Germanium-Doped Wurtzite Gan up to 10^{20} Cm^{-3}. *Phys. Rev. B* **2014,** *90*, 075203.

(53) Hill, A. H.; Smyser, K. E.; Kennedy, C. L.; Massaro, E. S.; Grumstrup, E. M. Screened Charge Carrier Transport in Methylammonium Lead Iodide Perovskite Thin Films. *J. Phys. Chem. Lett.* **2017,** *8*, 948-953.

(54) Kennedy, C. L.; Hill, A. H.; Massaro, E. S.; Grumstrup, E. M. Ultrafast Excited-State Transport and Decay Dynamics in Cesium Lead Mixed Halide Perovskites. *ACS Energy Lett.* **2017,** *2*, 1501-1506.

(55) Sze, S. M. *Physics of Semiconductor Devices*. 3rd ed.; Wiley: New York, 2006.

CHAPTER TWO

ULTRAFAST MICROSCOPY OF METHYLAMMONIUM LEAD IODIDE PEROVSKITE THIN FILMS: HETEROGENEITY OF EXCITED STATE SPATIAL AND TEMPORAL EVOLUTION

Contributions of Authors and Co-Authors

Manuscript: Ultrafast Microscopy of Methylammonium Lead Halide Perovskite Thin Films: Heterogeneity of Excited State Spatial and Temporal Evolution

Author: Andrew H. Hill

Contributions: Synthesized and characterized all samples. Collected and analyzed all ultrafast microscopic data. Assisted in writing and editing manuscript.

Author: Kori E. Smyser

Contributions: Aided in development of synthetic protocols used to produce samples studied in this work.

Author: Casey L. Kennedy

Contributions: Aided in analysis of ultrafast microscopic data. Provided valuable feedback on early drafts of manuscript.

Author: Eric S. Massaro

Contributions: Aided in analysis of ultrafast microscopic data. Provided valuable feedback on early drafts of manuscript.

Author: Erik M. Grumstrup

Contributions: Assisted with analysis and editing of manuscript for final submission.

Manuscript Information Page

Andrew H. Hill, Kori E. Smyser, Casey L. Kennedy, Eric S. Massaro, Erik M. Grumstrup

Status of Manuscript:
_X__ Prepared for submission to a peer-reviewed journal
____ Officially submitted to a peer-review journal
____ Accepted by a peer-reviewed journal
____ Published in a peer-reviewed journal

CHAPTER TWO

ULTRAFAST MICROSCOPY OF METHYLAMMONIUM LEAD IODIDE PEROVSKITE THIN FILMS: HETEROGENEITY OF EXCITED STATE SPATIAL AND TEMPORAL EVOLUTION

2.1 Introduction

As discussed in Chapter 1, organometal halide perovskites (OMHPs) are currently the focus of intense research directed toward their use as high-performance optoelectronic materials.[10, 13-19] These efforts have been rewarded by photovoltaic devices exhibiting power conversion efficiencies greater than 22%,[12] as well as promising advances in the use of OMHPs as lasing media and photodetectors.[20-22] In each of these applications, favorable material properties, including low trap state densities,[17, 56] low defect concentrations,[6, 27] and exceptionally long charge diffusion lengths,[16, 57] are important factors in the remarkable optoelectronic performance of OMHPs.

Despite promising advancements in OMHP applications, reported values for important benchmarks of optoelectronic performance (charge diffusion length,[13, 16, 23] diffusion constant,[15, 26] exciton binding energies[24-25]) can vary substantially. Such variation likely stems from differences in material synthesis and device fabrication, as well as intrinsic structural and compositional heterogeneities like grain boundaries, surfaces, and chemical composition, which are known to strongly influence the local electronic structure of OMHPs.[5, 7, 58-59] Precisely correlating spectroscopic observables to specific structural or compositional features is therefore critical to an accurate understanding of OMHP

photophysics, particularly within the context of the heterogeneous thin films that comprise the majority of current research efforts.

In this Chapter we apply pump-probe microscopy to isolate individual crystalline domains and obtain structurally correlated spectroscopic measurements on a methylammonium lead iodide perovskite ($MAPbI_3$) thin film. The combined sub-micron spatial resolution and ultrafast temporal resolution of the technique has proved valuable for revealing insights into excited state decay dynamics,[60] free carrier transport,[61] surface plasmon propagation,[62] exciton dynamics,[63] intraparticle heterogeneity,[3] and unique interfacial states,[64] which are inaccessible with traditional bulk spectroscopies.

Overall, the film exhibits early-time kinetics that reflect a competition between ultrafast band gap renormalization and band filling, followed by longer-lived dynamics that are consistent with trap-mediated surface recombination. However, at a single domain level, our measurements reveal the pervasive heterogeneity present in $MAPbI_3$ thin films. We find charge-carrier half-lives that vary by greater than an order of magnitude within a single domain. These measurements highlight the importance of spatially-resolved spectroscopies for correlating OMHP material properties with the functional benchmarks that are critical to device applications.

2.2 Experimental Methods

2.2.1 Thin Film Synthesis and Characterizaation.

$MAPbI_3$ samples were prepared on glass substrates using a two-step spin coating method adapted from multiple established protocols.[65-67] The precursor salt

methylammonium iodide (MAI) was first prepared by reaction of 12 mL methylamine solution (33% in EtOH) with 5 mL HI (57 wt. % in H_2O) under an N_2 atmosphere and stirred for ~45 min at room temperature. The reaction mixture was then concentrated in vacuo to yield off-white crystalline product MAI. Crystals were washed with 3 x 30 mL diethyl ether until pure white, and then resuspended in 20 mL diethyl ether and concentrated in vacuo a second time to yield white, needlelike crystalline product.

Two separate solutions were then prepared; 1 M PbI_2 in dimethylformamide (DMF), and .25 M MAI in isopropyl alcohol (IPA). These solutions were then spin-cast onto a glass microscope slide in two steps. 50 μL PbI_2/DMF was drop cast and spun for 5 s at 3,000 rpm followed by 5 s at 4,500 rpm. After the final spin completed, 45 s passed before 200 μL MAI/IPA was drop cast on top of the PbI_2 layer and spun for 20 s at 4,000 rpm.

After precursor deposition, the films were transferred to a hot plate and annealed in a DMF atmosphere at 100 ^{o}C for 60 minutes. Solvent annealing has been shown to improve film morphology and increase photovoltaic device effiency.[68] Field emission scanning electron micrographs (Fig. 2.1 A) show large $MAPbI_3$ islands on top of the glass substrate, which appear to be single crystalline on a greater than 10-micron length scale. Additional topographic information of samples was obtained by atomic force microscopy (AFM; Fig. 2.1 B) showing a ~ 40% variation in thickness (Fig. 2.1 B, inset). X-Ray diffraction (Fig. 2.1 C) confirms the sample to be crystalline $MAPbI_3$ with no evidence of remaining unreacted PbI_2.[14, 69]

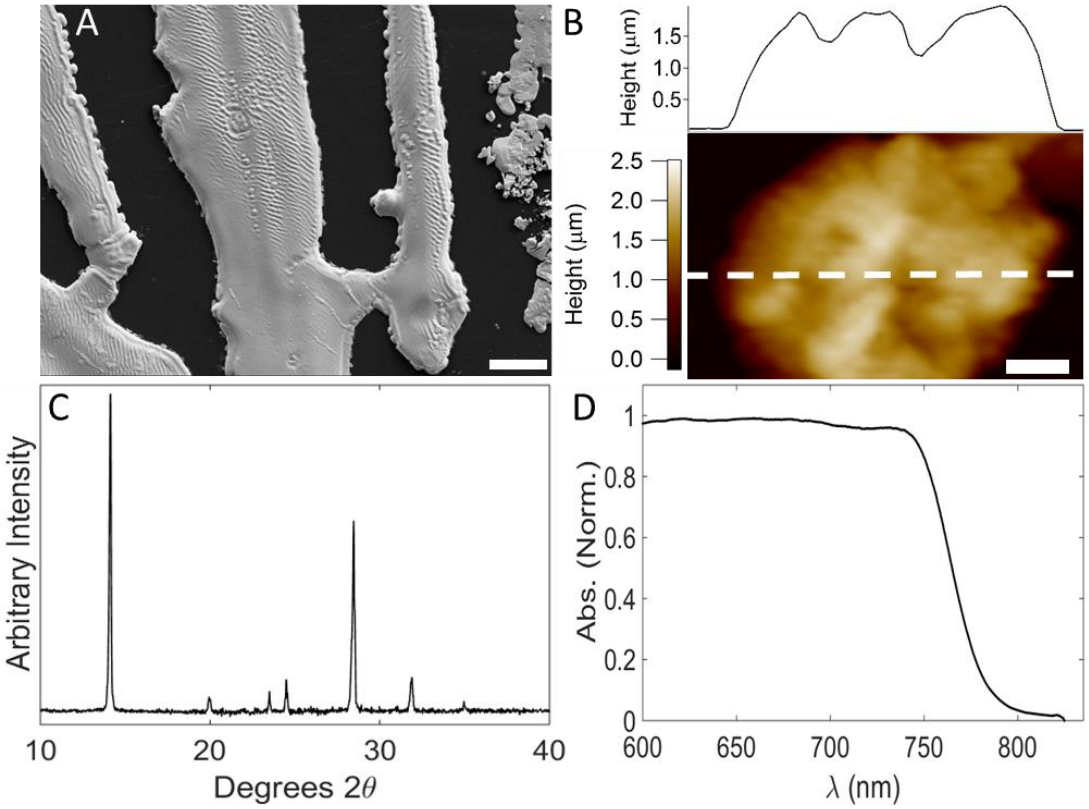

Figure 2.1. Characterization of $MAPbI_3$ thin films. (A) Field emission micrograph of a $MAPbI_3$ domain (scale bar: 5 μm). (B) Atomic force micrograph of a single $MAPbI_3$ domain (scale bar: 5 μm). Above: AFM cross section along dashed white line in image. (C) X-ray diffraction pattern showing a highly crystalline phase with little remaining unreacted precursor. Highest intensity peaks at 14.14º and 28.46º 2θ are indicative of (110) and (220) planes. No characteristic PbI_2 peak at 12.64º 2θ is observed. (D) Visible absorption spectrum of a single $MAPbI_3$ domain collected with a UV-visible microspectrometer.

2.2.2 Time-Resolved Microscopy

Transient kinetics from localized regions of $MAPbI_3$ domains are collected on a home-built pump-probe microscope as described in Chapter 1. Photogeneration was accomplished with a 400 nm excitation pulse and the evolution of the excited state was monitored using an 800 nm probe pulse. All data presented in this chapter was collected while the microscope was configured in a transmissive geometry. The numerical aperture of the microscope objective (100X, 0.9 NA) was roughly matched with that of the

condenser lens (0.7 NA) used to collect the transmitted probe light to avoid the influence of optical artifacts on the measurements.

2.3 Results and Discussion

2.3.1 Band-Edge Transient Dynamics

In Figure 2.2, we present transient imaging and kinetics from individual $MAPbI_3$ domains. For these measurements, both pump (λ_{pump} = 400 nm) and probe (λ_{probe} = 800 nm) are spatially overlapped on the sample to achieve an effective spatial resolution of ~ 220 nm full width at half maximum (fwhm). A pump-probe image of Domain I, collected by scanning the sample underneath the overlapped pump and probe beams, is shown in Panel A. The image exhibits significant (~70%) modulation in the transient response, which largely reflects variation in the domain thickness (see Chapter 4 and 5). Panel B of Figure 2.2 shows four transient kinetics traces collected at the location indicated in panel A for pump fluences ranging between 6.1 $\mu J/cm^2$ and 48.3 $\mu J/cm^2$. Overall, the kinetics are characterized by a short-lived photoinduced absorption (PIA), which decays with a sub-picosecond lifetime into a longer-lived photoinduced bleach (PIB). The PIB decays with an initial fast component of ~38 ps and persists beyond the scanning range of our instrument. Qualitatively similar dynamics, comprised of an initial short-lived PIA, and a long-lived multi-component transient bleach, were observed at four other locations on domain I, as well as on all other $MAPbI_3$ domains characterized. We will first discuss the photophysical origin of the early time PIA, and then describe the longer lived transient

bleach, which in agreement with previous reports, we attribute to a combination of band-filling and stimulated emission.[17, 49, 70-72]

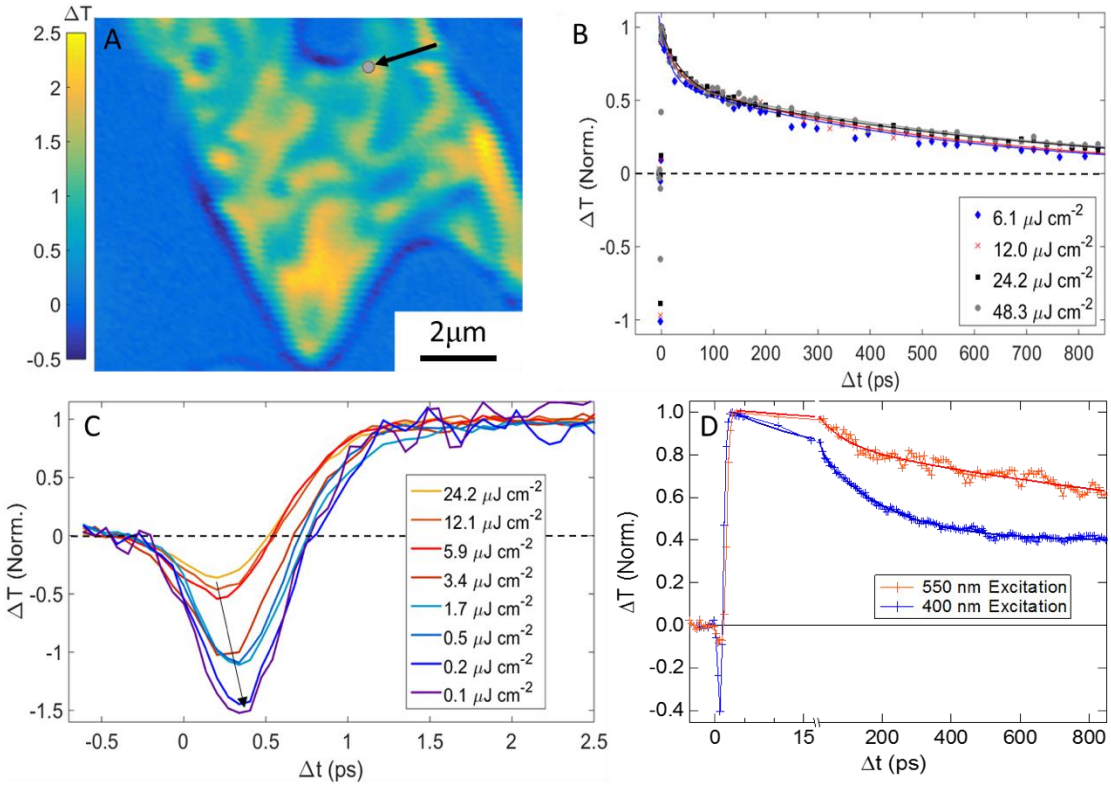

Figure 2.2. Transient dynamics of photoexcited $MAPbI_3$. (A) Pump-probe image (Δt = 2 ps) of a single $MAPbI_3$ domain (Domain I). Circle on the image indicates the location where the data shown in panel B was collected (and approximate spatial resolution of instrument). (B) Kinetics traces collected for excitation fluences between 6.1 μJ cm^{-2} and 48.3 μJ cm^{-2}. (C) Power dependence of early time PIA feature (λ_{pump} = 400 nm). Kinetics traces are normalized to the long-lived PIB that grows in by Δt = 1.5 ps. The arrow highlights the temporal shift of the PIA maximum at lower excitation densities. (D) Kinetics collected from a single location for two different excitation wavelengths. Pump fluence was 24.2 μJ cm^{-2} at 400 nm and 122 μJ cm^{-2} at 550 nm, producing a calculated ~53% higher carrier density for 550 nm excitation.

While we are limited to single wavelength measurements, previous reports of $MAPbI_3$ broadband transient transmission spectra show that at early times, kinetics collected at λ_{probe} = 800 nm reflect the low energy side of a derivative-like lineshape.[71-72]

This PIA has been attributed to a transient redshift of the absorption spectrum arising from either band gap renormalization[49] or from a transient Stark shift due to an exciton-induced microscopic electric field.[71] As we discuss below, power dependent measurements of the early time kinetics are consistent with a dynamic competition between band-gap renormalization, which redshifts the band gap energy due to correlation and exchange interactions, and band filling, which blueshifts the band gap energy as carriers cool and begin to occupy the thermalized band-edge states.

A detailed power-dependent study of the early time dynamics is presented in Panel C of Figure 2.3. The kinetics traces, normalized to the PIB at delays longer than 2 ps, highlight the relative decrease in PIA amplitude as the pump fluence is increased from 0.1 $\mu J/cm^2$ to 24.2 $\mu J/cm^2$ (calculated at 1/e width of the pump spot size). This observed power-dependence is consistent with band gap renormalization that predicts the magnitude of the associated spectral redshift to scale with the photogeenrated carrier density as $\sim n^{1/3}$.[47, 52] At low pump fluence, the charge carrier-induced renormalization increases the effective density of states accessible at λ_{probe} = 800 nm, causing the short-lived PIA. As the photoexcited carriers cool to the band edge, band filling dominates the transient response and we observe the photoinduced signal cross zero and grow into the long lived PIB. At higher pump fluences, carrier-carrier scattering causes faster carrier cooling, thereby increasing the occupation of band edge states at earlier delays. This interpretation is supported by the temporal shift of the PIA maximum highlighted in Figure 2.2 C. At the highest excitation densities, the maximum of the PIA occurs 140 fs earlier than it does at lower excitation densities, consistent with enhanced and earlier band filling from scattered

carriers. Similar band-edge effects are observed in GaAs, where at high excitation densities, enhanced carrier-carrier interactions directly scatter some carriers to the conduction band minimum (or valence band maximum),[73] creating a significant population of cooled carriers more quickly than through phonon coupling.

While quantitative modeling of the many-body cooling dynamics and a careful analysis of the full transient spectra is likely necessary to determine what role (if any) excitonic states play, these results suggest the early time PIA we observe can largely be described by free carrier contributions. We note this interpretation is consistent with Price et al. who show the relative magnitude of the PIA decreases as the excitation energy is moved nearer to the band edge,[49] an effect we also observe (see Fig. 2.2 D). In this case, as the pump is shifted to lower energies, the charge carrier density is generated with a lower effective temperature, and the renormalization-induced redshift is more quickly counteracted by band filling from cooled carriers.

Information regarding the specific timescales upon which carriers cool in $MAPbI_3$ can be obtained by fitting the data shown in Figure 2.2 C with a model used to quantitatively determine the rise time of the kinetics scan from the early-time photoinduced bleach. The results of these fits are shown in Figure 2.3 A. Two traces are shown in Figure 2.3 A; one collected using a 400 nm excitation pulse (blue) and the other collected using a 600 nm excitation pulse (red). In the case of 400 nm excitation we see no change in the measured carrier cooling time with respect to carrier density across nearly two orders of magnitude and recover an average carrier cooling time of ~ 220 fs. Across a comparable

range of excitation densities, we find carrier cooling time after 600 nm excitation to be similarly invariant with an average cooling time of ~ 130 fs.

The difference in the observed average cooling times after 400 nm and 600 nm excitation can be rationalized by considering the proximity of each excitation energy to the material bandgap (~765 nm for the samples studied in this manuscript). Above bandgap excitation imparts excess energy to photogenerated charge carriers, exciting them (at least initially) to states in the valence (and conduction) band removed from the band edge.[74] Carriers given more energy by their excitation pulse will initially lie farther from the band-edge of their respective bands, an effect which is illustrated in Figure 2.4 B. Carriers located at energies significantly above or below the band edge require an increased number of phonon interactions required to cool them to the temperature of the crystal lattice which in turn increases the time required to complete the cooling process. As such, carriers excited with energies closer to the band gap require less time to cool, in agreement with the data presented here.

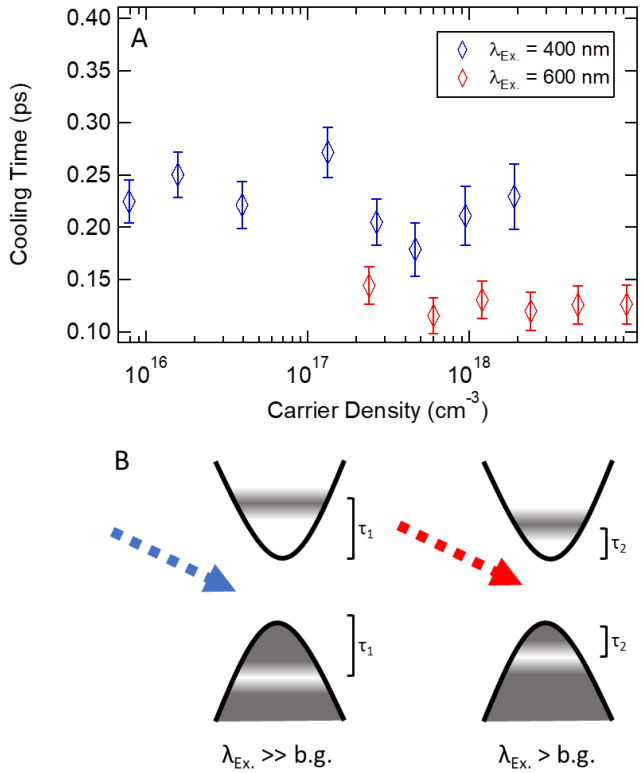

Figure 2.3. Carrier cooling dynamics in $MAPbI_3$. (A) Recovered carrier cooling times after excitation with 400 nm (blue) and 600 nm (red) pulses as a function of excitation density. (B) Graphical representation of excitation energy dependent cooling times.

At longer timescales (Δt > 2 ps), the PIB near the band edge reflects recombination dynamics of free carriers in $MAPbI_3$ films, which have been reported to undergo second order, band-to-band direct recombination.[17, 75-76] While the kinetics traces at λ_{probe} = 800 nm shown in Figure 2.2 B qualitatively reflect these dynamics, they differ from those previously observed in two important aspects. First, the kinetics we observe are markedly faster despite using photoexcitation fluences comparable to previous reports. Second, our results show that nearly a factor of ten increase in the pump fluence (6.1 μJ cm^{-2} to 48 μJ cm^{-2}) has no effect on the PIB dynamics, strongly indicating that neither Auger recombination nor band-to-band second order recombination mechanisms are at play.

Rather, the power independent kinetics suggest first order (trap-mediated) processes are dominating electron-hole recombination in these films.

In principle, both bulk and surface trap sites can contribute to carrier recombination.[44, 77] However, because the extinction coefficient of $MAPbI_3$ is 24.6 μm^{-1} at λ = 400 nm,[78] the majority of charge carriers are produced near the surface (1/e distance is ~ 40 nm). The close proximity of the photogenerated carriers to the domain surface implicates surface recombination as the dominant mechanism. To test this model, we compared kinetics traces of the recombination dynamics (probed at 800 nm) of a single $MAPbI_3$ domain after 400 nm and 550 nm photoexcitation. The extinction coefficient of $MAPbI_3$ at 550 nm (7.45 μm^{-1})[78] is more than a factor of three lower than that at 400 nm. Consequently, for the lower energy excitation, a greater number of charge carriers are generated in the bulk and slower recombination dynamics are expected as carriers must on average diffuse a greater distance to the surface. As shown in Figure 2.2 D, we observe kinetics that are consistent with this behavior – the transient bleach produced after 550 nm photoexcitation exhibits a slower decay relative to the PIB following 400 nm photoexcitation.

This data suggests $MAPbI_3$ films produced through the solvent-annealing approach have a significant density of surface recombination sites that decreases charge carrier lifetime relative to films annealed under ambient conditions. This conclusion is supported by time resolved photoluminescence (PL) we show in Figure 2.4. Our results show that films annealed under ambient conditions exhibit substantially increased PL lifetimes relative to solvent-annealed films. Similar effects were observed by Chen et al., who

proposed that annealing $MAPbI_3$ films under ambient conditions passivates the surface through PbI_2 formation.[58] XRD shown in panel B of Figure 2.4 corroborate this theory, with dry-annealed samples displaying a peak at 12º 2θ indicative of PbI_2.

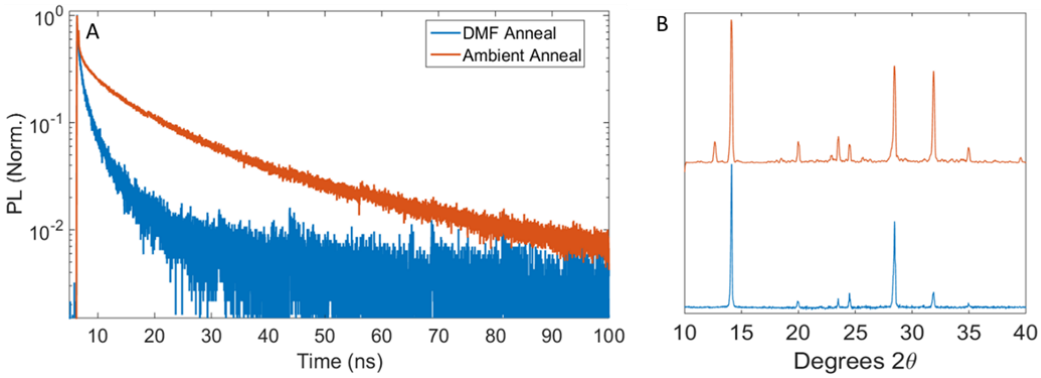

Figure 2.4. Comparison of time-resolved gluorescence spectra and x-ray diffractograms of wet and dry-annealed $MAPbI_3$ samples. (A) Time resolved fluorescence spectra of dry-annealed (orange) and solvent annealed (blue) $MAPbI_3$ samples. (B) XRD spectra of dry-annealed (orange) and solvent annealed (blue) $MAPbI_3$ samples.

Surfaces have also been invoked as the primary location for trap sites by Wu *et al.*, who argue based on spectroscopic comparisons between 2D and 3D perovskites, that excitonic self-trapping is enhanced at interfaces and surfaces.[70] While further investigation is required to identify the exact recombination mechanisms at play, the data presented here adds to a growing body of evidence that trap sites strongly influence the transient dynamics of $MAPbI_3$ films and play an important role in the efficiency of OMHP based photovoltaic devices.[5, 15]

The complex nature of the band-edge photophysics discussed in this section warrants a concise summary. Immediately after photoexcitation, the density of states available at the band-edge is determined by a dynamic competition between band-filling and band gap renormalization. These processes dominate the photoresponse of $MAPbI_3$

until photogenerated carriers have cooled to the band edge. The duration of this cooling process is shown to last 130 fs – 220 fs, depending on the excitation energy, with higher excitation energies displaying comparatively longer cooling times. Cooling times reported in this chapter are found to be independent of excitation density at densities up to ~10^{19} carriers cm^{-3}, in contrast to previous reports of a significant phonon bottlenecking effect in $MAPbI_3$.[79-80] After carriers cool to the band edge their recombination dynamics are found to be consistent with first order recombination at the fluences used. Analysis of recombination data collected using two separate excitation pulse wavelengths suggests the dominant recombination pathway to be surface trap mediated.

2.3.2 Lifetime Imaging

Comparison of the transient kinetics collected from multiple perovskite domains shows the kinetics of charge carrier recombination vary from domain to domain on the same film. To visualize the extent of variation across a single domain, we collected a series of pump-probe images at increasing pump-probe delays (*i.e.* Fig. 2.5 A Δt = 2 ps; Fig 2.5 B Δt = 400 ps). These delay-dependent images are ordered in sequence, and each single pixel decay trace is fit with a bi-exponential model (Figure 2.5 C). Once the kinetics traces are fit, the model parameters can in turn be used to generate an image reflecting the spatially-dependent recombination dynamics. In principle, both amplitude and lifetime parameters can be plotted to visualize recombination dynamics. However, we have found the PIB half-life, shown in Figure 2.5 D, provides a more concise representation of the complicated recombination dynamics observed in these films.

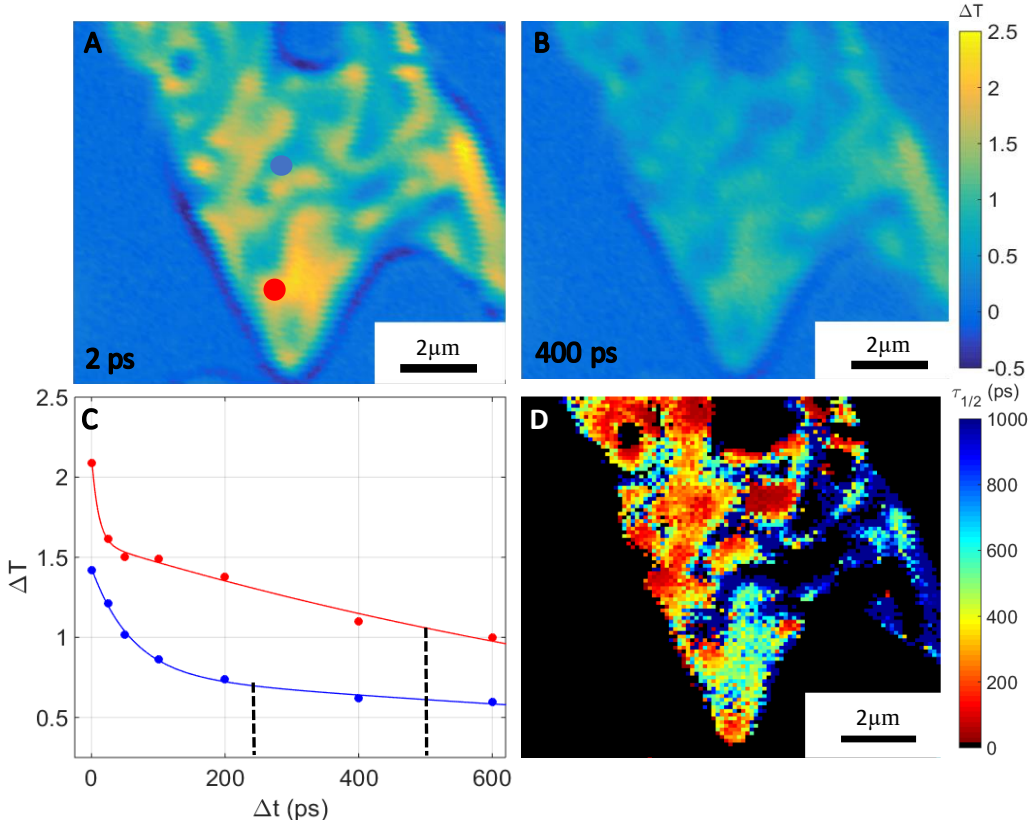

Figure 2.5. Lifetime imaging of $MAPbI_3$ domain. (A,B) Spatially overlapped images taken at Δt = 2 ps (A, reproduced from Fig. 2A) and Δt = 400 ps (B). Color scale for the images is the same. (C) Individual pixel kinetics traces extracted from the series of pump probe images. Red and blue traces represent data from locations indicated by red and blue circles in panel A, respectively. Calculated half-lives are indicated by the dashed lines. (D) Half-life image of domain I. Pump fluence of 72 μJ/cm^2.

As shown in Figure 2.5 D, the half-life varies by over an order of magnitude between fastest and slowest regions, suggesting dramatic variations in trap density are present even on a single domain. While the likely cause of the observed heterogeneity is variation in the surface quality, work has begun in our lab to quantify surface recombination velocities, which can be compared to similar measurements on $MAPbBr_3$ single crystals.[81] Nevertheless, these measurements highlight the need for spatially resolved spectroscopies,[5, 59] as conventional spectroscopic methods that average over the

intrinsic heterogeneity present in OMHP films may obscure the structural and compositional variables relevant to high-performance optoelectronic devices.

2.4 Conclusions

In summary, we have employed time-resolved microscopy to investigate the band edge dynamics of individual domains on $MAPbI_3$ thin films. Recombination kinetics differ from those previously reported in the literature, a result likely due to increased surface recombination in films produced with a solvent-annealing procedure. On ultrafast timescales, our results suggest short-lived photoinduced absorption just below the band gap energy results from a dynamic competition between band filling and band-gap renormalization. The high spatial resolution provided by time-resolved microscopy reveals the extensive spatial heterogeneity in excited state recombination dynamics, adding to the mounting body of evidence that the properties of these materials strongly depend on preparation conditions and local morphology. Together, these findings confirm that the precise correlations between structure and function that ultrafast microscopy provides is essential to optimize the design of ever more efficient OMHP-based optoelectronic devices.

REFERENCES CITED

(3) Mehl, B. P.; Kirschbrown, J. R.; House, R. L.; Papanikolas, J. M. The End Is Different Than the Middle: Spatially Dependent Dynamics in Zno Rods Observed by Femtosecond Pump-Probe Microscopy. *J. Phys. Chem. Lett.* **2011,** *2*, 1777-1781.

(5) Simpson, M. J.; Doughty, B.; Yang, B.; Xiao, K.; Ma, Y.-Z. Spatial Localization of Excitons and Charge Carriers in Hybrid Perovskite Films. *J. Phys. Chem. Lett.* **2015,** *6*, 3041-3047.

(6) Tian, Y.; Merdasa, A.; Peter, M.; Abedellah, M.; Zheng, K.; Jr., C. S. P.; Pullerits, T.; Yartsev, A.; Sundstrom, V.; Scheblykin, I. G. Giant Photoluminescence Blinking of Perovskite Nanocrystals Reveals Single-Trap Control of Luminescence. *Nano Lett.* **2015,** *15*, 1603-1608.

(7) de Quilettes, D. W.; Vorpahl, S. M.; Stranks, S. D.; Nagaoka, H.; Eperon, G. E.; Ziffer, M. E.; Snaith, H. J.; Ginger, D. S. Impact of Microstructure on Local Carrier Lifetime in Perovskite Solar Cells. *Science* **2015,** *348*, 683-686.

(10) Kojima, A.; Teshima, K.; Shirai, Y.; Miyasaka, T. Organometal Halide Perovskites as Visible-Light Sensitizers for Photovoltaic Cells. *J. Am. Chem. Soc.* **2009,** *131*, 6050-6051.

(12) Li, C.-M.; Sjodin, T.; Dai, H.-L. Photoexcited Carrier Diffusion near a Si(111) Surface: Non-Negligible Consequence of Carrier-Carrier Scattering. *Phys. Rev. B* **1997,** *56*, 15252-15255.

(13) Stranks, S. D.; Eperon, G. E.; Grancini, G.; Menelaou, C.; Alcocer, M. J. P.; Leijtens, T.; Herz, L. M.; Petrozza, A.; Snaith, H. J. Electron-Hole Diffusion Lengths Exceeding 1 Micrometer in Organometal Trihalide Perovskite Absorber. *Science* **2013,** *342*, 641-344.

(14) Zhang, W.; Saliba, M.; Moore, D. T.; Pathak, S. K.; Hörantner, M. T.; Stergiopoulos, T.; Stranks, S. D.; Eperon, G. E.; Alexander-Webber, J. A.; Abate, A.; et al. Ultrasmooth Organic-Inorganic Perovskite Thin-Film Formation and Crystallization for Efficient Planar Heterojunction Solar Cells. *Nat. Commun.* **2015,** *6*, 6142.

(15) Guo, Z.; Manser, J. S.; Wan, Y.; Kamat, P. V.; Huang, L. Spatial and Temporal Imaging of Long-Range Charge Transport in Perovskite Thin Films by Ultrafast Microscopy. *Nat. Commun.* **2015,** *6*, 7471.

(16) Christians, J. A.; Manser, J. S.; Kamat, P. V. Multifaceted Excited State of $CH_3NH_3PbI_3$. Charge Separation, Recombination, and Trapping. *J. Phys. Chem. Lett.* **2015,** *6*, 2086-2095.

(17) Manser, J. S.; Kamat, P. V. Band Filling with Free Charge Carriers in Organometal Halide Perovskites. *Nat. Photonics* **2014,** *8*, 737-743.

(18) Im, J.-H.; Jang, I.-H.; Pellet, N.; Grätzel, M.; Park, N.-G. Growth of $CH_3NH_3PbI_3$ Cuboids with Controlled Size for High-Efficiency Perovskite Solar Cells. *Nat. Nanotechnol.* **2014,** *9*, 927-932.

(19) Kim, H.-S.; Im, S. H.; Park, N.-G. Organolead Halide Perovskite: New Horizons in Solar Cell Research. *J. Phys. Chem. C* **2014,** *118*, 5615-5625.

(20) Tan, Z.-K.; Moghaddam, R. S.; Lai, M. L.; Docampo, P.; Higler, R.; Deschler, F.; Price, M.; Sadhanala, A.; Pazos, L. M.; Credgington, D.; et al. Bright Light-Emitting Diodes Based on Organometal Halide Perovskite. *Nat. Nanotechnol.* **2014,** *9*, 687-692.

(21) Zhang, Q.; Ha, S. T.; Liu, X.; Sum, T. C.; Xiong, Q. Room-Temperature near-Infared High-Q Perovskite Whispering-Gallery Planar Nanolasers. *Nano Lett.* **2014,** *14*, 5995-6001.

(22) Fang, Y.; Dong, Q.; Shao, Y.; Yuan, Y.; Huang, J. Highly Narrowband Perovskite Single-Crystal Photodetectors Enabled by Surface-Charge Recombination. *Nat. Photonics* **2015,** *9*, 679-686.

(23) Xing, G.; Matthews, N.; Sun, S.; Lim, S. S.; Lam, Y. M.; Gratzel, M.; Mhaisalkar, S.; T.C., S. Long-Range Balanced Electron- and Hole-Transport Lengths in Organic-Inorganic CH3NH3PbI3. *Science* **2013,** *342*, 344-347.

(24) Lin, Q.; Armin, A.; Nagiri, R. C. R.; Burn, P. L.; Meredith, P. Electro-Optics of Perovskite Solar Cells. *Nat. Photonics* **2014,** *9*, 106-112.

(25) Sun, S.; Salim, T.; Matthews, N.; Duchamp, M.; Boothroyd, C.; Xing, G.; Sum, T. C.; Lam, Y. M. The Origin of High Efficiency in Low-Temperature Solution-Processable Bilayer Organimetal Halide Hybrid Solar Cells. *Energy Environ. Sci* **2014,** *7*, 399-407.

(26) Tian, W.; Zhao, C.; Leng, J.; Cui, R.; Jin, S. Visualizing Carrier Diffusion in Individual Single-Crystal Organolead Halide Perovskite Nanowires and Nanoplates. *J. Am. Chem. Soc.* **2015,** *137*, 12458-12461.

(27) Dong, Q.; Fang, Y.; Shao, Y.; Mulligan, P.; Qiu, J.; Cao, L.; Huang, J. Electron-Hole Diffusion Lengths > 175 Mm in Solution-Grown $CH_3NH_3PbI_3$ Single Crystals. *Science* **2015,** *347*, 967-970.

(44) Sabbah, A. J.; Riffe, D. M. Femtosecond Pump-Probe Reflectivity Study of Silicon Carrier Dynamics. *Phys. Rev. B* **2002,** *66*, 165217.

(47) Berggren, K. F.; Sernelius, B. E. Band-Gap Narrowing in Heavily Doped Many-Valley Semiconductors. *Phys. Rev. B* **1981,** *24*, 1971-1986.

(49) Price, M. B.; Butkus, J.; Jellicoe, T. C.; Sadhanala, A.; Briane, A.; Halpert, J. E.; Broch, K.; Hodgkiss, J. M.; Friend, R. H.; Deschler, F. Hot-Carrier Cooling and Photoinduced Refractive Index Changes in Organic-Inorganic Lead Halide Perovskites. *Nat. Commun.* **2015,** *6*, 8420.

(52) Feneberg, M.; Osterburg, S.; Lange, K.; Lidig, C.; Garke, B.; Goldhahn, R.; Richter, E.; Netzel, C.; Neumann, M. D.; Esser, N.; et al. Band Gap Renormalization and Burstein-Moss Effect in Silicon- and Germanium-Doped Wurtzite Gan up to 10^{20} Cm^{-3}. *Phys. Rev. B* **2014,** *90*, 075203.

(56) Shi, D.; Adinolfi, V.; Comin, R.; Yuan, M.; Alarousu, E.; Buin, A.; Chen, Y.; Hoogland, S.; Rothenberger, A.; Katsiev, K.; et al. Low Trap-State Density and Long Carrier Diffusion in Organolead Trihalide Perovskite Single Crystals. *Science* **2015,** *347*, 519-522.

(57) Savenije, T. J.; Carlito S. Ponseca, J.; Kunneman, L.; Abdellah, M.; Zheng, K.; Tian, Y.; Zhu, Q.; Canton, S. E.; Scheblykin, I. G.; Pullerits, T.; et al. Thermally Activated Exciton Dissociation and Recombination Control the Carrier Dynamics in Organometal Halide Perovskite. *J. Phys. Chem. Lett.* **2014,** *5*, 2189-2194.

(58) Chen, Q.; Zhou, H.; Song, T.-B.; Luo, S.; Hong, Z.; Duan, H.-S.; Dou, L.; Liu, Y.; Yang, Y. Controllable Self-Induced Passivation of Hybrid Lead Iodide Perovskites toward High Performance Solar Cells. *Nano Lett.* **2014,** *14*, 4158-4163.

(59) Draguta, S.; Thakur, S.; Morozov, Y. V.; Wang, Y.; Manser, J. S.; Kamat, P. V.; Kuno, M. Spatially Non-Uniform Trap State Densities in Solution-Processed Hybrid Perovskite Thin Films. *J. Phys. Chem. Lett.* **2016,** *7*, 715-721.

(60) Upadhya, P. C.; Martinez, J. A.; Li, Q.; Wang, G. T.; Swartzentruber, B. S.; Taylor, A. J.; Prasankumar, R. P. Space-and-Time-Resolved Spectroscopy of Single Gan Nanowires. *Appl. Phys. Lett.* **2015,** *106*, 5.

(61) Gabriel, M. M.; Grumstrup, E. M.; Kirschbrown, J. R.; Pinion, C. W.; Christesen, J. D.; Zigler, D. F.; Cating, E. E. M.; Cahoon, J. F.; Papanikolas, J. M. Imaging Charge Separation and Carrier Recombination in Nanowire P-I-N Junctions Using Ultrafast Microscopy. *Nano Lett.* **2014,** *14*, 3079-3087.

(62) Yu, K.; Devadas, M. S.; Major, T. A.; Lo, S. S.; Hartland, G. V. Surface Plasmon Polariton Propagation and Coupling in Gold Nanostructures. *J. Phys. Chem. C* **2014,** *118*, 8603-8609.

(63) Cui, Q.; Ceballos, F.; Kumar, N.; Zhao, H. Transient Absorption Microscopy of Monolayer and Bulk Wse2. *ACS Nano* **2014,** *8*, 2970-2976.

(64) Wong, C. Y.; Cotts, B. L.; Wu, H.; Ginsberg, N. S. Exciton Dynamics Reveal Aggregates with Intermolecular Order at Hidden Interfaces in Solution-Cast Organic Semiconducting Films. *Nat. Commun.* **2015,** *6:594*.

(65) Xiao, Z.; Dong, Q.; Bi, C.; Shao, Y.; Yuan, Y.; Huang, J. Solvent Annealing of Perovskite-Induced Crystal Growth for Photovoltaic-Device Efficiency Enhancement. *Adv. Mater.* **2014,** *26*, 6503-6509.

(66) Im, J.-H.; Luo, J.; Franckevicius, M.; Pellet, N.; Gao, P.; Moehl, T.; Zakeeruddin, S. M.; Nazeeruddin, M. K.; Gratzel, M.; Park, N.-G. Nanowire Perovskite Solar Cell. *Nano Lett.* **2015,** *15*, 2120-2126.

(67) Lee, M. M.; Teuscher, J.; Miyasaka, T.; Murakami, T. N.; Snaith, H. J. Efficient Hybrid Solar Cells Based on Meso-Superstructured Organometal Halide Perovskites. *Science* **2012,** *338*, 643-647.

(68) Liu, J.; Gao, C.; He, X.; Ye, Q.; Ouyang, L.; Zhuang, D.; Liao, C.; Mei, J.; Lau, W. Improved Crystallization of Perovskite Films by Optimized Solvent Annealing for High Efficiency Solar Cell. *ACS Appl. Mater. Interfaces* **2015,** *7*, 24008-24015.

(69) Nie, W.; Tsai, H.; Asadpour, R.; Blancon, J.-C.; Neukirch, A. J.; Gupta, G.; Crochet, J. J.; Chhowalla, M.; Tretiak, S.; Alam, M. A.; et al. High-Efficiency Solution-Processed Perovskite Solar Cells with Milimeter-Scale Grains. *Science* **2015,** *347*, 522-525.

(70) Wu, X.; Trinh, M. T.; Niesner, D.; Zhu, H.; Norman, Z.; Owen, J. S.; Yaffe, O.; Kudisch, B. J.; X.Y.Zhu. Trap States in Lead Iodide Perovskites. *J. Am. Chem. Soc.* **2015,** *137*, 2089-2096.

(71) Deschler, F.; Price, M.; Pathak, S.; Klintberg, L. E.; Jarausch, D.-D.; Higler, R.; Huttner, S.; Leijtens, T.; Stranks, S. D.; Snaith, H. J.; et al. High Photoluminescence Efficiency and Optically Pumped Lasing in Soulution-Processed Mixed Halide Perovskite Semiconductors. *J. Phys. Chem. Lett.* **2014,** *5*, 1421-1426.

(72) Chen, K.; Barker, A. J.; Morgan, F. L. C.; Halptert, J. E.; Hodgkiss, J. M. The Effect of Carrier Thermalization Dynamics on Light Emission and Amplification in Organometal Halide Perovskites. *J. Phys. Chem. Lett.* **2015,** *6*, 153-158.

(73) Gong, T.; Nighan, W. L.; Fauchet, P. M. Hot-Carrier Coulomb Effects in GaAs Investigated by Femtosecond Spectroscopy around the Band Edge. *Appl. Phys. Lett.* **1990,** *57*, 2713-2715.

(74) Fu, J.; Xu, Q.; Han, G.; Wu, B.; Huan, C. H. A.; Leek, M. L.; Sum, T. C. Hot Carrier Cooling Mechanisms in Halide Perovskites. *Nat. Commun.* **2017,** *8*, 1300.

(75) Ponseca, C. S.; Savenije, T. J.; Abdellah, M.; Zheng, K.; Yartsev, A.; Pascher, T.; Harlang, T.; Chabera, P.; Pullerits, T.; Stepanov, A.; et al. Organometal Halide Perovskite Solar Cells Rationalized: Ultrafast Charge Generation, High and Microsecond-Long Balanced Mobilities, and Slow Recombination. *J. Am. Chem. Soc.* **2014,** *136*, 5189-5192.

(76) Stamplecoskie, K. G.; Manser, J. S.; Kamat, P. V. Dual Nature of the Excited State in Organic-Inorganic Lead Halide Perovskites. *Energy Environ. Sci.* **2015,** *8*, 208-215.

(77) Aspnes, D. E. Recombination at Semiconductor Surfaces and Interfaces. *Surf. Sci.* **1983,** *132*, 406-421.

(78) Ziang, X.; Shifeng, L.; Laixiang, Q.; Shuping, P.; Wei, W.; Yu, Y.; Li, Y.; Zhijian, C.; Shufeng, W.; Honglin, D.; et al. Refractive Index and Extinction Coefficient of CH3NH3PbI3 Studied by Spectroscopic Ellipsometry. *Opt. Mater. Express* **2014,** *5*, 29-43.

(79) Yang, Y.; Ostrowski, D. P.; France, R. M.; Zhu, K.; van de Lagemaat, J.; Luther, J. M.; Beard, M. C. Observation of a Hot-Phonon Bottleneck in Lead-Iodide Perovskites. *Nat. Photonics* **2016,** *10*, 53-59.

(80) Yang, J.; Wen, X.; Xia, H.; Sheng, R.; Ma, Q.; Kim, J.; Tapping, P.; Harada, T.; Kee, T. W.; Huang, F.; et al. Acoustic-Optical Phonon up-Conversion and Hot-Phonon Bottleneck in Lead-Halide Perovskites. *Nat. Commun.* **2017,** *8*, 14120.

(81) Yang, Y.; Yan, Y.; Yang, M.; Choi, S.; Zhu, K.; Luther, J. M.; Beard, M. C. Low Surface Recombination Velocity in Solution-Grown $CH_3NH_3PbBr_3$ Perovskite Single Crystal. *Nat. Commun.* **2015,** *6:7961*.

CHAPTER THREE

SCREENED CHARGE CARRIER TRANSPORT IN METHYLAMMONIUM LEAD IODIDE PEROVSKITE THIN FILMS

Contributions of Authors and Co-Authors

Manuscript: Screened Charge Carrier Transport in Methylammonium Lead Iodide Perovskite Thin Films

Author: Andrew H. Hill

Contributions: Synthesized and characterized all samples. Collected and analyzed all ultrafast microscopic data. Assisted in writing and editing manuscript.

Author: Kori E. Smyser

Contributions: Aided in development of synthetic protocols used to produce all samples studied in this work.

Author: Casey L. Kennedy

Contributions: Aided in analysis of ultrafast microscopic data. Provided valuable feedback on early drafts of manuscript.

Author: Eric S. Massaro

Contributions: Aided in analysis of ultrafast microscopic data. Provided valuable feedback on early drafts of manuscript.

Author: Erik M. Grumstrup

Contributions: Assisted with analysis and editing of manuscript for final submission.

Manuscript Information Page

Andrew H. Hill, Kori E. Smyser, Casey L. Kennedy, Eric S. Massaro, Erik M. Grumstrup
Journal of Physical Chemistry Letters

Status of Manuscript:
____ Prepared for submission to a peer-reviewed journal
____ Officially submitted to a peer-review journal
____ Accepted by a peer-reviewed journal
_X_ Published in a peer-reviewed journal

Published by the American Chemical Society
Submitted January 8, 2017
Accepted February 9, 2017
Volume 8, Issue 5, 948-953

CHAPTER 3

SCREENED CHARGE CARRIER TRANSPORT IN METHYLAMMONIUM LEAD IODIDE PEROVSKITE THIN FILMS

3.1 Introduction

Chapter 2 focused on characterizing the relaxation dynamics of photogenerated carriers in $MAPbI_3$. Throughout the course of that work significant heterogeneity was identified in both the photoresponse and recombination dynamics of single $MAPbI_3$ domains, highlighting the need for spatially resolved spectroscopies to provide a robust characterization of $MAPbI_3$. Following the relatively broad scope of the work presented in Chapter 2, Chapter 3 focuses on characterizing charge carrier transport in $MAPbI_3$. Despite advances in many applications and a flurry of research activity, a fundamental understanding of how the material parameters govern charge carrier transport in lead-halide perovskites is not yet established, preventing a rational approach toward optimizing carrier transport in optoelectronic devices. While transport properties have been characterized through a variety of techniques[13, 15-16, 23, 26, 57], reported diffusion and mobility parameters vary widely, reflecting, at least in part, differences in domain size and the relative importance of grain boundaries to experimental observables.[82, 83] Carriers generated near multiple grain boundaries exhibit diminished mobility relative to those generated in large, single-crystalline domains. Thus, the morphological heterogeneity of organometal halide perovskite thin films introduced by solution-processing techniques complicates efforts directed toward uncovering the intrinsic material transport parameters.

To overcome these challenges, we utilize pump-probe microscopy (PPM) together with scanning electron microscopy (SEM) to interrogate the intrinsic transport properties of methylammonium lead iodide ($MAPbI_3$) thin films. As demonstrated in Chapter 2, PPM provides sufficient spatial resolution to isolate individual, single crystal $MAPbI_3$ domains of a thin film while excluding dynamics associated with scattering from grain boundaries and other morphological defects. By directly imaging carrier transport on 25 individual domains, we show that the transport properties of $MAPbI_3$ thin films are comparable to those previously observed in single crystals, suggesting that excellent, long-range carrier mobilities are achievable, even in thin film morphologies. In addition, we also measure carrier diffusion in single $MAPbI_3$ domains while varying carrier density over nearly two orders of magnitude. Analysis of the density-dependent behavior implicates strong carrier-phonon scattering and a large effective dielectric constant as the primary determiners of charge transport up to carrier densities of ~ 1×10^{19} cm^{-3}. At higher densities, the observed diffusivity increases modestly due to non-degenerate carrier populations.

3.2 Experimental

3.2.1 Thin Film Preparation and Characterization

The thin film samples used in this work were prepared and annealed identically to those discussed in Chapter 2. After annealing, samples were sealed from the ambient atmosphere using microscope slide cover slips and optical adhesive in preparation for ultrafast microscopic characterization. Samples were also characterized using scanning

electron microscopy, X-Ray Diffraction, and UV-Vis spectroscopy. In all cases these measurements were performed after samples underwent ultrafast spectroscopic characterization.

3.3 Results and Discussion

Figure 3.1 presents a series of correlated PPM – SEM measurements performed on an individual $MAPbI_3$ domain. The pump-probe image of the domain, collected by scanning the sample underneath spatially-overlapped pump (λ_{pump} = 600 nm) and probe beams (λ_{probe} = 785 nm), is shown in panel A of Figure 3.1. Because of the high spatial resolution (400 nm FWHM) determined by the overlap of the tightly focused pump and probe beams, strong fringes appear in the image, reflecting transient shifting of (probe beam) Fabry-Perot resonances in the domain. At delay times longer than ~ 2 ps, the transient response reflects a combination of stimulated emission, band filling, and refractive index changes due to the presence of photogenerated charge carriers.[17, 49] The correlated scanning electron microscope (SEM) image of the same domain is shown in panel B of Figure 3.1.

Carrier transport in individual domains is measured by imaging the spatial evolution of the ambipolar (electrons and holes) charge carrier cloud photoexcited by a pump pulse focused to a sub-micron spot size. The excited charge carriers diffuse under a concentration gradient, and are imaged with a delayed probe pulse that can be independently positioned with respect to the pump. Figure 3.1 C shows three such spatially-separated pump-probe images collected from the location indicated by the red

circles on in panels A and B of Figure 3.1. As the delay time is increased from Δt = 5 ps to 800 ps, the spot grows in diameter, reflecting the diffusive motion of the charge carriers through the $MAPbI_3$ domain.

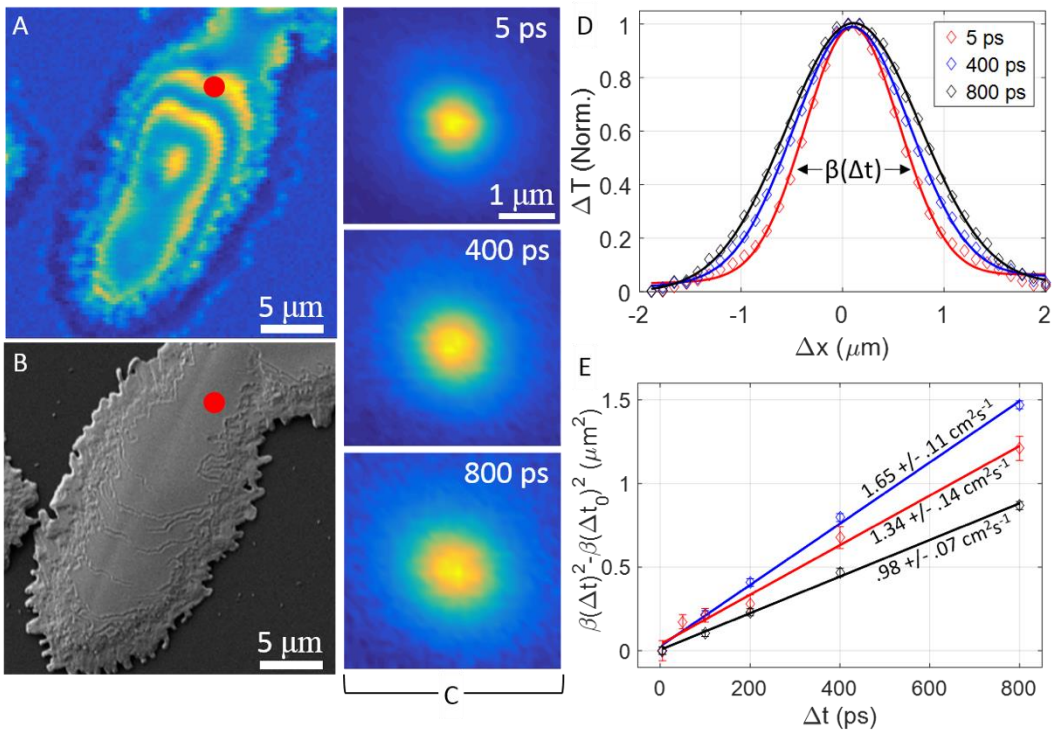

Figure 3.1. Characterization of a perovskite domain by spatially separated pump-probe microscopy. (A) Pump-probe image of perovskite domain at Δt = 5 ps. (B) Field emission micrograph of domain imaged in panel A. (C) Images of delay-dependent photogenerated carrier cloud collected from location indicated by the red circles in panels A and B. (D) Normalized carrier distribution profiles (colored diamonds) and fits (solid lines) used to extract carrier diffusivity. (E) Compiled diffusion data taken from three individual domains on the same thin film.

The broadening of the profile can be more clearly seen if the images in column C are integrated along (for example) the vertical axis. Figure 3.1 D shows normalized, integrated carrier distribution profiles at Δt = 5 ps, 400 ps, and 800 ps. Each profile can be fit with a model (solid lines) which convolves together the finite width Gaussian

profiles of the pump and probe beams with the Δt-dependent component arising from charge carrier diffusion.[84] The time-dependent change of the FWHM of the profile is given by Equation 1.3 which is reproduced below for clarity:

$$\Delta\beta = [\beta(t_0)^2 + 16\ln(2)\, D \cdot (\Delta t - t_0)]^{1/2} \quad (3.1)$$

In the limit of diffusive motion, plotting the change in the square of the fwhm as a function of pump-probe delay yields a line whose slope is proportional to the ambipolar charge carrier diffusion constant.[85] Figure 3.1 E shows three sets of diffusion data collected from three separated $MAPbI_3$ domains. The square of the profile fwhm broadens linearly with time, strongly suggesting diffusive motion to be the cause.

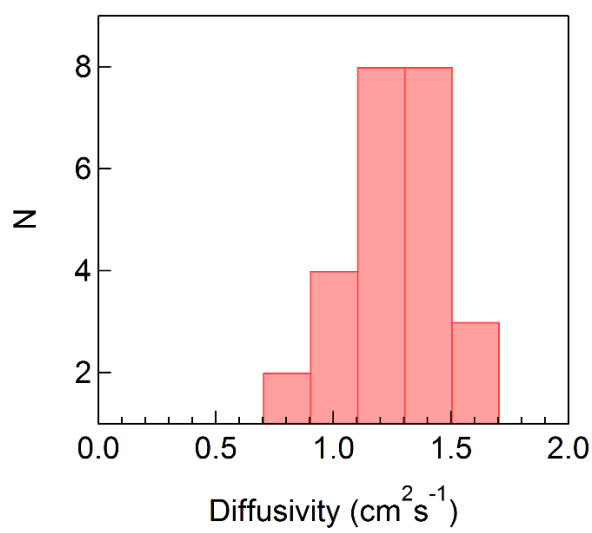

Figure 3.2. Distribution of measured carrier diffusivities for 25 individual $MAPbI_3$ domains.

In Figure 3.2, we show diffusivities determined from PPM measurements performed on 25 individual $MAPbI_3$ domains. For each individual domain, we verified the decay kinetics were power-independent at the pump fluence and location diffusion was measured. Multiple kinetics scans were taken at locations from which diffusion data

was collected. The first scan was performed at the projected pump fluence and the fluence was reduced by a factor of two for the second scan. Kinetics were deemed power independent if the two traces, when normalized, traced an identical decay path. Several examples of this are shown in Figure 3.3.

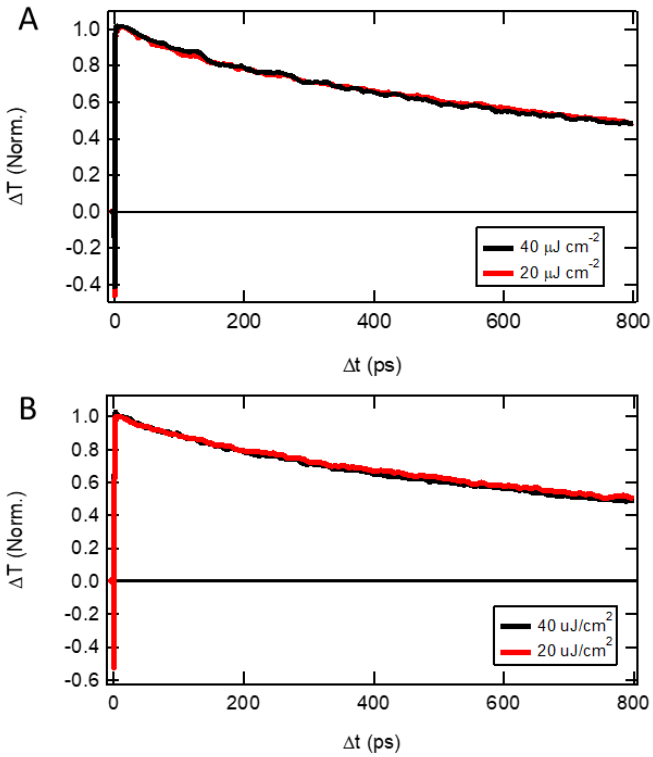

Figure 3.3. Power independent kinetics traces of $MAPbI_3$ crystallites. (A, B) Example decay traces showing power independent recombination dynamics in two separate $MAPbI_3$ domains.

If unaccounted for, density dependent recombination will artificially increase the determined diffusion constant because the center (higher carrier density region) of the photogenerated carrier cloud undergoes faster decay than the (lower density) edges.[4] On average, it was determined if pump fluences exceeded ~40 uJ/cm^2 nonlinear recombination began to influence the observed kinetics. Below this fluence, we attribute

the decay kinetics to a combination of surface recombination[58, 86] and diffusion of carriers out of the probe volume[84]. Despite excluding measurements performed on or near grain boundaries, we find diffusion constants vary between 0.74 $cm^2 \cdot s^{-1}$ and 1.77 $cm^2 \cdot s^{-1}$. Note that diffusivity can be related to the more commonly encountered (ambipolar) mobility (μ_A = 28 $cm^2/V \cdot s$ - 68 $cm^2/V \cdot s$) through the Einstein relation ($D = \mu_A kT/q$). While the cause of the factor of three difference in domain-to-domain transport characteristics is not yet known, the diffusion constants we find in these thin films are significantly greater than those previously determined in $MAPbI_3$ thin films with ultrafast microscopy,[15] but closely comparable to mobilities obtained with transient microwave conductivity.[75] Because microwave conductivity probes the motion of carriers on the nanometer length scale,[87] it is not surprising that higher mobility values are found relative to the microscopy approach, which measures transport on 100-1000 nm length scales. Carriers diffusing along single nanometer length scales will experience, on average, a far more homogeneous crystal environment than those traveling over a micron. However, we note that the diffusion constants we find for thin film morphologies are also closely comparable to values reported for $MAPbI_3$ bulk single crystals[27, 56, 88] and nanostructures,[26] suggesting that preparation conditions, crystal quality, and grain boundary density are critical for ensuring optimal carrier transport, particularly over length scales greater than 10 – 100 nm.

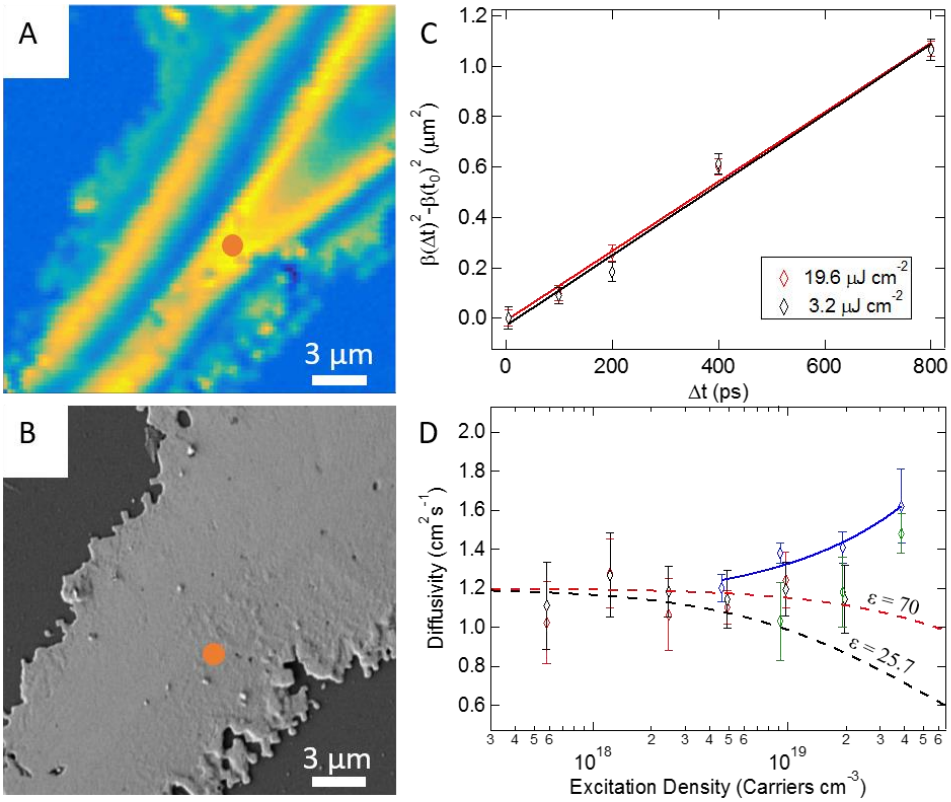

Figure 2.4. (A) Pump-probe image of a single $MAPbI_3$ domain. (B) Corresponding scanning electron micrograph of the domain in panel A. (C) Time-dependent fwhm^2 of charge carrier distributions after pump excitations of 3.2 and 19 µJ cm^{-2}. Data were collected from locations indicated by red circles in panels A and B. (D) Excitation fluence dependence of carrier diffusivity in $MAPbI_3$ perovskite. Error bars represent 90% confidence intervals. Data represented by red diamonds are collected from red spot in panel B. Data represented by black, blue, and green diamonds was collected from individual domains all displaying similar low-density diffusivities. The red and black dashed lines depict predicted diffusivities as calculated by Eqn. 3.2 using relative static permittivities of 70 and 25.7, respectively. The solid blue line is a fit of the blue diamonds to Eqn. 3.3 demonstrating $n^{2/3}$ dependence of the ambipolar diffusivity.

To determine the impact of carrier density on ambipolar diffusion in $MAPbI_3$, we next measured the diffusion constant (as outlined in Figure 3.1) of individual domains over a range of excitation fluences. Figure 3.4 shows correlated PPM and SEM images of one such perovskite domain in panels A and B, respectively. In Figure 3.4 C, we show representative plots of $\Delta\beta^2$ vs. Δt, as determined from spatially separated images

collected at the location indicated on panels A and B, for pump fluences of 3.2 uJ/cm^2 and 19.6 uJ/cm^2. Linear fits to the data (solid lines) recover diffusion constants (D = 1.2 cm^2/s) that are independent of pump intensity within error. Similar behavior was observed in all domains we investigated. Figure 3.4 D summarizes the density dependent ambipolar diffusion constants (with 90% confidence intervals) measured on four individual $MAPbI_3$ domains. No change in diffusivity is observed between 6 x 10^{17} cm^{-3} - ~1 x 10^{19} cm^{-3}, however at higher carrier densities, a moderate increase in diffusivity can be observed. We note the carrier density reported in Figure 3.4 is calculated by averaging over the photoexcitation volume bounded by the 1/e width of the Gaussian pump spot (800 nm) and the 1/e absorption depth (assuming Beer-Lambert absorption) at λ_{pump} = 600 nm (for full details, see Appendix A).

To understand the observed trend in density-dependent diffusivity, we first discuss our results within the context of carrier-carrier scattering. It is well-established that charge carrier mobility and diffusivity are strongly reduced by Coulomb scattering when densities exceed ~10^{17} cm^{-3}, as described by Chapman and Cowling[89] and applied to doped semiconductors by Fletcher.[90] Experimental measurements of density-dependent ambipolar diffusion in Si[12], GaAs[91] and InGaAsP[92] multiple quantum wells have largely verified Fletcher's expression that describes the diffusivity arising from carrier-carrier scattering as (*in SI units*):

$$D_{eh} = 48\pi^{3/2}2^{-3/2}n^{-1}\epsilon^2{\epsilon_0}^2q^{-4}\left(\frac{m_e+m_h}{m_e m_h}\right)^{1/2}\frac{(\mathrm{kT})^{5/2}}{\mathrm{Log}[1+256\epsilon^2{\epsilon_0}^2n^{-2/3}q^{-4}\mathrm{k}^2\mathrm{T}^2]} \quad (3.2)$$

Here, n is the carrier density, ϵ is the static relative permittivity of the material, ϵ_0 the permittivity of vacuum, q the carrier charge, kT thermal energy, and m_e and m_h the

electron and hole effective masses, respectively. The overall (observed) diffusion constant, D is given by a sum of reciprocals (Mathiessen rule) of the intrinsic (low density) diffusion constant with the carrier-carrier scattering term:

$$\frac{1}{D} = \frac{1}{D_i} + \frac{1}{D_{eh}} \qquad (3.3)$$

For common inorganic semiconductors, carrier-carrier scattering significantly decreases diffusivity at high carrier densities. For example, as shown by Dai *et al.*, a factor of four drop in diffusivity is seen in silicon over the same range of carrier densities presented in Figure 3.4, a result correctly modeled by Equations. 3.2 and 3.3.[12]

We identify two causes for the significantly reduced effects of carrier-carrier scattering in $MAPbI_3$ relative to traditional inorganic semiconductors. The first is that the static relative permittivity in $MAPbI_3$ is much greater than that in Si (11.7) or GaAs (13.1), strongly screening the Coulomb interaction between charge carriers (or between carriers and trap sites, see below). The red and black dashed lines in Figure 3.4 shows diffusivity predicted by Equations. 3.1 and 3.2 for two reported values of the static relative permittivity in $MAPbI_3$ (ϵ = 25.7[93] and ϵ = 70[24], respectively), assuming m_e = .23m_0 and m_h = .29m_0,[94] T = 300 K, and a low-density diffusion constant D_i = 1.2 $cm^2 \cdot s^{-1}$. Comparison between the data and model suggests that in these high-performing films we investigated, the static relative permittivity is closer to the higher end of this range.

However, the strong Coloumb screening imposed by the material's large relative permittivity is insufficient to describe the atypical density independence exhibited by $MAPbI_3$. For example, if Si had a static relative permittivity of 70, Equations 3.2 and 3.3 predict the diffusivity would still drop by a factor of two at ~ 10^{19} carriers cm^{-3}. The

additional factor that contributes to the observed density independence is that the intrinsic diffusivity (and mobility) of $MAPbI_3$, D_i, is nearly a factor of ten lower than many inorganic semiconductors. As a result, even at photoexcitation densities of ~ 10^{19} cm^{-3}, carrier motion is dominated not by carrier-carrier scattering (D_{eh}), but rather by the scattering process responsible for the low intrinsic diffusivity, D_i. Because the density-independence up to ~ 10^{19} cm^{-3} shows that carriers are largely screened from Coulombic interactions with other charged centers in the lattice (both other carriers and trap sites), we conclude that the intrinsic transport characteristics of $MAPbI_3$ are determined by strong carrier-phonon coupling. This conclusion is in agreement with previously reported temperature dependent studies where mobility in $MAPbI_3$ was observed to scale as $T^{-1.6}$.[95] The fact that D_i is relatively low reflects the comparatively stronger carrier-phonon coupling in the highly polar $MAPbI_3$ than is typically seen in inorganic semiconductors. Thus, efforts directed toward improving carrier mobility in lead halide perovskites should focus on reducing the carrier-phonon coupling, while balancing the possible beneficial effects of large polaron formation.[88, 96]

At higher photoexcitation densities, carrier diffusivities show a modest increase. We attribute this trend to the greater mobility of non-band edge states occupied at high carrier densities.[12] As injection density increases, band edge states fill and carriers are forced to occupy states with energies above the band minimum. At high carrier densities when the band-edge degeneracy is broken, the ambipolar diffusivity can be expressed as:[97]

$$D = \left[\left(\frac{\pi}{6}\right)^{1/3}\left(\frac{n}{N_{c,v}}\right)^{2/3} + 1\right] D_i \qquad (3.4)$$

Here n is the injected carrier density and $N_{c,v}$ is the average density of states of the conduction and valence bands. Diffusion measurements displaying a thermal increase can be well fit with Equation 3.4 (see blue trace, Fig. 3.4), returning $N_{c,v}$ values from 6.0×10^{19} - 1.3×10^{20} cm^{-3}. While the density of states determined from Equation 3.4 are relatively high compared to conventional semiconductors, we note that density-dependent recombination and carrier-carrier scattering effects likely impact the determined density. Nevertheless, as shown in Figure 3.4, the modest increase in carrier diffusivity scales as $n^{2/3}$, in agreement with the behavior expected for non-degenerate diffusion (the process by which carriers lying higher in energy than the low-energy edges of the valence and conduction bands diffuse more rapidly than those at the band edges). We also note that the critical excitation fluence where non-degenerate behavior begins to influence diffusion exceeds the regime where a phonon bottleneck has been previously reported.[49, 79-80] While a phonon-induced, long-lived hot carrier population would give rise to a modest diffusivity enhancement in a manner analogous to non-degeneracy effects, the measurements performed here are likely insensitive to such effects given the previously reported timescales (~ 1 ps) of carrier cooling under 600 nm photoexcitation.

When possible all measurements of carrier diffusion were performed while ensuring higher-order electron-hole recombination was absent, as indicated by power-independent spatially overlapped kinetics collected at the same location (see above). However, we note that at the elevated fluences where nondegenerate diffusion processes typically take place, decay dynamics occasionally display slight dependence on carrier density. To compensate for this, diffusion constants were extracted from linear fits of time

points after ~200 ps, where nonlinear recombination has a smaller effect on the observed diffusion.

3.4 Conclusions

In conclusion, we have measured the local ambipolar transport properties of charge carriers in individual $MAPbI_3$ domains. Although significant domain-to-domain variation exists, thin-film morphologies can be fabricated that exhibit diffusivities comparable to single-crystals. Efforts are ongoing to identify the cause of inter-domain variability in carrier transport. We also present data showing that carrier transport in $MAPbI_3$ perovskites is independent of carrier density up to ~10^{19} cm^{-3}. These results implicate a high static dielectric constant, which screens photoexcited carriers from interactions with other charged centers in the lattice, and strong carrier-phonon coupling as the determining factors in $MAPbI_3$ transport properties. At injection densities above ~10^{19} cm^{-3} carrier diffusivities increase as $n^{2/3}$, indicating breakdown in the excited carrier degeneracy.

REFERENCES CITED

(12) Li, C.-M.; Sjodin, T.; Dai, H.-L. Photoexcited Carrier Diffusion near a Si(111) Surface: Non-Negligible Consequence of Carrier-Carrier Scattering. *Phys. Rev. B* **1997,** *56*, 15252-15255.

(13) Stranks, S. D.; Eperon, G. E.; Grancini, G.; Menelaou, C.; Alcocer, M. J. P.; Leijtens, T.; Herz, L. M.; Petrozza, A.; Snaith, H. J. Electron-Hole Diffusion Lengths Exceeding 1 Micrometer in Organometal Trihalide Perovskite Absorber. *Science* **2013,** *342*, 641-344.

(15) Guo, Z.; Manser, J. S.; Wan, Y.; Kamat, P. V.; Huang, L. Spatial and Temporal Imaging of Long-Range Charge Transport in Perovskite Thin Films by Ultrafast Microscopy. *Nat. Commun.* **2015,** *6*, 7471.

(16) Christians, J. A.; Manser, J. S.; Kamat, P. V. Multifaceted Excited State of $CH_3NH_3PbI_3$. Charge Separation, Recombination, and Trapping. *J. Phys. Chem. Lett.* **2015,** *6*, 2086-2095.

(17) Manser, J. S.; Kamat, P. V. Band Filling with Free Charge Carriers in Organometal Halide Perovskites. *Nat. Photonics* **2014,** *8*, 737-743.

(23) Xing, G.; Matthews, N.; Sun, S.; Lim, S. S.; Lam, Y. M.; Gratzel, M.; Mhaisalkar, S.; T.C., S. Long-Range Balanced Electron- and Hole-Transport Lengths in Organic-Inorganic CH3NH3PbI3. *Science* **2013,** *342*, 344-347.

(24) Lin, Q.; Armin, A.; Nagiri, R. C. R.; Burn, P. L.; Meredith, P. Electro-Optics of Perovskite Solar Cells. *Nat. Photonics* **2014,** *9*, 106-112.

(26) Tian, W.; Zhao, C.; Leng, J.; Cui, R.; Jin, S. Visualizing Carrier Diffusion in Individual Single-Crystal Organolead Halide Perovskite Nanowires and Nanoplates. *J. Am. Chem. Soc.* **2015,** *137*, 12458-12461.

(27) Dong, Q.; Fang, Y.; Shao, Y.; Mulligan, P.; Qiu, J.; Cao, L.; Huang, J. Electron-Hole Diffusion Lengths > 175 Mm in Solution-Grown $CH_3NH_3PbI_3$ Single Crystals. *Science* **2015,** *347*, 967-970.

(49) Price, M. B.; Butkus, J.; Jellicoe, T. C.; Sadhanala, A.; Briane, A.; Halpert, J. E.; Broch, K.; Hodgkiss, J. M.; Friend, R. H.; Deschler, F. Hot-Carrier Cooling and Photoinduced Refractive Index Changes in Organic-Inorganic Lead Halide Perovskites. *Nat. Commun.* **2015,** *6*, 8420.

(56) Shi, D.; Adinolfi, V.; Comin, R.; Yuan, M.; Alarousu, E.; Buin, A.; Chen, Y.; Hoogland, S.; Rothenberger, A.; Katsiev, K.; et al. Low Trap-State Density and Long Carrier Diffusion in Organolead Trihalide Perovskite Single Crystals. *Science* **2015,** *347*, 519-522.

(57) Savenije, T. J.; Carlito S. Ponseca, J.; Kunneman, L.; Abdellah, M.; Zheng, K.; Tian, Y.; Zhu, Q.; Canton, S. E.; Scheblykin, I. G.; Pullerits, T.; et al. Thermally Activated Exciton Dissociation and Recombination Control the Carrier Dynamics in Organometal Halide Perovskite. *J. Phys. Chem. Lett.* **2014,** *5*, 2189-2194.

(58) Chen, Q.; Zhou, H.; Song, T.-B.; Luo, S.; Hong, Z.; Duan, H.-S.; Dou, L.; Liu, Y.; Yang, Y. Controllable Self-Induced Passivation of Hybrid Lead Iodide Perovskites toward High Performance Solar Cells. *Nano Lett.* **2014,** *14*, 4158-4163.

(75) Ponseca, C. S.; Savenije, T. J.; Abdellah, M.; Zheng, K.; Yartsev, A.; Pascher, T.; Harlang, T.; Chabera, P.; Pullerits, T.; Stepanov, A.; et al. Organometal Halide Perovskite Solar Cells Rationalized: Ultrafast Charge Generation, High and Microsecond-Long Balanced Mobilities, and Slow Recombination. *J. Am. Chem. Soc.* **2014,** *136*, 5189-5192.

(79) Yang, Y.; Ostrowski, D. P.; France, R. M.; Zhu, K.; van de Lagemaat, J.; Luther, J. M.; Beard, M. C. Observation of a Hot-Phonon Bottleneck in Lead-Iodide Perovskites. *Nat. Photonics* **2016,** *10*, 53-59.

(80) Yang, J.; Wen, X.; Xia, H.; Sheng, R.; Ma, Q.; Kim, J.; Tapping, P.; Harada, T.; Kee, T. W.; Huang, F.; et al. Acoustic-Optical Phonon up-Conversion and Hot-Phonon Bottleneck in Lead-Halide Perovskites. *Nat. Commun.* **2017,** *8*, 14120.

(82) Reid, O. G.; Yang, M.; Kopidakis, N.; Zhu, K.; Rumbles, G. Grain-Size-Limited Mobility in Methylammonium Lead Iodide Perovskite Thin Films. *ACS Energy Lett.* **2016,** *1*, 561-565.

(83) Grancini, G.; Viola, D.; Gandini, M.; Altamura, D.; Pogna, E. A. A.; D'Innocenzo, V.; Bargigia, I.; Giannini, C.; Cerullo, G.; Petrozza, A. Lattice Distortions

Drive Electron–Hole Correlation within Micrometer-Size Lead-Iodide Perovskite Crystals. *ACS Energy Lett.* **2016,** *2*, 265-269.

(84) Grumstrup, E. M.; Gabriel, M. M.; Cating, E. M.; Pinion, C. W.; Christesen, J. D.; Kirschbrown, J. R.; Vallorz, E. L.; Cahoon, J. F.; Papanikolas, J. M. Ultrafast Carrier Dynamics in Individual Silicon Nanowires: Characterization of Diameter-Dependent Carrier Lifetime and Surface Recombination with Pump-Probe Microscopy. *J. Phys. Chem. C* **2014,** *118*, 8634-8640.

(85) Smith, L. M.; Wake, D. R.; Wolfe, J. P.; Levi, D.; Klein, M. V.; Klem, J.; Henderson, T.; Morkoç, H. Picosecond Imaging of Photoexcited Carriers in Quantum Wells: Anomalous Lateral Confinement at High Densities. *Phys. Rev. B* **1988,** *38*, 5788-5791.

(86) Stewart, R. J.; Grieco, C.; Larsen, A. V.; Maier, J. J.; Asbury, J. B. Approaching Bulk Carrier Dynamics in Organo-Halide Perovskite Nanocrystalline Films by Surface Passivation. *J. Phys. Chem. Lett.* **2016,** *7*, 1148-1153.

(87) Savenije, T. J.; Ferguson, A. J.; Kopidakis, N.; Rumbles, G. Revealing the Dynamics of Charge Carriers in Polymer:Fullerene Blends Using Photoinduced Time-Resolved Microwave Conductivity. *J. Phys. Chem. C* **2013,** *117*, 24085-24103.

(88) Chen, Y.; Yi, H. T.; Wu, X.; Haroldson, R.; Gartstein, Y. N.; Rodionov, Y. I.; Tikhonov, K. S.; Zakhidov, A.; Zhu, X. Y.; Podzorov, V. Extended Carrier Lifetimes and Diffusion in Hybrid Perovskites Revealed by Hall Effect and Photoconductivity Measurements. *Nat. Commun.* **2016,** *7*, 12253.

(89) S. Chapman, T. G. C. *Mathematical Theory of Non-Uniform Gases*. 3rd ed.; Cambridge University Press: 1970.

(90) Fletcher, N. H. The High Current Limit for Semiconductor Junction Devices. *Proceedings of the IRE* **1957,** *45*, 862-872.

(91) Akiyama, H.; Matsusue, T.; Sakaki, H. Carrier Scattering and Excitonic Effects on Electron-Hole-Pair Diffusion in Nondoped and P -Type-Modulation-Doped GaAs/Al(X)Ga(1-X)as Quantum-Well Structures. *Phys. Rev. B* **1994,** *49*, 14523-14530.

(92) Zhu, D. X.; Dubovitsky, S.; Steier, W. H.; Burger, J.; Tishinin, D.; Uppal, K.; Dapkus, P. D. Ambipolar Diffusion Coefficient and Carrier Lifetime in a Compressively Strained InGaAsP Multiple Quantum Well Device. *Appl. Phys. Lett.* **1997,** *71*, 647-649.

(93) Frost, J. M.; Butler, K. T.; Brivio, F.; Hendon, C. H.; van Schilfgaarde, M.; Walsh, A. Atomistic Origins of High-Performance in Hybrid Halide Perovskite Solar Cells. *Nano Lett.* **2014,** *14*, 2584-2590.

(94) Giorgi, G.; Fujisawa, J.-I.; Segawa, H.; Yamashita, K. Small Photocarrier Effective Masses Featuring Ambipolar Transport in Methylammonium Lead Iodide Perovskite: A Density Functional Analysis. *J. Phys. Chem. Lett.* **2013,** *4*, 4213-4216.

(95) Savenije, T. J.; Ponseca, C. S.; Kunneman, L.; Abdellah, M.; Zheng, K.; Tian, Y.; Zhu, Q.; Canton, S. E.; Scheblykin, I. G.; Pullerits, T.; et al. Thermally Activated Exciton Dissociation and Recombination Control the Carrier Dynamics in Organometal Halide Perovskite. *J. Phys. Chem. Lett.* **2014,** *5*, 2189-2194.

(96) Zhu, H.; Miyata, K.; Fu, Y.; Wang, J.; Joshi, P. P.; Niesner, D.; Williams, K. W.; Jin, S.; Zhu, X.-Y. Screening in Crystalline Liquids Protects Energetic Carriers in Hybrid Perovskites. *Science* **2016,** *353*, 1409-1413.

(97) Silard, A. P.; Duta, M. J. Majority Carrier Diffusion Coefficients in Degenerately Doped Silicon. *J. Appl. Phys.* **1987,** *62*, 3809-3812.

CHAPTER FOUR

PEROVSKITE CARRIER TRANSPORT: DISENTANGLING THE IMPACTS OF EFFECTIVE MASS AND SCATTERING TIME THROUGH MICROSCOPIC OPTICAL DETECTION

Contributions of Authors and Co-Authors

Manuscript: Perovskite Carrier Transport: Disentangling the Impacts of Effective Mass and Scattering Time Through Microscopic Optical Detection

Author: Andrew H. Hill

Contributions: Synthesized and characterized all $MAPbI_3$ samples. Collected all $MAPbI_3$ ultrafast microscopic data. Performed fitting of $MAPbI_3$ and $CsPbBrI_2$ images. Assisted in writing and editing manuscript.

Author: Casey L. Kennedy

Contributions: Synthesized all $CsPbBrI_2$ samples. Collected all $CsPbBrI_2$ ultrafast microscopic data. Aided in analysis of ultrafast microscopic data. Provided valuable feedback on early drafts of manuscript.

Author: Eric S. Massaro

Contributions: Aided in analysis of ultrafast microscopic data. Provided valuable feedback on early drafts of manuscript.

Author: Erik M. Grumstrup

Contributions: Assisted with analysis and editing of manuscript for final submission.

Manuscript Information Page

Andrew H. Hill, Casey L. Kennedy, Eric S. Massaro, Erik M. Grumstrup
Journal of Physical Chemistry Letters

Status of Manuscript:
____ Prepared for submission to a peer-reviewed journal
____ Officially submitted to a peer-review journal
____ Accepted by a peer-reviewed journal
_X_ Published in a peer-reviewed journal

Published by the American Chemical Society
Submitted March 1, 2018
Accepted May 11, 2018
Volume 9, Issue 11, 2808 - 2813

CHAPTER FOUR

PEROVSKITE CARRIER TRANSPORT: DISENTANGLING THE IMPACTS OF EFFECTIVE MASS AND SCATTERING TIME THROUGH MICROSCOPIC OPTICAL DETECTION

4.1 Introduction

The work presented in Chapter 3 identified the primary contributors to carrier transport in $MAPbI_3$ to be a high static dielectric constant and strong carrier-phonon coupling. While the high diffusivities reported in Chapter 3 suggest $MAPbI_3$ may be positioned to supplant silicon as the active media in cost-effective solar cells, problems remain in the literature concerning the stability of $MAPbI_3$ based devices,[98] potentially limiting their viability as a long-term alternative to Silicon based photovoltaics. To date, the majority of research efforts have focused on hybrid organic-inorganic perovskites (HOIP, A = $CH_3NH_3^+$, $CN_2H_5^+$), however, all-inorganic analogues utilizing a cesium cation have recently emerged as more chemically stable alternatives to OMHPs.[98-99] These pure inorganic analogues are promising from the perspective of improved stability, but exhibit reduced average (electron and hole) mobilities relative to the hybrid systems,[53-54, 100] a factor which may underpin the reduced power conversion efficiencies observed in all-inorganic perovskite solar cells.[101-102]

To understand why the two materials exhibit different mobilities, it is instructive to consider what material parameters influence carrier transport. Carrier mobility (or, via the Einstein relation, the diffusion constant) of a material is determined by the ratio of two more fundamental material parameters: the carrier effective mass ($m_{e/h}$) and mean

scattering time (τ), $\mu_{e/h} = q\tau/m_{e/h}$.[55] Therefore, a comparison of materials based solely on their respective mobilities inherently overlooks a more fundamental argument regarding *why* carriers in one material are transported faster than those in another. The carrier mass and mean scattering time reflect different properties of the material. Carrier effective mass is determined by the dispersion of both the valence and conduction bands[41] as well as the extent to which the lattice distorts around photogenerated carriers.[103] The scattering time reflects the average frequency carriers experience a scattering event that alters their momentum state.[41] Thus, the ability to disentangle and directly compare these two parameters can provide a deeper understanding of the photophysics of materials systems and, ultimately, a clearer avenue toward their optimization for various applications.

In this Chapter, we outline and apply a microscopy-based approach to optically determine both the optical mass [$(1/m_e + 1/m_h)^{-1}$] and the average scattering time of photogenerated carriers in individual micron-scale domains of $MAPbI_3$, and in the highest photoconversion efficiency all-inorganic perovskite $CsPbBrI_2$.[101-102] While other spectroscopies (terahertz, magneto-absorption, cyclotron resonance) can elucidate these parameters, they often rely on complimentary theoretical studies or limited-availability instrumentation (*e.g.* high field magnets). Of more relevance to thin film materials, these techniques probe sample volumes on the hundreds of micron to millimeter length scales, requiring samples to be single crystalline over similar length scales or risk conflating intrinsic material properties with the effects of morphological or compositional heterogeneities. In contrast, the high spatial resolution enabled by optical microscopy

allows selective interrogation of highly crystalline perovskite domains, minimizing (or in principle, isolating and characterizing) the effects of band bending and carrier scattering that can occur at grain boundaries and other structural heterogeneities. Our measurements on individual $MAPbI_3$ and $CsPbBrI_2$ domains show that charge carriers in the two materials have similar reduced optical masses (0.10 +/- 0.01 m_0 and 0.12 +/- 0.01 m_0, respectively), but that the average carrier scattering times differ substantially between $MAPbI_3$ (τ = 5.1 fs) and $CsPbBrI_2$ (τ = 1.7 fs). These results reveal that the reduced mobility of $CsPbBrI_2$ relative to $MAPbI_3$ is due largely to its shorter mean carrier scattering time, an effect likely caused by increased lattice disorder from the mixed-halide stoichiometry of $CsPbBrI_2$.

4.2 Results and Discussion

The optical response of individual $MAPbI_3$ and $CsPbBrI_2$ domains are interrogated using a home-built ultrafast microscope. Two laser pulses (pump and probe) with a controlled temporal delay are coupled into a microscope objective (100x, 0.9 NA), which focuses both to near diffraction-limited spots and collects the retroreflected probe light for detection. The pump pulse serves to excite charge carriers across the bandgap, and the accompanying change in sample reflectivity is monitored by the probe pulse. The small exciton binding energies in $MAPbI_3$ and $CsPbBrI_2$ (12 meV[104] and 10 meV[54], respectively) imply that excitons play little role in the excited state dynamics. Photoexcitation of direct band-gap semiconductors results in a myriad of many-body effects which perturb the optical response of the material. In the lead halide perovskites, band-gap renormalization,[49] band-filling,[17] line broadening,[105] and stimulated emission all contribute to the band edge

optical response. These many competing optical effects make spectroscopic interpretation challenging, particularly for techniques that probe the imaginary part of the dielectric function at the band edge. To circumvent these issues, we instead probe the change in reflectivity (the real part of the dielectric function) below the band gap energy, which to a good approximation, depends linearly on the photogenerated charge carrier density.

Figure 4.1 outlines the ground-state optical response of two individual perovskite domains, each of which is characterized by a distinct fringe pattern reflecting its morphology. Figure 1A shows an atomic force micrograph (AFM) of a single $MAPbI_3$ domain with a corresponding scanning emission micrograph (SEM) in Figure 1B. The equilibrium reflectivity image shown in Figure 1C is collected by scanning the focused probe beam (λ_{probe} = 800 nm) over the sample. The image is dominated by alternating bright and dark interference fringes, the positions of which are determined by the thickness and refractive index of the perovskite domain.

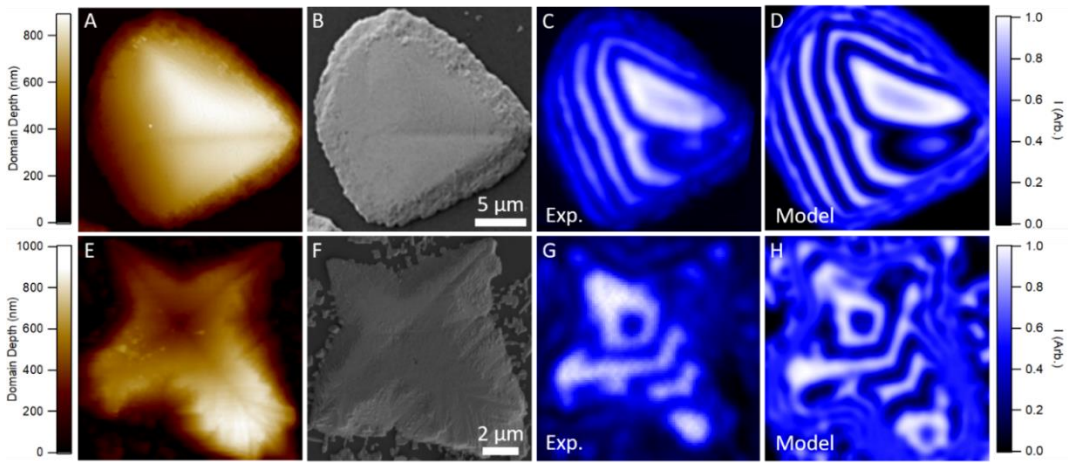

Figure 4.1. Characterization of $MAPbI_3$ and $CsPbBrI_2$ crystalline domains. (A) AFM and (B) SEM image of $MAPbI_3$ domain. (C) Reflectivity image at λ_{probe} = 800 nm of domain shown in panels A, B. (D) Modeled reflectivity image of domain with n = 2.56. (E) AFM and (F) SEM image of $CsPbBrI_2$ domain. (G) Experimental and (H) modeled (n = 2.33) reflectivity images of domain shown in panels E, F.

Using the AFM shown in Figure 4.1 A, the reflectivity image can be fit using a transfer matrix approach to extract the ground-state refractive index of 2.56 +/- 0.02.[51, 106-107] A discussion of our model and fitting routines is provided in Appendix B. The modeled image of the $MAPbI_3$ domain generated using the AFM in Figure 4.1 A and the fit-determined refractive index is shown in Figure 4.1 D. In the second row of Figure 4.1, we show analogous measurements performed on a single $CsPbBrI_2$ domain. AFM and SEM images of the domain are shown in Figure 4.1 E and Figure 4.1 F, respectively. The ground state reflectivity image of the same domain, again collected at λ_{probe} = 800 nm, is shown in panel G. Fits analogous to those carried out on the $MAPbI_3$ domain yield a ground-state index of n = 2.33 +/- 0.01, and the modeled image (Figure 4.1 H) shows good agreement with experiment.

With the equilibrium optical response well-characterized, we shift our attention to the transient response of the perovskite domains. Upon photoexcitation, semiconductors exhibit a decrease in their refractive index due to the generation of free charge carriers, an effect often analyzed with the Drude model.[43-46] This decrease in the refractive index is given by Equation 1.1. It is reproduced below to aid readability:[41]

$$\Delta n = -\frac{Ne^2\tau^2}{2m^* n_0 \varepsilon_0 (1+\omega^2\tau^2)} \qquad (4.1)$$

Here, N is the photogenerated carrier density, e is the fundamental charge, τ is the free-carrier mean scattering time, $m^* = (1/m_e + 1/m_h)^{-1}$, is the reduced optical mass of the photogenerated carriers, n_0 is the ground state refractive index, ε_0 is the permittivity of vacuum, and ω is the probe pulse angular frequency.

A photoinduced decrease in the refractive index will have two effects on the optical response of a sample: (1) the overall reflectivity of the sample will decrease, and (2) interference fringes like those observed in Figure 4.1 will shift toward thicker regions of the domain. This effect is shown in Figure 4.2, where we calculate the reflectivity of a triangular domain (shown in black) assuming refractive indices that differ by 3% (red and blue traces). In Figure 4.2, we show the modeled pump-probe signal, which measures the difference between the pump-induced and equilibrium reflectivity, $\Delta R = [I'(x) - I(x)]$. To first order, the magnitude of the oscillations in the ΔR image are proportional to the change in the refractive index. Therefore, because the refractive index change is a function of both m^* and τ (see Equation 4.1), the transient reflectivity images are sensitive probes of these fundamental material properties.

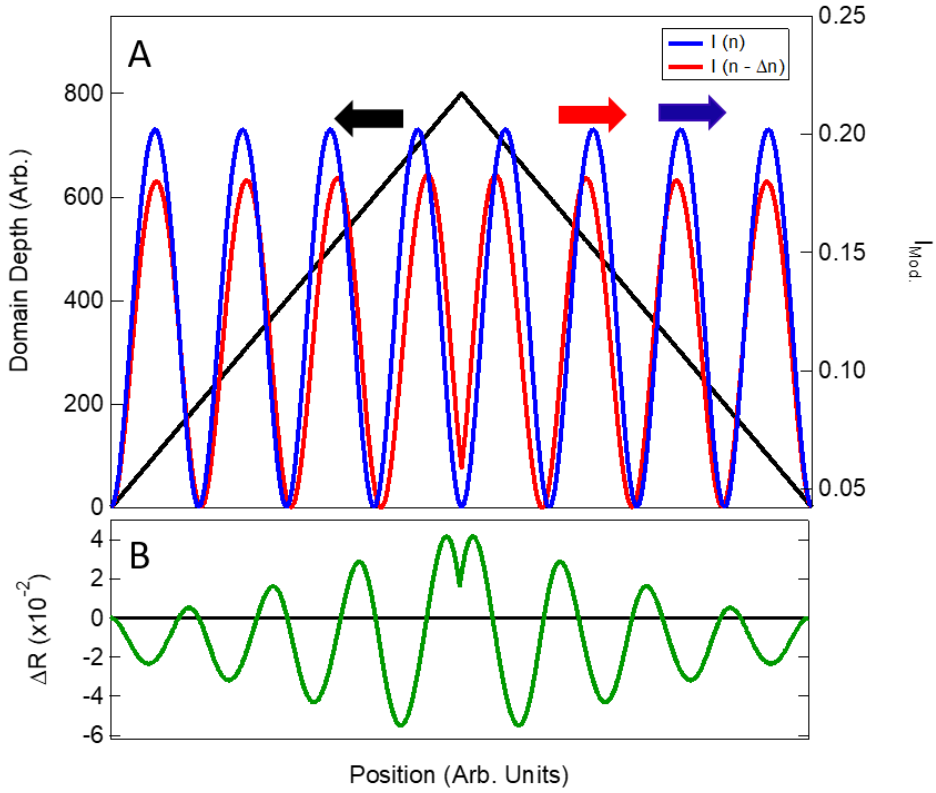

Figure 4.2. Effects of a refractive index change in pump-probe reflection imaging. (A) Profile of hypothetical domain (black line) overlaid with two predicted reflectivity traces assuming different refractive indices. A decrease in the refractive index (red vs. blue traces) is accompanied by lateral shifts of the interference fringes. Also note the mean decrease in amplitude between the blue and red traces. (B) Predicted pump-probe signal, $[I(n-\Delta n)-I(n)]$, determined from the two traces shown in panel A.

In Figure 4.3, we show the excited state response of the same $MAPbI_3$ domain displayed in the top row of Figure 1. The experimental transient reflectivity image in panel A is collected at a pump-probe delay of Δt = 2 ps, when the transient reflectivity signal is maximal (SI), using a 600 nm excitation pulse with a fluence of 13.1 μJ cm^{-2}. At this excitation energy and density, the carriers have cooled to the band edge by 2 ps.[74] While fringe magnitudes in the experimental ΔR image (~ 10^{-4}) are much smaller than those in

the modeled data of Figure 4.2 (~ 10^{-2}), the qualitative agreement suggests that a pump-induced decrease in the refractive index dominates the photoresponse of $MAPbI_3$.

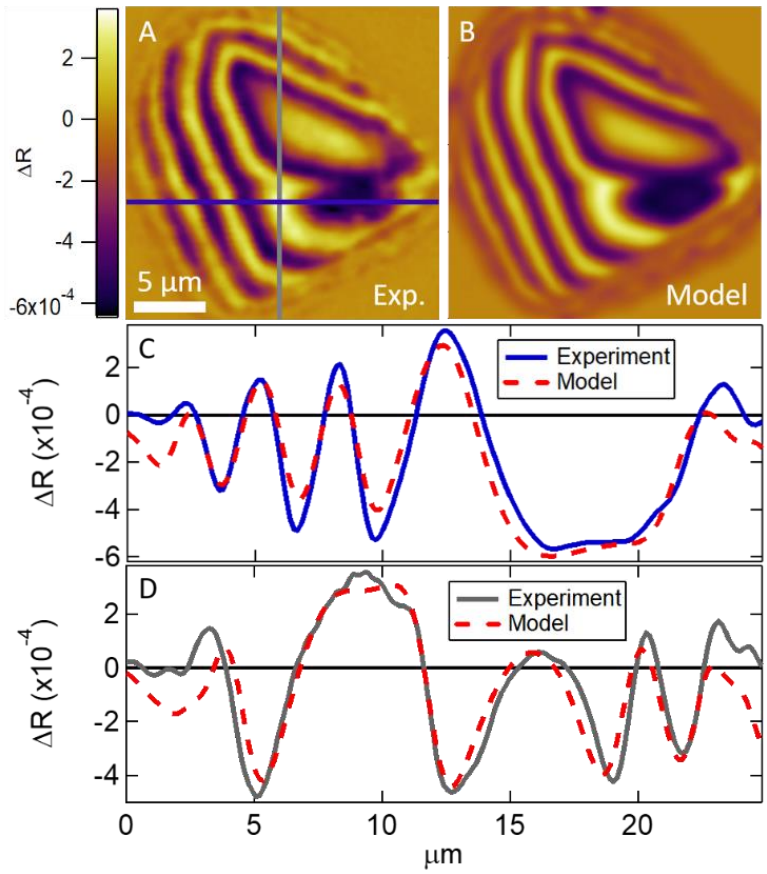

Figure 4.3. Analysis of single domain $MAPbI_3$ transient reflectivity image. (A) Pump-probe image of the $MAPbI_3$ domain shown in Figure 1. (B) Modeled pump-probe image generated by fitting a Drude model to the image in panel A. (C) and (D) show single slice comparisons of experimental (blue and grey solid lines) and modeled (red dashed) ΔR images. Location of profiles indicated in panel A by the corresponding blue and grey solid lines.

To determine m^* and τ from the ΔR image, it is necessary to first address two complicating factors. The first is that for optically thick systems like the perovskite domains in Figures 4.1 and 4.3, photoexcitation generates an exponentially varying charge carrier density determined by the wavelength dependent absorption coefficient, α_λ. To

address this, we employ a numerical transfer matrix approach which explicitly accounts for the depth-dependent carrier density (full details in Appendix B). The second complicating factor is that the Drude response given by Equation 4.1 is a function of both the optical mass, m^*, and the mean scattering time, τ. It is therefore necessary to make a second measurement to allow for simultaneous determination of the two parameters. To provide this correlation, we measure the material diffusivity by directly imaging carrier motion using spatially-separated pump-probe microscopy.[53-54]

$$D_{am} = \frac{\tau kT}{m_{av}} \qquad (4.2)$$

Here, kT is the thermal energy. Like the Drude response, the ambipolar diffusion constant is a function of the mean scattering time, τ. However, Equation 1 depends on the reduced optical mass while D_{am} (Equation 4.2) is a function of the average mass of the electron and hole, m_{av}. Therefore, to solve the two expressions simultaneously, we make use of the approximation (to first order) $m^* \approx 1/2\, m_{av}$, which, due to the similar hole and electron effective masses in lead halide perovskites, introduces little error.[108] We note that benchmark measurements performed on an intrinsic (100) silicon wafer recover a scattering time and optical mass which are both consistent with reported values, despite silicon's relatively disparate electron and hole effective masses (see Appendix B for details).

We highlight at this point that the correlation of ambipolar diffusivity with the refractive index change is predicated on the fact that the masses, m^*, probed in the two measurements (Equations 4.1 & 4.2) are the same. While this assumption certainly holds for most inorganic semiconductors (e.g. silicon, GaAs), it may be less clear for the lead

halide perovskites, where polarons are thought to form from the coupling of electronic and nuclear degrees of freedom.[108-110] One way to approach this question is by considering the thermal velocity of the carriers in the lattice. If we assume the (electron or hole) polaron mass is 0.3 m_e,[108] the polaron velocity[111] ($v_{th} = \sqrt{2kT/m^*}$) in $MAPbI_3$ is $\sim 2 \times 10^7$ cm s^{-1}. At this velocity, the unit cell transit time is ~5 fs, corresponding to a characteristic thermal frequency (v_{th}/a) of ~ 200 THz, which far exceeds the LO phonon mode frequency (and is comparable to the optical probe frequency). This characteristic transport frequency suggests that the strong coupling limit in which the electron adiabatically follows the nuclear motion is not appropriate for $MAPbI_3$ (at least at room temperatures). Rather, it is more appropriate to consider the weak coupling limit, in which the polaron behaves much like a free carrier, with a slightly modified mass, $m_p \approx m_{e/h}(1 + \alpha/6)$, where α is the Fröhlich coupling parameter.[111] Assuming α ~ 1.7[112] we estimate the maximum error introduced by equating the optical masses in the two measurements is ~ 25%. As we discuss in detail later, we suspect this is an overestimation of the error, given the low temperature assumptions implicit in the Fröhlich model.

Given the above assumptions, the ΔR images can be analyzed to independently determine τ and m^*. To do so, the Drude response (Equation 4.1) is recast in terms of τ and the experimentally-determined D_{am}. The resultant expression is then used in conjunction with a depth-dependent carrier density and the AFM image to calculate equilibrium and photoinduced reflectivities at each position on the perovskite domain. The calculated difference image is fit to the experimental ΔR image using a standard least squares

algorithm. Figure 4.3B shows the fit of the $MAPbI_3$ domain using an ambipolar diffusivity of D_{am} = 1.2 cm^2s^{-1}, an average value taken across 25 domains previously reported in Ref. 54. The modeled image is generated using the best fit parameters of τ = 5.1 +/- 0.1 fs and $m^*_{.}$ = 0.10 +/- 0.01 m_0 (where m_0 is the electron rest mass). The reported errors are derived from uncertainties in the measured excitation density propagated through the fitting procedure, however the value of τ should be interpreted as an ensemble average, as its value is determined from the average distribution of diffusion constants (see Appendix B). Note that in this long scattering time limit, the Drude response is insensitive to the scattering time of the carriers (see Equation 4.1 for $\omega^2\tau^2 \gg 1$), and thus the scattering time is determined exclusively from the diffusion measurement. Single slice comparisons of the modeled and experimental ΔR images, taken at the positions indicated in panel A, are shown in Figures 4.3 C and 4.3 D. The model captures both the positions and amplitudes of the experimental interference fringes exceptionally well. While there are some discrepancies, they tend to occur near the edges where the domain surface is rough (see Figure 4.1 B), suggesting that roughness effects not included in our model are the primary cause[107] of the disagreement between the modeled and experimental values.

The average scattering time we find for $MAPbI_3$ (5.1 fs) is closely comparable to that obtained from THz spectroscopy[113] (4.2 fs). The minor discrepancy likely reflects differences in the spatial resolution of the two techniques. THz measurements of polycrystalline films inevitably sample grain boundaries and structural defects that function as efficient scattering sites for photogenerated carriers,[82, 108] contributing to the shorter observed scattering times. In the case of ultrafast microscopy, the influence of grain

boundaries on the measured values is eliminated by the ability to probe photogenerated carrier populations exclusively in structurally homogenous regions. The optical mass we determine for $MAPbI_3$ (0.10 +/- 0.01 m_0) is also in good agreement with reported values, which range from 0.10 - 0.15 m_0.[49, 88, 114-115]

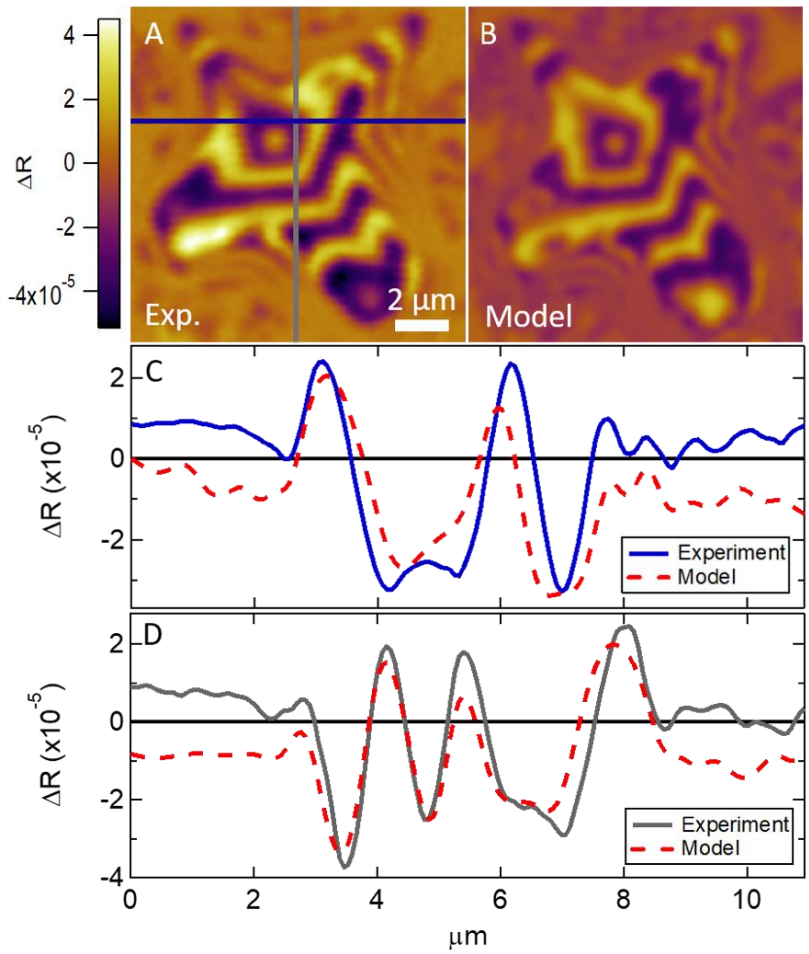

Figure 4.4. Pump-probe image modeling of the $CsPbBrI_2$ perovskite domain. (A) Experimental pump-probe reflectivity image. (B) Modeled image generated from a Drude model fit to the experimental pump-probe image in panel A. (C) and (D) show single-slice comparisons of experimental (blue and grey solid lines) and modeled (red, dashed lines) ΔR images. Profile locations are indicated by the corresponding blue and grey solid lines in panel A.

Figure 4.4 presents a corresponding analysis of the $CsPbBrI_2$ domain shown in Figure 4.1 E-H. In Panel A, the pump-probe image collected at $\Delta t = 4$ ps (at maximal $\Delta R/R$, SI) for an excitation pulse energy of 2.8 μJ cm^{-2} is shown (λ_{pump} = 550 nm). As in the $MAPbI_3$ case, the change in reflectivity, calculated using the equilibrium and pump-modified transfer matrices, was fit to the experimental image. The good agreement between the modeled image (panel B) and the experimental image is consistent with a pump-induced shift in the Fabry-Perot mode positions. Using a diffusivity[54] averaged from 14 domains (see SI) of $D_{am.}$ = 0.31 $cm^2\ s^{-1}$ we determine a mean carrier scattering time of τ = 1.7 +/- 0.1 fs and an optical mass of 0.12 +/- 0.01 m_0 for $CsPbBrI_2$. In this case, the long scattering time limit of the Drude response is not met, in contrast to $MAPbI_3$. Single-slice comparisons between modeled and experimental data are shown in Figure 4.4 C and 4.4 D. Again, the amplitude and the position of the transient fringes are well-described by our model, with small deviations likely arising from local variations in the finesse of the perovskite domain due to surface roughness. Comparison with the literature shows that the optical mass determined here is closely comparable to that obtained from high-field magneto-absorption measurements (0.124 m_0).[116]

The analysis described above highlights a number of important comparisons between the two perovskite systems. First, our results show the optical masses in $MAPbI_3$ and $CsPbBrI_2$ are similar. If polaron formation were strongly coupled to the reorientation of the A-site cation, we would expect to see a significant reduction in the diffusion constant in $MAPbI_3$ relative to $CsPbBrI_2$ according to Equation 4.2. In fact, we find the opposite case, suggesting that the polaronic character of the two perovskites is similar and likely a

consequence of more conventional models of polar lattice distortion.[103] This interpretation is in agreement with recent results suggesting that charge carriers predominantly couple with phonon modes of the lead-halide octahedra.[109] We attribute the slight increase in optical mass of $CsPbBrI_2$ relative to $MAPbI_3$ to the partial Br substitution, where more strongly localized band edge carriers (greater band edge dispersion) are a reflection of the higher ionization potential of Br relative to I. Analogous effects can be observed in ZnSe and ZnTe, where the isoelectronic substitution of Te with Se is correlated to a significant increase in carrier mass.[117]

Second, we note that while the slightly larger optical mass accounts for ~20% of the observed decrease in carrier mobility in $CsPbBrI_2$ relative to $MAPbI_3$, the most important factor is the threefold shorter mean scattering time (τ = 1.7 fs vs. τ = 5.1 fs, respectively). The shorter scattering time of $CsPbBrI_2$ likely reflects a disruption of long-range energetic ordering of the band structure introduced by substitution of iodine with the smaller and more electronegative bromine. Indeed, the calculated mean free path for $CsPbBrI_2$ ($\lambda_m = \tau\sqrt{3kT/m^*} = 5.7$ Å) is significantly shorter than the length of a unit cell (~10 Å)[54] whereas in $MAPbI_3$, the mean free path of the carriers ($\lambda_m = 18.8$ Å) spans nearly two unit cells. While further studies correlating halide and cation substitution to carrier scattering times are needed, these results suggest that efforts aimed at optimizing performance in all-inorganic perovskite solar cells should focus on reducing lattice disorder through stabilization of bulk $CsPbI_3$, either through chemical means (doping) or via non-equilibrium fabrication approaches.[118]

Finally, we note the scattering times we recover from these experiments and the characteristic frequencies of the carriers we interrogate raise important questions regarding the sensitivity of our technique (and, by extension, the Drude response at optical frequencies) to the large polaron formation believed to play a role in the lead-halide perovskite photoresponse.[109, 119] As previously discussed, our correlation of the two approaches implicitly assumes that the carrier mass relevant to the thermal diffusion measurement is in fact the same carrier mass that determines the (high frequency) optical response. This comparison appears problematic at first, given the optical frequencies used in the Drude measurements far exceed the ability of the nuclear motions to "keep up" with the electronic response. However, this picture is likely relevant only at temperatures below the Debye temperature (kT < $\hbar\omega_{ph}$), where traditional polaron theory is strictly relevant (and where cyclotron resonance, a robust probe of polaron effective mass, has been traditionally performed). Using calculated values of the Fröhlich coupling parameter α ~ 1.7,[112] and an average phonon energy, $\hbar\omega_{ph}$ ~ 12 meV, the polaron self-energy (in the weak coupling limit) $E_0 \approx -\alpha\hbar\omega_{ph} = -20\ meV$, is smaller than kT at room temperature (25.7 meV). Thus, in this simple picture, the charge carriers (at least in the primarily iodide perovskites) would appear to have sufficient average thermal energy available to escape the self-trapped polaron state and behave largely like strongly scattering free carriers. While such an argument depends on the scattering mechanism of polarons with lattice phonons, (which is known to be modified[111]) it may provide insight into why we measure (at optical frequencies) nearly the same carrier scattering times in $MAPbI_3$ as THz measurements,[113] which should be more sensitive to low-frequency nuclear motions.

Additional experimental probes of carrier transport, perhaps in chemically modified systems and at varying temperatures, are needed to understand these effects. However, we note that the challenges associated with disentangling a polaron effective mass from phonon scattering, particularly as temperatures approach $\hbar\omega_{ph}/k$, have been recognized for some time.[120-121] Further complicating an understanding of carrier transport in the lead halide perovskites is the broad and distinctly anharmonic phonon spectrum which spans 0 – 200 cm^{-1},[122-123] as well as the fact that, due to structural phase transitions, the high symmetry phases of lead halide perovskites cannot be studied at temperatures low enough to freeze out the low-frequency lattice modes of the material.

4.3 Conclusions

In conclusion, we have determined the optical mass and mean scattering time of charge carriers in $CsPbBrI_2$ and $MAPbI_3$. The comparison was enabled through determination of the free carrier contribution to the refractive index, coupled with direct measurements of the ambipolar diffusivity. Our analysis yields photogenerated carrier effective masses of 0.11 +/- 0.01 m_0 and 0.13 +/- 0.01 m_0, and carrier scattering times of τ = 5.9 +/- 0.1 fs and τ = 1.7 +/- 0.1 fs for $MAPbI_3$ and $CsPbBrI_2$, respectively. These results highlight significant differences in carrier transport between the two materials, and suggest routes toward optimized carrier transport in all-inorganic lead-halide perovskites.

REFERENCES CITED

(17) Manser, J. S.; Kamat, P. V. Band Filling with Free Charge Carriers in Organometal Halide Perovskites. *Nat. Photonics* **2014,** *8*, 737-743.

(41) Elliot, R. J.; Gibson, A. F. *An Introduction to Solid State Physics and Its Applications*. The Macmillan Press Ltd.: United Kingdom, 1974.

(43) Sabbah, A. J.; Riffe, D. M. Measurement of Silicon Surface Recombination Velocity Using Ultrafast Pump–Probe Reflectivity in the near Infrared. *J. Appl. Phys.* **2000,** *88*, 6954-6956.

(44) Sabbah, A. J.; Riffe, D. M. Femtosecond Pump-Probe Reflectivity Study of Silicon Carrier Dynamics. *Phys. Rev. B* **2002,** *66*, 165217.

(45) Bennett, B. R.; Soref, R. A.; Alamo, J. A. D. Carrier-Induced Change in Refractive Index of InP, GaAs and InGaAsP. *IEEE J. Quantum Electron.* **1990,** *26*, 113-122.

(46) Henry, C. H.; Logan, R. A.; Bertness, K. A. Spectral Dependence of the Change in Refractive Index Due to Carrier Injection in GaAs Lasers. *J. Appl. Phys.* **1981,** *52*, 4457-4461.

(49) Price, M. B.; Butkus, J.; Jellicoe, T. C.; Sadhanala, A.; Briane, A.; Halpert, J. E.; Broch, K.; Hodgkiss, J. M.; Friend, R. H.; Deschler, F. Hot-Carrier Cooling and Photoinduced Refractive Index Changes in Organic-Inorganic Lead Halide Perovskites. *Nat. Commun.* **2015,** *6*, 8420.

(51) Born, M.; Wolf, E. *Principles of Optics*. Pergamon Press: London, 1959.

(53) Hill, A. H.; Smyser, K. E.; Kennedy, C. L.; Massaro, E. S.; Grumstrup, E. M. Screened Charge Carrier Transport in Methylammonium Lead Iodide Perovskite Thin Films. *J. Phys. Chem. Lett.* **2017,** *8*, 948-953.

(54) Kennedy, C. L.; Hill, A. H.; Massaro, E. S.; Grumstrup, E. M. Ultrafast Excited-State Transport and Decay Dynamics in Cesium Lead Mixed Halide Perovskites. *ACS Energy Lett.* **2017,** *2*, 1501-1506.

(55) Sze, S. M. *Physics of Semiconductor Devices*. 3rd ed.; Wiley: New York, 2006.

(74) Fu, J.; Xu, Q.; Han, G.; Wu, B.; Huan, C. H. A.; Leek, M. L.; Sum, T. C. Hot Carrier Cooling Mechanisms in Halide Perovskites. *Nat. Commun.* **2017,** *8*, 1300.

(82) Reid, O. G.; Yang, M.; Kopidakis, N.; Zhu, K.; Rumbles, G. Grain-Size-Limited Mobility in Methylammonium Lead Iodide Perovskite Thin Films. *ACS Energy Lett.* **2016,** *1*, 561-565.

(88) Chen, Y.; Yi, H. T.; Wu, X.; Haroldson, R.; Gartstein, Y. N.; Rodionov, Y. I.; Tikhonov, K. S.; Zakhidov, A.; Zhu, X. Y.; Podzorov, V. Extended Carrier Lifetimes and Diffusion in Hybrid Perovskites Revealed by Hall Effect and Photoconductivity Measurements. *Nat. Commun.* **2016,** *7*, 12253.

(98) Beal, R. E.; Slotcavage, D. J.; Leijtens, T.; Bowring, A. R.; Belisle, R. A.; Nguyen, W. H.; Burkhard, G. F.; Hoke, E. T.; McGehee, M. D. Cesium Lead Halide Perovskites with Improved Stability for Tandem Solar Cells. *J. Phys. Chem. Lett.* **2016,** *7*, 746-51.

(99) Akbulatov, A. F.; Luchkin, S. Y.; Frolova, L. A.; Dremova, N. N.; Gerasimov, K. L.; Zhidkov, I. S.; Anokhin, D. V.; Kurmaev, E. Z.; Stevenson, K. J.; Troshin, P. A. Probing the Intrinsic Thermal and Photochemical Stability of Hybrid and Inorganic Lead Halide Perovskites. *J. Phys. Chem. Lett.* **2017,** *8*, 1211-1218.

(100) Dastidar, S.; Li, S.; Smolin, S. Y.; Baxter, J. B.; Fafarman, A. T. Slow Electron–Hole Recombination in Lead Iodide Perovskites Does Not Require a Molecular Dipole. *ACS Energy Lett.* **2017,** *2*, 2239-2244.

(101) Niezgoda, J. S.; Foley, B. J.; Chen, A. Z.; Choi, J. J. Improved Charge Collection in Highly Efficient $CsPbBrI_2$ Solar Cells with Light-Induced Dealloying. *ACS Energy Lett.* **2017,** *2*, 1043-1049.

(102) Nam, J. K.; Chai, S. U.; Cha, W.; Choi, Y. J.; Kim, W.; Jung, M. S.; Kwon, J.; Kim, D.; Park, J. H. Potassium Incorporation for Enhanced Performance and Stability of Fully Inorganic Cesium Lead Halide Perovskite Solar Cells. *Nano Lett.* **2017,** *17*, 2028-2033.

(103) Frohlich, H. Introduction to the Theory of the Polaron. In *Polarons and Excitons*, Kuper, C. G.; Whitfield, G. D., Eds. Plenium Press: New York, 1962; pp 1-22.

(104) Galkowski, K.; Mitioglu, A.; Miyata, A.; Plochocka, P.; Portugall, O.; Eperon, G. E.; Wang, J. T.-W.; Stergiopoulos, T.; Stranks, S. D.; Snaith, H. J.; et al. Determination of the Exciton Binding Energy and Effective Masses for Methylammonium and Formamidinium Lead Tri-Halide Perovskite Semiconductors. *Energy Environ. Sci.* **2016,** *9*, 962-970.

(105) Sharma, V.; Aharon, S.; Gdor, I.; Yang, C.; Etgar, L.; Ruhman, S. New Insights into Exciton Binding and Relaxation from High Time Resolution Ultrafast Spectroscopy of $CH_3NH_3PbI_3$ and $CH_3NH_3PbBr_3$ Films. *J. Mater. Chem. A* **2016,** *4*, 3546-3553.

(106) Katsidis, C. C.; Siapkas, D. I. General Transfer-Matrix Method for Optical Multilayer Systems with Coherent, Partially Coherent, and Incoherent Interference. *Appl. Opt.* **2002,** *41*, 3978-3987.

(107) Mitsas, C. L.; Siapkas, D. I. Generalized Matrix Method for Analysis of Coherent and Incoherent Reflectance and Transmittance of Multilayer Structures with Rough Surfaces, Interfaces, and Finite Substrates. *Appl. Opt.* **1995,** *34*, 1678-1683.

(108) Herz, L. M. Charge-Carrier Mobilities in Metal Halide Perovskites: Fundamental Mechanisms and Limits. *ACS Energy Lett.* **2017,** *2*, 1539-1548.

(109) Miyata, K.; Meggiolaro, D.; Trinh, M. T.; Joshi, P. P.; Mosconi, E.; Jones, S. C.; De Angelis, F.; Zhu, X.-Y. Large Polarons in Lead Halide Perovskites. *Sci. Adv.* **2017,** *3*.

(110) Frost, J. M. Calculating Polaron Mobility in Halide Perovskites. *Phys. Rev. B* **2017,** *96*, 195202.

(111) Emin, D. Optical Properties of Large and Small Polarons and Bipolarons. *Phys. Rev. B* **1993,** *48*, 13691-13702.

(112) Sendner, M.; Nayak, P. K.; Egger, D. A.; Beck, S.; Muller, C.; Epding, B.; Kowalsky, W.; Kronik, L.; Snaith, H. J.; Pucci, A.; et al. Optical Phonons in Methylammonium Lead Halide Perovskites and Implications for Charge Transport. *Mater. Horizons* **2016,** *3*, 613-620.

(113) Karakus, M.; Jensen, S. A.; D'Angelo, F.; Turchinovich, D.; Bonn, M.; Cánovas, E. Phonon–Electron Scattering Limits Free Charge Mobility in Methylammonium Lead Iodide Perovskites. *J. Phys. Chem. Lett.* **2015,** *6*, 4991-4996.

(114) Miyata, A.; Mitioglu, A.; Plochocka, P.; Portugall, O.; Wang, J. T.-W.; Stranks, S. D.; Snaith, H. J.; Nicholas, R. J. Direct Measurement of the Exciton Binding Energy and Effective Masses for Charge Carriers in Organic-Inorganic Tri-Halide Perovskites. *Nat. Phys.* **2015,** *11*, 582-587.

(115) Tanaka, K.; Takahashi, T.; Ban, T.; Kondo, T.; Uchida, K.; Miura, N. Comparative Study on the Excitons in Lead-Halide-Based Perovskite-Type Crystals $CH_3NH_3PbBr_3$ $CH_3NH_3PbI_3$. *Solid State Commun.* **2003,** *127*, 619-623.

(116) Yang, Z.; Surrente, A.; Galkowski, K.; Miyata, A.; Portugall, O.; Sutton, R. J.; Haghighirad, A. A.; Snaith, H. J.; Maude, D. K.; Plochocka, P.; et al. Impact of the Halide Cage on the Electronic Properties of Fully Inorganic Cesium Lead Halide Perovskites. *ACS Energy Lett.* **2017,** *2*, 1621-1627.

(117) Madelung, O. *Semiconductors: Data Handbook.* 3rd ed.; Springer - Verlag Berlin Heidelberg: 2004.

(118) Fu, Y.; Rea, M. T.; Chen, J.; Morrow, D. J.; Hautzinger, M. P.; Zhao, Y.; Pan, D.; Manger, L. H.; Wright, J. C.; Goldsmith, R. H.; et al. Selective Stabilization and Photophysical Properties of Metastable Perovskite Polymorphs of $CsPbI_3$ in Thin Films. *Chem. Mater.* **2017,** *29*, 8385-8394.

(119) Neukirch, A. J.; Nie, W.; Blancon, J.-C.; Appavoo, K.; Tsai, H.; Sfeir, M. Y.; Katan, C.; Pedesseau, L.; Even, J.; Crochet, J. J.; et al. Polaron Stabilization by Cooperative Lattice Distortion and Cation Rotations in Hybrid Perovskite Materials. *Nano Lett.* **2016,** *16*, 3809-3816.

(120) Smilga, A. V. On the Polaron Mass at Finite Temperatures. *J. Phys. Condens. Matter* **1991,** *3*, 915.

(121) Ahrenkiel, R. K. Studies of the Polaron Mobility in Agbr at High Temperatures. *Phys. Rev.* **1969,** *180*, 859-863.

(122) Bonn, M.; Miyata, K.; Hendry, E.; Zhu, X. Y. Role of Dielectric Drag in Polaron Mobility in Lead Halide Perovskites. *ACS Energy Lett.* **2017,** *2*, 2555-2562.

(123) Egger, D. A.; Bera, A.; Cahen, D.; Hodes, G.; Kirchartz, T.; Kronik, L.; Lovrincic, R.; Rappe, A. M.; Reichman, D. R.; Yaffe, O. What Remains Unexplained About the Properties of Halide Perovskites? *Adv. Mater.* **2018**, 1800691.

CHAPTER FIVE

DETERMINING THE EFFECTS OF A-SITE CATION SUBSTITUTION ON THE OPTICAL RESPONSE AND TRANSPORT PROPERTIES OF LEAD TRI-BROMIDE PEROVSKITES

Contributions of Authors and Co-Authors

Manuscript: Determining the Effects of A-Site Cation Substitution on the Optical Response and Transport Properties of Lead Tri-Bromide Perovskites

Author: Andrew H. Hill

Contributions: Synthesized and characterized all $MAPbBr_3$ and $FAPbBr_3$ samples. Characterization included Uv-Vis Absorption, X-Ray Diffraction, and emission measurements. Collected all $MAPbBr_3$ and $FAPbBr_3$ ultrafast microscopic data. Performed fitting of all $MAPbBr_3$ and $FAPbBr_3$ images. Assisted in writing and editing manuscript.

Author: Casey L. Kennedy

Contributions: Synthesized and characterized all $CsPbBr_3$ samples. Collected all $CsPbBr_3$ ultrafast microscopic data. Performed fitting of all $CsPbBr_3$ images. Provided valuable feedback on early drafts of manuscript.

Author: Erik M. Grumstrup

Contributions: Aided in analysis of ultrafast microscopic data. Provided valuable feedback on early drafts of manuscript.

Manuscript Information Page

Andrew H. Hill, Casey L. Kennedy, Erik M. Grumstrup
Journal of Physical Chemistry Letters

Status of Manuscript:
__X_ Prepared for submission to a peer-reviewed journal
____ Officially submitted to a peer-review journal
____ Accepted by a peer-reviewed journal

CHAPTER FIVE

DETERMINING THE EFFECTS OF A-SITE CATION SUBSTITUTION ON THE OPTICAL RESPONSE AND TRANSPORT PROPERTIES OF LEAD TRI-BROMIDE PEROVSKITES

5.1 Introduction

Chapter 4 detailed the development of a microscopy-based technique capable of uniquely determining the optical mass and mean scattering time of photogenerated carriers in micron-sized crystalline domains. This technique was then applied to two different perovskites ($MAPbI_3$ and $CsPbBrI_2$) to recover a nearly fourfold decrease in the scattering time of carriers in $CsPbBrI_2$ relative to $MAPbI_3$. We also reported a slight increase in the optical mass of carriers in $CsPbBrI_2$ and ascribed that increase to partial Br_I substitution.[124]

Chapter 4 also contained discussions of the potential role of polarons in determining the photophysics and carrier transport in lead-halide perovskite systems. While the concept that extensive coupling of electronic and nuclear degrees of freedom plays a large role in perovskite photoresponse is gaining acceptance within the perovskite photophysics community[108] there is still a debate regarding the mechanisms which dominate polaron formation. One interpretation suggests that the organic cations in OMHPs may reorient their dipole moment in the response to passing charge carriers to provide high dielectric shielding to inhibit interactions between charge carriers and other charged species.[125] Another claims that charge carriers couple primarily to bending and breathing vibrational modes of the lead-halide octahedra at the core of the perovskite unit cell.[109]

Unfortunately, due to the nature of the two materials studied in Chapter 4 that work is unable to speak conclusively on this issue. $MAPbI_3$ and $CsPbBrI_2$ have neither the same A-site cation nor the same halide profile so we are unable to conclusively ascribe the increase in photogenerated carrier masses to the effect of either. In fact, an in-depth understanding of the roles that each building-block of the perovskite lattice plays on carrier transport is lacking within the literature. On a general level, changing the A-site cation is known to have tangible consequences on the optoelectronic properties of the material. All-inorganic perovskites display lower diffusivities[54, 108] and go on to produce lower efficiency photovoltaic devices than their hybrid organic-inorganic counterparts.[101-102] However, these conclusions must be drawn from multiple studies. Many research groups prepare their samples using different methods and interrogate them using a wide variety of (often bulk) spectroscopies with varying dependencies on sample morphology and grain boundary density.[82, 108] This results in a literature with little agreement between studies regarding benchmark optoelectronic properties (carrier lifetime, carrier diffusion length, etc) of nominally identical materials, as highlighted by Herz.[108] With little agreement on the properties of similar materials, looking to two separate studies of two different materials to answer more fundamental questions regarding the role each substituent plays in carrier transport becomes challenging.

To characterize the role the cation plays in determining the photophysics of lead halide perovskites, we have synthesized and characterized the structural and optical properties of a series of three lead tri-bromide ($APbBr_3$) perovskites each employing a different A-site cation; a methylammonium (MA) cation, a formamidinium (FA) cation,

and a Cesium (Cs) ion. By keeping the same halide profile across the entire series but changing the identity of the A-site cation we are able to make explicit determinations of the role the A-site cation plays in carrier transport in hopes of informing future debate regarding the dominant mechanisms of polaron formation in these materials.

Thin-films samples of each perovskite were prepared using identical one-step spin coating protocols. In order to minimize the effects of sample morphology and grain-boundary density on observed carrier diffusion, transport measurements were made using ultrafast microscopy. Across a number of highly-crystalline domains we find $MAPbBr_3$ and $FAPbBr_3$ to have almost identical average diffusivities ($D_{av.}$ = 1.50 cm^2s^{-1} and $D_{av.}$ = 1.43 cm^2s^{-1} respectively) while $CsPbBr_3$ displays substantially slower average carrier diffusion ($D_{av.}$ = 0.91 cm^2s^{-1}). Interestingly we find $MAPbBr_3$ and $FAPbBr_3$ to be almost spectroscopically indistinguishable with nearly identical bandgaps, carrier lifetimes, and carrier diffusion constants. Application of the technique discussed in Chapter 4 reveals all three species to have photogenerated carrier optical masses that are identical within our error. These findings support the theory that the optical properties of lead halide perovskites are determined largely by the lead-halide cage and that the A-site cation serves only to stabilize the crystal structure.

5.2 Experimental Methods: Sample Preparation and Steady-State Characterization

Thin-film samples of $MAPbBr_3$, $FAPbBr_3$, and $CsPbBr_3$ were synthesized according to previously published protocols.[54] In contrast to the synthesis of $MAPbI_3$ in Chapters 3 and 4, tri-bromide samples were all processed using a one-step spin-coating

procedure and a single precursor solution. 0.25 - 1 M solutions of $PbBr_2$ and FA/MA/CsBr in either dimethylformamide (DMF) or, in the case of CsBr, dimethylsulfoxide (DMSO) were prepared. 250 μL of the precursor solution was spin-coated onto a glass microscope slide and then annealed in a DMF atmosphere for 1 hr at 100 ºC. Adjustments to the precursor solution solvent choice and concentration were made to optimize the quality of the resulting crystallites.

Figure 1 displays X-Ray diffractograms collected from each of the three perovskite samples. $MAPbBr_3$ and $FAPbBr_3$ are both found to adopt a cubic crystal structure, evident from the prominent contributions of the (100), (200), and (122) peaks in each. $MAPbBr_3$ displays a lattice parameter of 5.9188 Å. We determine $FAPbBr_3$ to have a lattice parameter of 5.9785 Å, representing ~1% increase in unit cell volume relative to $MAPbBr_3$, in line with previous reports.[126] In contrast, $CsPbBr_3$ adopts an orthorhombic crystal structure with lattice parameters of a = 8.272 Å, b = 11.716 Å, and c = 8.212 Å.

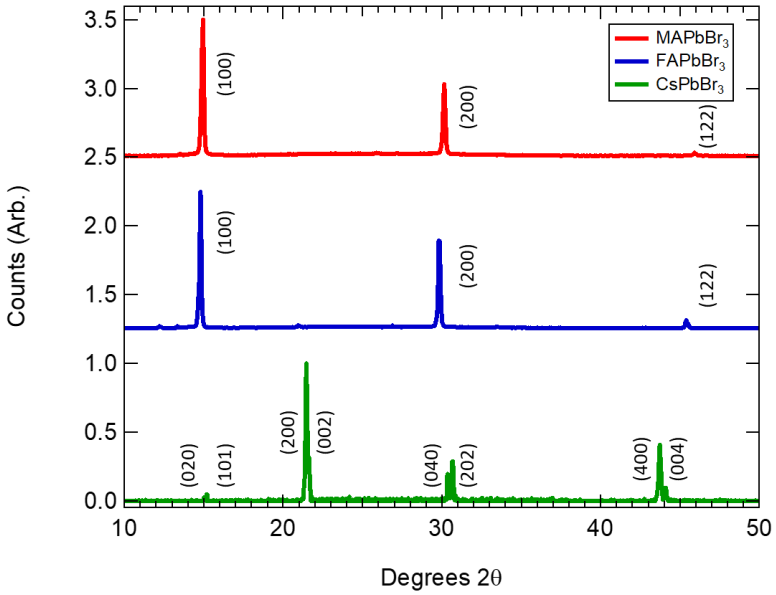

Figure 5.1. X-Ray diffractograms of $MAPbBr_3$ (red), $FAPbBr_3$ (blue), and $CsPbBr_3$ (green) perovskite samples.

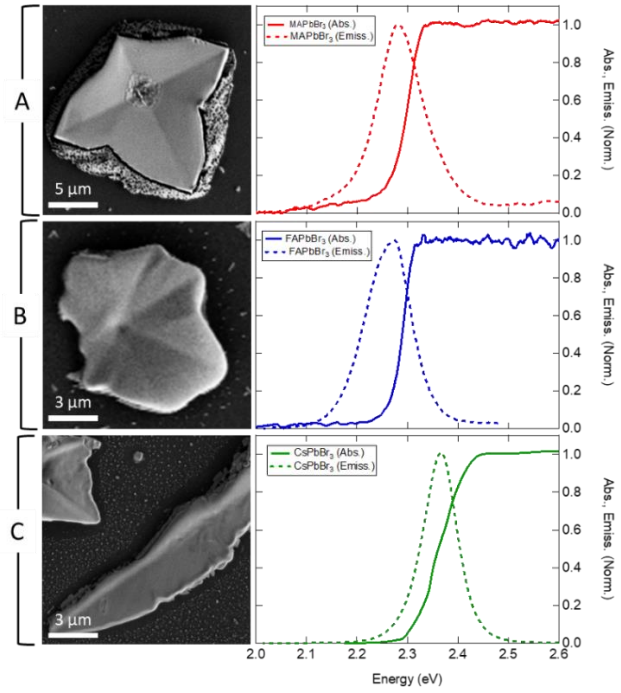

Figure 5.2. Characterization of lead tri-bromide perovskite sample series. (A) Scanning electron microscopy image of individual crystallite (left) and accompanying absorption / emission spectra (right) of $MAPbBr_3$. (B) Scanning electron microscopy image of individual crystallite (left) and accompanying absorption / emission spectra (right) of $FAPbBr_3$. (C) Scanning electron microscopy image of individual crystallite (left) and accompanying absorption / emission spectra (right) of $CsPbBr_3$.

Figure 5.2 shows scanning electron microscopy (SEM) images of individual $MAPbBr_3$, $FAPbBr_3$, and $CsPbBr_3$ crystallites along with accompanying absorption and emission spectra. Absorption spectra were collected from a UV-Vis microscope and emission spectra were collected from a commercial fluorimeter. The bandgaps we find for $MAPbBr_3$, $FAPbBr_3$, and $CsPbBr_3$ (2.30 eV, 2.30 eV, and 2.37 eV, respectively) are all in agreement with previously reported values for single crystalline samples of each species.[127-129]

5.3 Excited State Characterization: Recombination and Transport Properties

Figure 5.3 A – C show spatially overlapped pump-probe images of $MAPbBr_3$, $FAPbBr_3$, and $CsPbBr_3$ crystallites collected 2 ps after photoexcitation. All images were collected using a 400 nm pump pulse followed by an 800 nm probe pulse. The pump pulse fluence used to generate each image varies from species to species, but care was taken to ensure that the images were collected at fluences in which the magnitude of the transient signal was linear with respect to pump pulse fluence. The observed oscillations in signal intensity are due to the same Fabry-Perot interference phenomena discussed in Chapter 4. Figure 5.3 D shows kinetics decay traces for each sample in the lead tri-bromide series. Interestingly the decay kinetics of lead tri-bromide perovskites appear to be relatively insensitive to the identity of the A-site cation. A double exponential (shown in color-coordinated solid lines) fits all three traces well.[130] Each sample shows a ~60% decay in the magnitude of the transient signal at 250 ps indicating similar recombination dynamics, though early-time decay appears to be more pronounced in $CsPbBr_3$ compared

to $FAPbBr_3$ and $MAPbBr_3$. The faster recombination displayed in $CsPbBr_3$ relative to the two hybrid organic-inorganic systems is consistent with previous reports of faster recombination processes in perovskites with an orthorhombic crystalline geometry.[54]

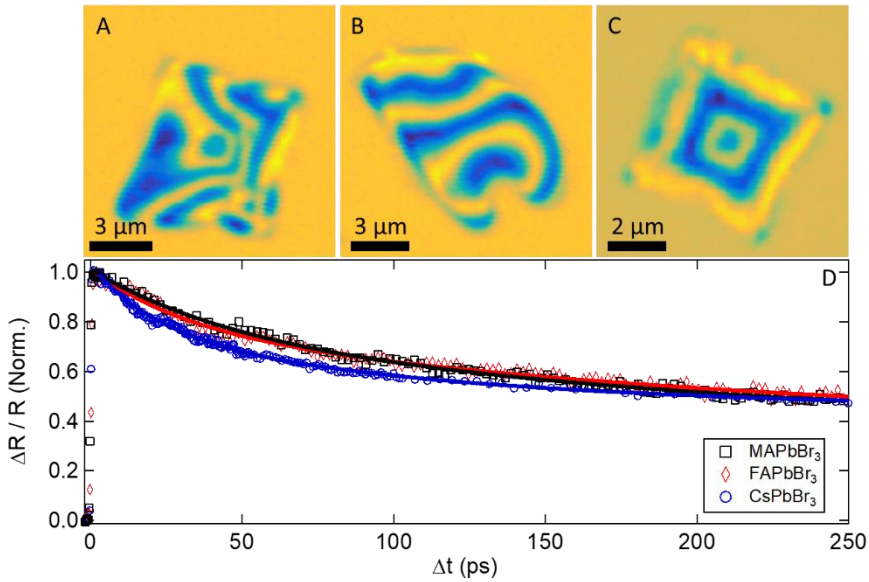

Figure 5.3. Characterization of photoexcited lead tri-bromide perovskites. (A) Spatially overlapped pump-probe image of $MAPbBr_3$ crystallite. (B) Spatially overlapped pump-probe image of $FAPbBr_3$ crystallite. (C) Spatially overlapped image of $CsPbBr_3$ perovskite. (D) Comparison of decay kinetics of $MAPbBr_3$ (black squares), $FAPbBr_3$ (red diamonds), and $CsPbBr_3$ (blue circles). Data shown with double exponential fits in color corresponding solid lines.

Carrier transport in perovskite domains is measured by monitoring the spatial evolution of the charge carrier cloud generated by the pump pulse. Charge carriers diffuse under a concentration gradient and are imaged by the time-delayed probe pulse whose position on the sample is controlled by a set of galvanometer mirrors. Figure 5.4 A shows a spatially overlapped image of an $MAPbBr_3$ domain. After the spatially overlapped image is collected, a region showing a homogeneous transient response is selected and a series of images of the photogenerated carrier cloud are taken at increasing time delays.

The carrier distributions captured in these images are then fit to a Gaussian profile, the full-width-at-half-maximum (fwhm) of which broadens with respect to time reflecting carrier transport. Data shown in Figure 5.4 B, collected from the domain shown in Figure 5.4 A, displays time-dependent broadening of the photogenerated carrier cloud attributed to carrier diffusion.[28, 53-54] Figure 5.4 C shows a histogram of diffusion constants collected in this manner from 13 $MAPbBr_3$ crystallites yielding an average ambipolar diffusivity of $D_{av.} = 1.50\ cm^2s^{-1}$. Figures 5.4 D – 5.4 F and 5.4 G – 5.4 I show analogous data collected from $FAPbBr_3$ and $CsPbBr_3$ crystallites. From eight samples of $FAPbBr_3$ we determine an average diffusivity of $D_{av.} = 1.43\ cm^2s^{-1}$, and from 12 $CsPbBr_3$ crystallites we find $D_{av.} = 0.91\ cm^2s^{-1}$.

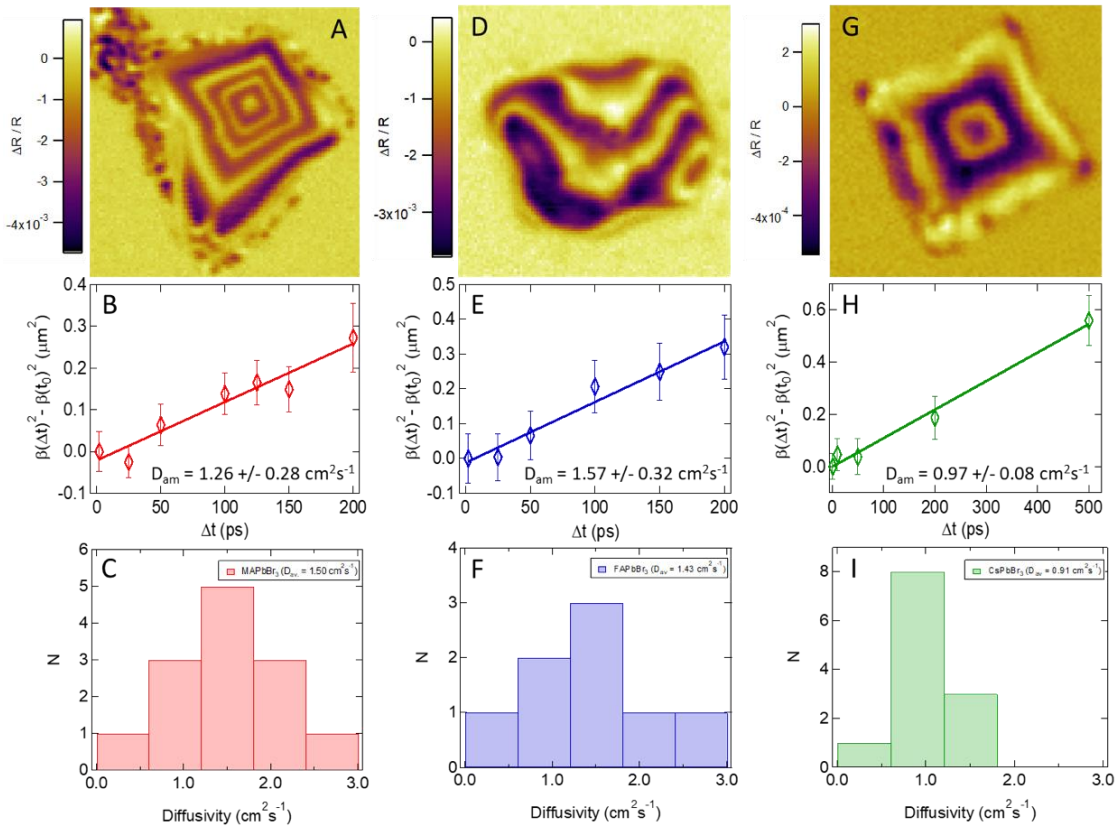

Figure 5.4. Characterization of charge carrier mobilities in MA/FA/$CsPbBrI_3$ perovskite crystallites. (A) Spatially overlapped image of $MAPbBr_3$ perovskite crystallite. (B) Time-dependent broadening of photogenerated carrier distribution collected from spot marked in panel A. (C) Histogram of charge carrier diffusivities collected from 13 $MAPbBr_3$ samples. (D) Spatially overlapped image of $FAPbBr_3$ perovskite crystallite. (E) Time-dependent broadening of photogenerated carrier distribution collected from spot marked in panel D. (F) Histogram of charge carrier diffusivities collected from 8 $FAPbBr_3$ samples. (G) Spatially overlapped image of $CsPbBr_3$ perovskite crystallite. (H) Time-dependent broadening of photogenerated carrier distribution collected from spot marked in panel G. (I) Histogram of charge carrier diffusivities collected from 12 $CsPbBr_3$ samples.

In the case of the organic A-site cations (MA and FA) we determine no meaningful effects of the A-site cation on the perovskite's equilibrium optical properties. Absorption spectra shown in Figure 1 determine a bandgap of 2.29 eV for both $MAPbBr_3$ and $FAPbBr_3$. The Stokes shift seen in each material is similar as well, with $MAPbBr_3$ and $FAPbBr_3$ displaying shifts of 16 meV and 25 meV, respectively, suggesting the

samples to be of similar optical quality.[42] In light of this characterization of the quality of the $MAPbBr_3$ and $FAPbBr_3$ crystallites, similarities between the recombination and transport dynamics in the two materials become somewhat expected. Decay kinetics of each shown in Figure 5.2 D almost perfectly overlay one another, and the two materials show remarkably similar average diffusivities as displayed in Figure 5.3.

The remarkable optical similarity we observe between $MAPbBr_3$ and $FAPbBr_3$ in both the ground and excited state is not entirely unexpected. Multiple theoretical studies performed on hybrid organic-inorganic perovskites predicts the frontier orbitals (those largely responsible for the perovskite optical response) to be comprised entirely of the lead cation and halide cage,[131-133] suggesting that the orbitals of the A-site cation play no appreciable role in carrier absorption or transport. This leaves the A-site cation primarily to stabilize the perovskite crystal structure, only influencing the optical properties of the material through determining the degree of orbital overlap experienced between the lead and halide ions. Through this lens, extensive spectroscopic similarity between $MAPbBr_3$ and $FAPbBr_3$ makes intuitive sense. The ionic radii of the two cations[134] (2.70 Å and 2.79 Å for MA and FA, respectively) differ by less than 4% resulting in a ~1% expansion of the $FAPbBr_3$ lattice relative to $MAPbBr_3$. This minute difference in A-site cation size, and similarly negligible difference in the lattice size, seem unlikely to appreciably change the overlap of the lead and halide orbitals, in agreement with the observed similarity between the $MAPbBr_3$ and $FAPbBr_3$ we report above.

A Cesium cation, however, has an atomic radius of 1.81 Å,[134] roughly 33% smaller than either of the organic cations studied above. The optical consequences of this

A-site cation size discrepancy are readily seen when comparing the absorption spectra of $CsPbBr_3$ and either of the hybrid organic-inorganic perovskites studied. $CsPbBr_3$ presents a bandgap of 2.37 eV, noticeably blue-shifted relative to $MAPbBr_3$ and $FAPbBr_3$. The blue-shifting has been attributed to a change in the Pb-I-Pb angle which is determined largely by the crystalline structure.[135] In the case of a cubic crystal structure (such as in $MAPbBr_3$ and $FAPbBr_3$) this angle is close to 180º,[136] allowing for favorable overlap of the lead and halide orbitals which determine the density of states for both the valence and conduction bands.[137] In the case of $CsPbBr_3$, which assumes an octahedral geometry the Pb-I-Pb angle is reduced significantly to 153.2º, changing the orbital overlap and leading to a destabilization of the conduction band and an increase in the bandgap.[135]

Despite the different electronic structure, the substitution of a cesium ion for a larger organic cation seems to have a relatively minor effect on excited state decay dynamics. While decay traces of $CsPbBr_3$ show faster initial recombination than $MAPbBr_3$ or $FAPbBr_3$ all three materials studied show a half-life of around 200 ps. Based on a survey of multiple SEMs of each species, we note that crystallites of the $CsPbBr_3$ perovskites appear significantly more amorphous than those of $MAPbBr_3$ and $FAPbBr_3$, which may be indicative of slightly reduced crystalline quality. A lower quality crystal will have a higher density of defect sites for carriers to recombine, which is in qualitative agreement with the slightly accelerated decay we report above. $CsPbBr_3$ crystals being of lower crystalline quality would also explain the reduced carrier diffusion seen in $CsPbBr_3$ ($D_{av.}$ = 0.91 cm^2s^{-1}) relative to $MAPbBr_3$ ($D_{av.}$ = 1.50 cm^2s^{-1}) and $FAPbBr_3$ ($D_{av.}$ = 1.43 cm^2s^{-1}). Carriers diffusing in a material with a higher defect density

will on average have a shorter scattering time than those diffusing in a highly crystalline material.

Puzzlingly, the Stokes shift seen in $CsPbBr_3$ is the smallest of the three materials (~5 mEv) which suggests it to be more highly crystalline than our samples of $MAPbBr_3$ and $FAPbBr_3$.[138] While this is an interesting result we stress that the emission spectra displayed in Figure 5.1 were collected on an instrument that lacks the spatial resolution of those used to collect the absorption spectra and perform the excited state characterization discussed above. Bulk spectroscopies are more susceptible to the influence of grain boundaries and edge states than spatially resolved spectroscopies, leading to complications when attempting to compare the optical properties of these materials.[108] As such, we place more credence in the data collected through spatially resolved spectroscopies. Based on a survey of SEM images of each species we believe the $MAPbBr_3$ and $FAPBr_3$ samples studied to be of higher crystalline quality than the $CsPbBr_3$ samples. The increased crystalline quality of the $MAPbBr_3$ and $FAPbBr_3$ allows photogenerated carriers to diffuse more rapidly in these materials, likely through an increase in their average carrier scattering times relative to $CsPbBr_3$.

Although we attribute the reduced diffusivity seen in $CsPbBr_3$ relative to $MAPbBr_3$ and $FAPbBr_3$ to a decrease in the relative quality of the crystallites, if our emission data is to be believed this may not be the case. Recent research suggests that polaron formation may play a role, with the coupling constant for electron and hole polaron formation in $CsPbBr_3$ predicted to be nearly twice that seen in $MAPbBr_3$.[109] This would result in carriers in $CsPbBr_3$ having significantly higher optical masses than those

in $MAPbBr_3$ and $FAPbBr_3$, which would cause the observed decrease in carrier diffusivity. The contributions of the average carrier scattering time and the carrier optical mass to diffusion can be disentangled though application of the analysis method described in Chapter 4. Conducting the same experiments on $MAPbBr_3$, $FAPbBr_3$, and $CsPbBr_3$ would allow us to determine the cause of the abated diffusion seen in $CsPbBr_3$ relative to the two OMHP species, as well as answer lingering questions in the literature regarding the role of the A-site cation in carrier transport.

5.4 Quantifying the effect of Cation Substitution on Photogenerated Carrier Optical Mass and Mean Scattering Time

In an effort to determine the effects of cation substitution on photgenerated carrier optical mass and mean scattering time we performed the image analysis routine outlined in Chapter 4 on $MAPbBr_3$, $FAPbBr_3$, and $CsPbBr_3$ perovskites. Figure 5.5 summarizes the application of our technique to an $MAPbBr_3$ domain. Panel A shows an experimental pump-probe image of the domain. Our fitting routines return a ground state refractive index of $n_0 = 2.07$, a mean carrier scattering time of $\tau = 8.0$ fs, and a photogenerated carrier optical mass of $m^* = 0.18 +/- 0.04\ m_0$. A modeled image reproduced using these values is shown in Panel B. Single slice comparisons of the experimental and modeled images are shown in Panels C and D. As was the case for the domains presented in Chapter 4, our model captures both the intensities and positions of the interference fringes exceptionally well. The most substantial deviations from the model are found at the edges of the domain and likely caused by surface roughness effects not accounted for in our model.

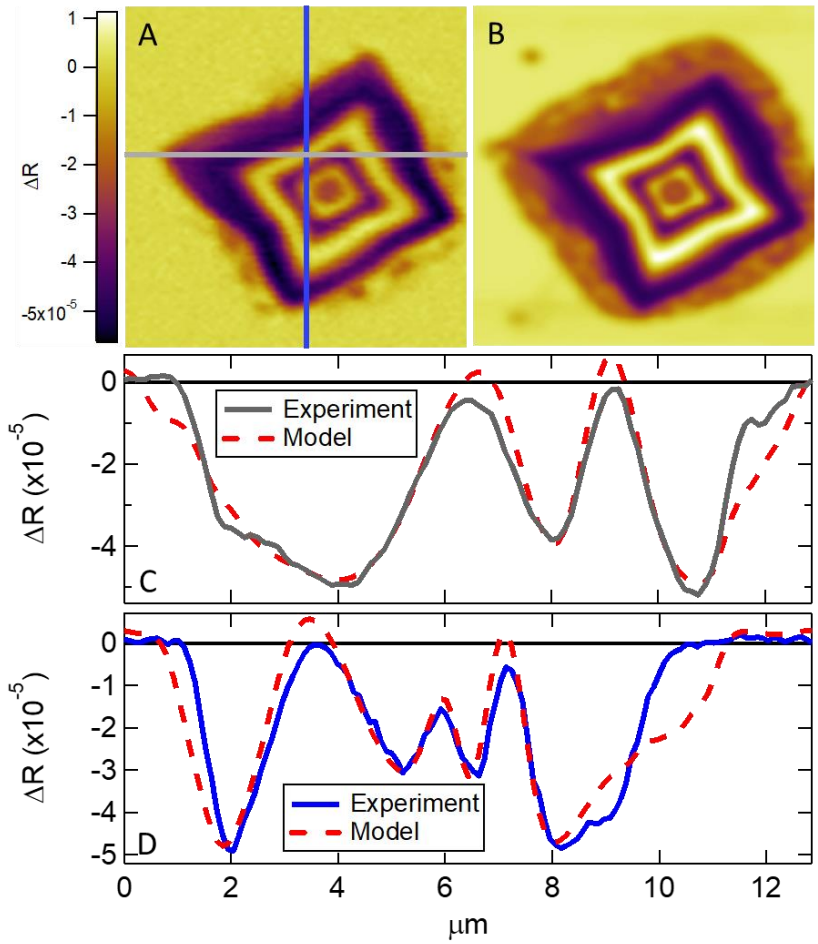

Figure 5.5. Pump-probe image analysis of $MAPbBr_3$ domain. (A) Experimental pump-probe image of $MAPbBr_3$ crystallite. (B) Modeled image of $MAPbBr_3$ domain produced using fit-determined values for carrier mean scattering time, optical mass, and ground-state refractive index. (C,D) Single slice comparisons of experimental and modeled images.

Application of our image analysis routines to an $FAPbBr_3$ domain is shown in Figure 5.6. An experimental pump-probe image is shown in Panel A and accompanied by a modeled image of the same domain in Panel B produced using fit-determined values (n_0 = 1.97, τ = 21.9 fs, and m^* = 0.17 +/- 0.04 m_0). Panels C and D show horizontal and vertical slice comparisons of the experimental and modeled images. As in Figure 5.5 our model captures the experimental data exceptionally well. Discrepancies between the

modeled and experimental values are, however, quite noticeable at the edges of the domain owed to the roughness of the crystallite.

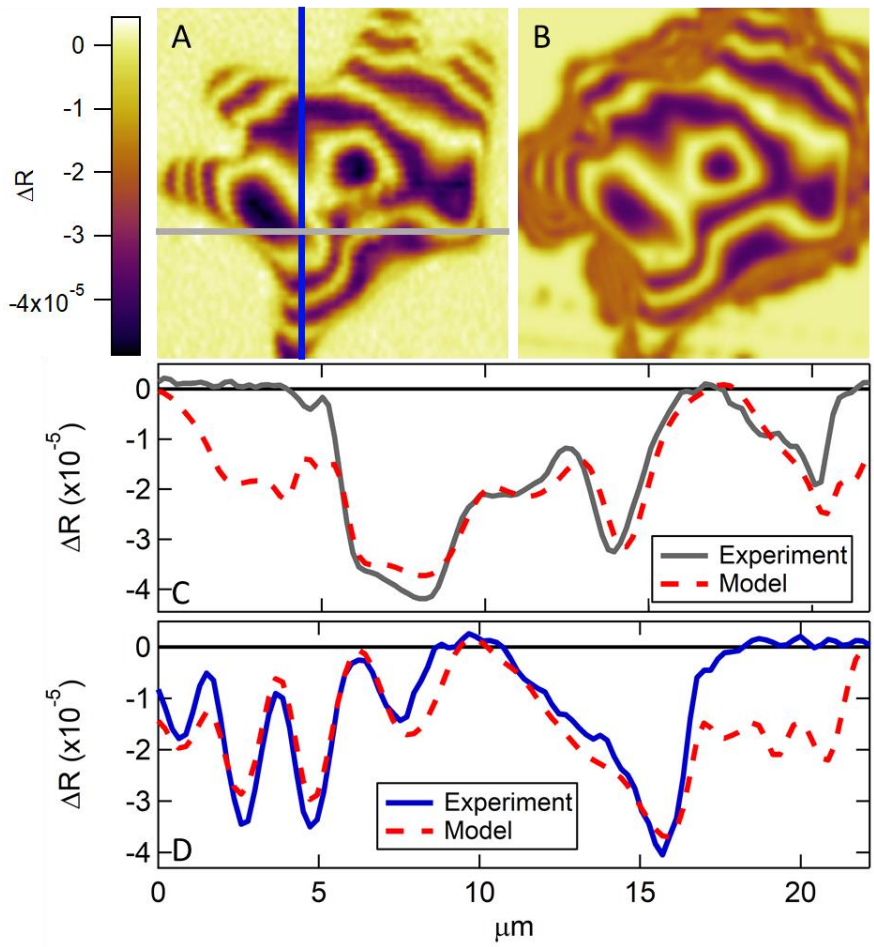

Figure 5.6. Pump-probe image analysis of $FAPbBr_3$ domain. (A) Experimental pump-probe image of $FAPbBr_3$ crystallite. (B) Modeled image of $FAPbBr_3$ domain produced using fit-determined values for carrier mean scattering time, optical mass, and ground-state refractive index. (C,D) Single slice comparisons of experimental and modeled images.

Lastly, we analyzed images of a $CsPbBr_3$ domain. Panel A of Figure 5.7 shows a pump-probe image of a single $CsPbBr_3$ crystallite. Our analysis returned a ground state refractive index of $n_0 = 2.37$, a mean carrier scattering time of $\tau = 4.1$ fs, and a

photogenerated carrier optical mass of $m^* = 0.14 +/- 0.04\ m_0$. A modeled image of this domain reproduced with these values is shown in Panel B. Single-slice comparisons of the experimental and modeled images are shown in Panels C and D.

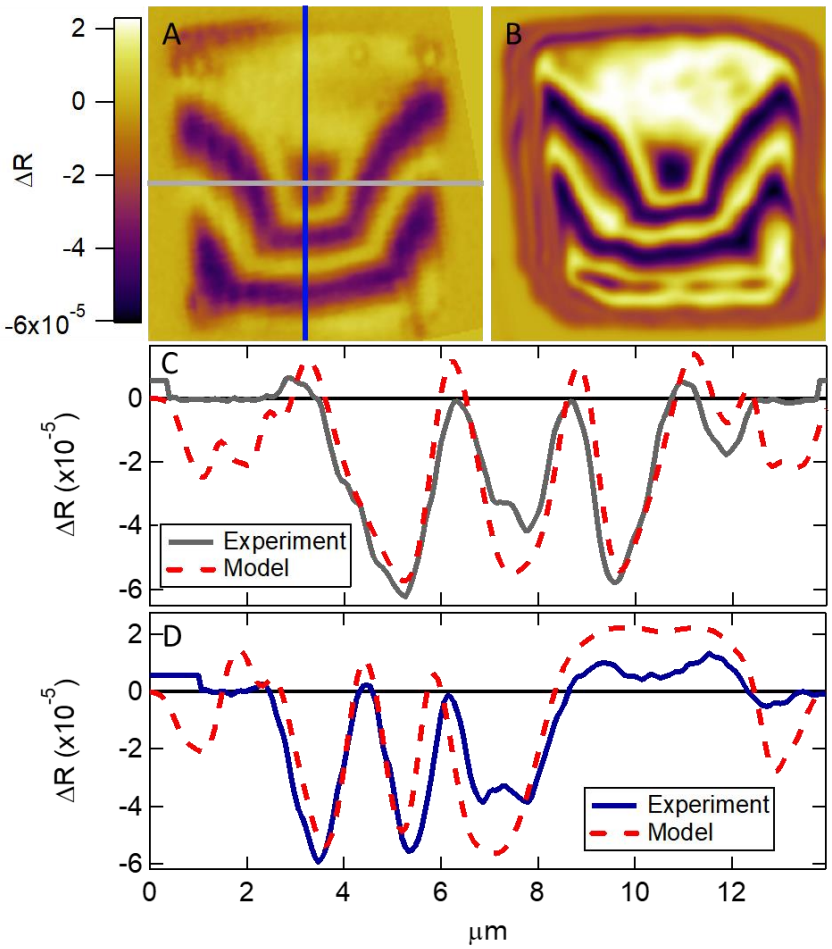

Figure 5.7. Pump-probe image analysis of $CsPbBr_3$ domain. (A) Experimental pump-probe image of $FAPbBr_3$ crystallite. (B) Modeled image of $FAPbBr_3$ domain produced using fit-determined values for carrier mean scattering time, optical mass, and ground-state refractive index. (C,D) Single slice comparisons of experimental and modeled images.

Interestingly all three species ($MAPbBr_3$, $FAPbBr_3$, and $CsPbBr_3$) show remarkably similar material properties. This similarity is most apparent when considering

the optical masses of photogenerated carriers in each material which our method measures to be identical within error. At first glance, the long scattering time of the $FAPbBr_3$ domain (21.9 fs vs 8.0 and 4.1 fs) appears to be an outlier, but the difference can be explained by consideration of the ambipolar diffusivity of each domain analyzed. Both the $MAPbBr_3$ and $CsPbBr_3$ domains showed similarly modest diffusivities (1.0 cm^2s^{-1} and 0.64 cm^2s^{-1}, respectively), while a rather high diffusivity was measured on the $FAPbBr_3$ domain (2.94 cm^2s^{-1}) shown in Fig 5.6. Because of the disparity in the diffusivities measured on each crystalline domain we believe considerations of the *average* tau, calculated using the average diffusivity of each species in lieu of the diffusivity measured on each individual domain. This approach is robust provided the photogenerated carrier optical mass is relatively invariant between crystallites of the same species (i.e. analysis of multiple grains of $MA/FA/CsPbBr_3$ return the same optical mass). Analysis of the scattering time and effective mass from multiple domains confirms this to be the case. As such, we report average scattering times of 12.0 fs, 11.4 fs, and 5.5 fs for $MAPbBr_3$, $FAPbBr_3$, and $CsPbBr_3$, respectively. A table of the recovered ground state refractive indices, average carrier scattering times, and photogenerated carrier optical masses is given in Figure 5.8.

Species	n_0	τ_{av}	m^* (m_e)
$MAPbBr_3$	2.07	12.0 fs	0.18 +/- 0.04
$FAPbBr_3$	1.94	11.4 fs	0.17 +/- 0.04
$CsPbBr_3$	2.37	5.5 fs	0.14 +/- 0.04

Figure 5.8. Parameters recovered from fitting of $MA/FA/CsPbBr_3$ perovskite pump-probe images.

While the optical masses of photogenerated carriers in MA/FA/$CsPbBr_3$ (0.18 0.04 m_0, 0.17 +/- 0.04 m_0, and 0.14 +/- 0.04 m_0, respectively) are found to be indistinguishable within error, across multiple samples carriers in $CsPbBr_3$ are consistently found to be ~20% lighter than those in MA/$FAPbBr_3$. While the optical mass discrepancy may appear to be a consequence of the inorganic A-site cation we note that subtle differences in effective mass may lie within the error of our measurement. Experiments are underway in our laboratory to improve our measurement techniques to decrease the error in these measurements. The reduced average scattering time of carriers in $CsPbBr_3$ relative to $MAPbBr_3$ and $FAPbBr_3$ is somewhat puzzling but tentatively attributed to the apparent reduced quality of the $CsPbBr_3$ crystallites compared to the $MAPbBr_3$ and $FAPbBr_3$ samples.

There exists a debate in the literature as to whether or not the Drude response (at optical frequencies) is sensitive to the polaron formation believed to play a large role in perovskite carrier transport. The method we employ here assumes that the scattering time measured by the Drude response is the same scattering time which determines carrier diffusivity. In the case of polaron formation there is the possibility that polarons have ample time to form around diffusing carriers. However the timescale of polaron formation is significantly longer than a single optical cycle of the probe pulse,[109] which is the determining time scale for the Drude response. As discussed in Chapter 4 the thermal energy available to carriers in lead-halide perovskites is higher than the Debye energy, suggesting that carriers have enough energy to escape the self-trapped polaron state and that polarons likely don’t play a role in carrier transport in these materials. Even in the

case that polaron formation does play a role in transport, consideration of the thermal velocity of charge carriers and the lattice parameters the halide perovskites suggests the characteristic frequency of carrier transport is in fact comparable to that of the probe pulse.

In the event that our method is not sensitive to polaron formation we may be underestimating the carrier optical mass for one, or all, of the species studied here. Since the polaron coupling strength is predicted to differ between the three species[109] insensitivity to polarons may lead to a significant underestimation of the average carrier scattering time and a mischaracterization of the cause of the abated diffusion in $CsPbBr_3$ relative to the two OMHP species. We reiterate that, based on the arguments provided in Chapter 4 and summarized above, we believe the Drude response and the ambipolar diffusivity to sample the same scattering time, strongly suggesting our method is sensitive to polaron formation. However, additional experiments (likely further comparison with THz and magneto-absorption results) are required to put this issue to rest.

5.5 Conclusion

In conclusion, we have synthesized and characterized the optical properties and photogenerated carrier dynamics of three separate lead tri-bromide perovskites: $MAPbBr_3$, $FAPbBr_3$, and $CsPbBr_3$. The $MAPbBr_3$ and $FAPbBr_3$ perovskites are found to be spectroscopically very similar, displaying nearly identical band gaps, excited state recombination kinetics, and carrier transport rates. $CsPbBr_3$ on the other hand exhibits a

band gap that is blue shifted relative to the hybrid organic-inorganic perovskites, along with faster recombination kinetics and slower average carrier diffusivities. Shifting of the band-gap in $CsPbBr_3$ is explained by differences in the atomic radii of the A-site cation. Application of the technique discussed in Chapter 4 to these materials determined carriers in $MAPbBr_3$, $FAPbBr_3$, and $CsPbBr_3$ to have identical optical masses within our experimental error while the mean scattering time of carriers was determined to vary with the local ambipolar diffusivity. Experiments are underway to determine the cause of the slower average diffusion seen in $CsPbBr_3$ relative to $MAPbBr_3$ and $FAPbBr_3$.

REFERENCES CITED

(28) Grumstrup, E. M.; Gabriel, M. M.; Pinion, C. W.; Parker, J. K.; Cahoon, J. F.; Papanikolas, J. M. Reversible Strain-Induced Electron-Hole Recombination in Silicon Nanowires Observed with Femtosecond Pump-Probe Microscopy. *Nano Lett.* **2014,** *14*, 6287-6292.

(42) Pankove, J. I. *Optical Processes in Semiconductors*. Dover Publications, Inc.: New York, 1971.

(53) Hill, A. H.; Smyser, K. E.; Kennedy, C. L.; Massaro, E. S.; Grumstrup, E. M. Screened Charge Carrier Transport in Methylammonium Lead Iodide Perovskite Thin Films. *J. Phys. Chem. Lett.* **2017,** *8*, 948-953.

(54) Kennedy, C. L.; Hill, A. H.; Massaro, E. S.; Grumstrup, E. M. Ultrafast Excited-State Transport and Decay Dynamics in Cesium Lead Mixed Halide Perovskites. *ACS Energy Lett.* **2017,** *2*, 1501-1506.

(82) Reid, O. G.; Yang, M.; Kopidakis, N.; Zhu, K.; Rumbles, G. Grain-Size-Limited Mobility in Methylammonium Lead Iodide Perovskite Thin Films. *ACS Energy Lett.* **2016,** *1*, 561-565.

(101) Niezgoda, J. S.; Foley, B. J.; Chen, A. Z.; Choi, J. J. Improved Charge Collection in Highly Efficient $CsPbBrI_2$ Solar Cells with Light-Induced Dealloying. *ACS Energy Lett.* **2017,** *2*, 1043-1049.

(102) Nam, J. K.; Chai, S. U.; Cha, W.; Choi, Y. J.; Kim, W.; Jung, M. S.; Kwon, J.; Kim, D.; Park, J. H. Potassium Incorporation for Enhanced Performance and Stability of Fully Inorganic Cesium Lead Halide Perovskite Solar Cells. *Nano Lett.* **2017,** *17*, 2028-2033.

(108) Herz, L. M. Charge-Carrier Mobilities in Metal Halide Perovskites: Fundamental Mechanisms and Limits. *ACS Energy Lett.* **2017,** *2*, 1539-1548.

(109) Miyata, K.; Meggiolaro, D.; Trinh, M. T.; Joshi, P. P.; Mosconi, E.; Jones, S. C.; De Angelis, F.; Zhu, X.-Y. Large Polarons in Lead Halide Perovskites. *Sci. Adv.* **2017,** *3*.

(124) Hill, A. H.; Kennedy, C. L.; Massaro, E. S.; Grumstrup, E. M. Perovskite Carrier Transport: Disentangling the Impacts of Effective Mass and Scattering Time through Microscopic Optical Detection. *J. Phys. Chem. Lett.* **2018**, 2808-2813.

(125) Zhu, H.; Miyata, K.; Fu, Y.; Wang, J.; Joshi, P. P.; Niesner, D.; Williams, K. W.; Jin, S.; Zhu, X. Y. Screening in Crystalline Liquids Protects Energetic Carriers in Hybrid Perovskites. *Science* **2016,** *353*, 1409-1413.

(126) Elbaz, G. A.; Straus, D. B.; Semonin, O. E.; Hull, T. D.; Paley, D. W.; Kim, P.; Owen, J. S.; Kagan, C. R.; Roy, X. Unbalanced Hole and Electron Diffusion in Lead Bromide Perovskites. *Nano Lett.* **2017,** *17*, 1727-1732.

(127) Wei, H.; Fang, Y.; Mulligan, P.; Chuirazzi, W.; Fang, H.-H.; Wang, C.; Ecker, B. R.; Gao, Y.; Loi, M. A.; Cao, L.; et al. Sensitive X-Ray Detectors Made of Methylammonium Lead Tribromide Perovskite Single Crystals. *Nat. Photonics* **2016,** *10*, 333.

(128) Brennan, M. C.; Herr, J. E.; Nguyen-Beck, T. S.; Zinna, J.; Draguta, S.; Rouvimov, S.; Parkhill, J.; Kuno, M. Origin of the Size-Dependent Stokes Shift in CsPbBr3 Perovskite Nanocrystals. *J. Am. Chem. Soc.* **2017,** *139*, 12201-12208.

(129) Wang, L.; Wang, K.; Zou, B. Pressure-Induced Structural and Optical Properties of Organometal Halide Perovskite-Based Formamidinium Lead Bromide. *J. Phys. Chem. Lett.* **2016,** *7*, 2556-2562.

(130) Stranks, S. D.; Burlakov, V. M.; Leijtens, T.; Ball, J. M.; Goriely, A.; Snaith, H. J. Recombination Kinetics in Organic-Inorganic Perovskites: Excitons, Free Charge, and Subgap States. *Phys. Rev. Appl.* **2014,** *2*, 034007.

(131) Zhao, T.; Shi, W.; Xi, J.; Wang, D.; Shuai, Z. Intrinsic and Extrinsic Charge Transport in $CH_3NH_3PbI_3$ Perovskites Predicted from First-Principles. *Sci. Rep.* **2016,** *6*, 19968.

(132) Endres, J.; Egger, D. A.; Kulbak, M.; Kerner, R. A.; Zhao, L.; Silver, S. H.; Hodes, G.; Rand, B. P.; Cahen, D.; Kronik, L.; et al. Valence and Conduction Band Densities of States of Metal Halide Perovskites: A Combined Experimental–Theoretical Study. *J. Phys. Chem. Lett.* **2016,** *7*, 2722-2729.

(133) Huang, X.; Paudel, T.; Dowben, P.; Dong, S.; Tsymbal, E. Electronic Structure and Stability of the $CH_3NH_3PbBr_3$ (001) Surface. *Phys. Rev. B* **2016,** *94*.

(134) Amat, A.; Mosconi, E.; Ronca, E.; Quarti, C.; Umari, P.; Nazeeruddin, M. K.; Grätzel, M.; De Angelis, F. Cation-Induced Band-Gap Tuning in Organohalide Perovskites: Interplay of Spin–Orbit Coupling and Octahedra Tilting. *Nano Lett.* **2014,** *14*, 3608-3616.

(135) Beimborn, J. C.; Hall, L. M. G.; Tongying, P.; Dukovic, G.; Weber, J. M. Pressure Response of Photoluminescence in Cesium Lead Iodide Perovskite Nanocrystals. *J. Phys. Chem. C* **2018,** *122*, 11024-11030.

(136) Stoumpos, C. C.; Kanatzidis, M. G. The Renaissance of Halide Perovskites and Their Evolution as Emerging Semiconductors. *Accounts of Chemical Research* **2015,** *48*, 2791-2802.

(137) Manser, J. S.; Christians, J. A.; Kamat, P. V. Intriguing Optoelectronic Properties of Metal Halide Perovskites. *Chem. Rev.* **2016,** *116*, 12956-13008.

(138) Singh, J. *Excitation Energy Transfer Processes in Condensed Matter: Theory and Applications*. Plenum Press: New York, 1994.

CHAPTER SIX

CONCLUSIONS AND FUTURE DIRECTIONS

6.1 Summary

The goal of this dissertation has been to characterize lead-halide perovskites by disentangling the fundamental material properties which determine their excited state dynamics. Chapter 2 detailed characterization of the excited state dynamics of $MAPbI_3$ using ultrafast microscopy. In this chapter we uncovered highly spatially variant recombination dynamics across a single crystallite. Additionally, we characterized a short-lived (sub-ps) photoinduced absorption feature at 800 nm to be a consequence of both bandgap renormalization and band-filling. This work highlighted the extensive heterogeneity endemic to solution processed lead halide perovskites and provided strong motivation for utilizing spatially resolved spectroscopies for characterizing their photophysical properties.

In Chapter 3 we shifted our focus solely to the transport properties of $MAPbI_3$, specifically studying how carrier diffusivity varied with respect to photogenerated carrier density. These experiments showed carrier diffusion to be invariant at carrier densities up to ~ 10^{19} carriers cm^{-3} above which it increases exponentially, characteristic of a loss of degeneracy in the excited state population. Further analysis of density-dependent diffusion data revealed a high dielectric constant to be the primary reason behind the remarkable transport properties of $MAPbI_3$. Additional information regarding the domain-to-domain heterogeneity of charge carrier diffusivity was also reported. Carrier

transport was measured on 25 separate domains and we observed a range of diffusivities from 0.77 cm^2s^{-1} – 1.74 cm^2s^{-1}.

Chapter 4 recounts our efforts to understand the physical mechanism by which diffusion in $CsPbBrI_2$ is reduced with respect to $MAPbI_3$. To accomplish this goal, we developed a new spectroscopic technique capable of uniquely determining the optical mass and mean scattering times of photogenerated carriers. We determined the cause of the reduced average diffusivity seen in $CsPbBrI_2$ is due to a nearly four-fold decrease in the mean scattering time relative to $MAPbI_3$ and that the optical masses of photogenerated carriers in the two materials were in fact quite similar. The reduced scattering time of carriers in $CsPbBrI_2$ relative to $MAPbI_3$ is likely due to increased lattice strain in the former due to its mixed halide stoichiometry.

Finally, in Chapter 5 we carried out an in-depth study of the excited state properties of three different lead tri-bromide perovskites each featuring a different A-site cation: MA, FA, and a Cs ion. $MAPbBr_3$ and $FAPbBr_3$ were found to be nearly spectroscopically identical, showing very similar bandgaps, emission spectra, recombination dynamics, and carrier transport properties. $CsPbBr_3$ showed notably slower carrier transport dynamics and slightly accelerated carrier recombination. Application of the technique developed in Chapter 4 to this series of materials determined the optical masses of the photogenerated carriers to be indistinguishable across all three materials. While this work calls into question the cation-rotation mediated polaron formation mechanism prevalent in the literature, further experiments are ongoing to

verify the results. Work is also in progress to identify the cause of the slower average diffusion seen in $CsPbBr_3$ relative to the two hybrid organic-inorganic species.

6.2 Future Work

6.2.1 Correlation of Emission Linewidth with Local Recombination Dynamics and Transport Properties

The mean scattering time of charge carriers in semiconductors can, in the low-density limit, provide valuable information about the defect density and degree of ordering of the crystalline sample. Similar information can be determined from the spectral width of the emission profile of a sample.[42] Work is currently ongoing in our laboratory to correlate local diffusion measurements with spatially resolved emission measurements on a series of perovskite crystallites. Our hypothesis is that areas of crystallites which display faster ambipolar diffusivities will exhibit narrower emission spectra than those with of slower diffusing carriers.

To determine whether or not there is a correlation between emission linewidth and carrier transport, we have constructed a fluorescence microscope capable of measuring emission spectra collected from 1.0 – 3.5 um^2 sample areas. Briefly, the excitation pulse is directed towards the back aperture of a microscope objective. Immediately before the objective we place a dichroic mirror to reflect the excitation pulse but allow any emitted light to pass through uninhibited. After the pump pulse excites the sample, emitted light is collected and collimated by the microscope objective and directed towards the galvanometer mirrors. Then the emitted light is coupled into an optical fiber which directs it towards a scanning monochromator where individual wavelengths of emitted

light are separated and sent towards a photomultiplier tube for detection. The signal from the photomultiplier tube is then analysed by a lock-in amplifier and routed to a computer for collection and analysis. This instrument is detailed in Figure 6.1.

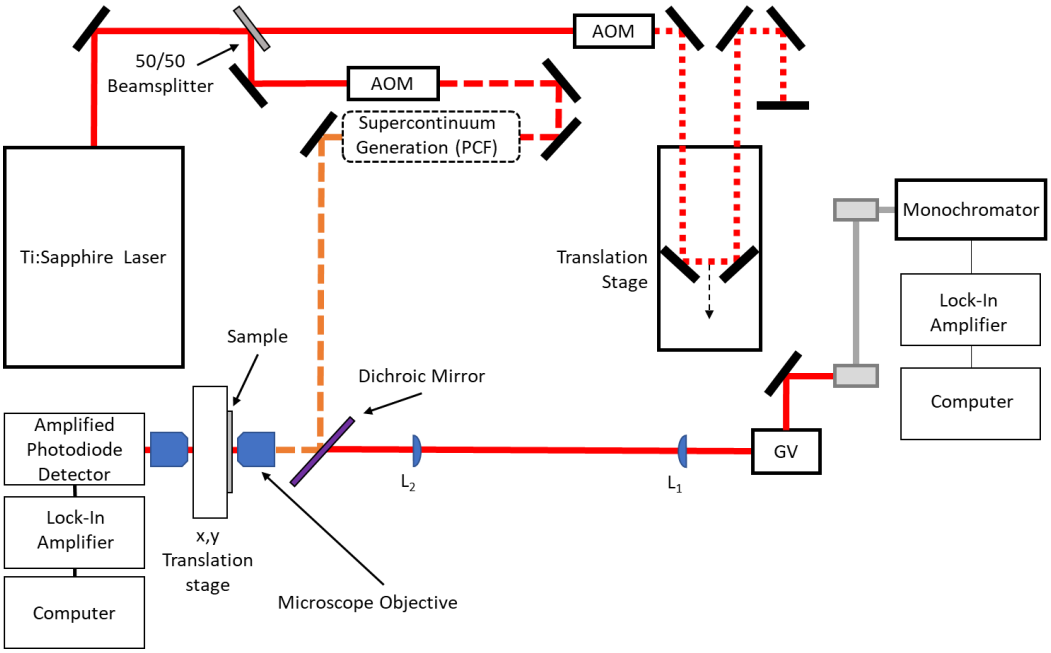

Figure 6.1. Diagram of home-built emission microscope. Abbreviations (AOM, GV, PCF) retain their original meanings from Figure 1.1.

Figure 6.2 shows the characterization of a single domain of $MAPbI_3$. A spatially overlapped pump-probe image of the domain is shown in Panel A and accompanied by an emission image (collected by holding the monochromator at a single wavelength and raster scanning the sample beneath the excitation pulse using a piezoelectric stage) collected at $\lambda = 772$ nm in Panel B. Panel C shows emission spectra collected at the labelled spots from the image in Panel B. Shifting in the emission spectra suggests that the local electronic structure varies from point-to-point on a single crystalline domain, likely due to varying defect densities or degrees of local disorder. Such local

heterogeneity would also affect carrier transport since variance in the defect density or ordering parameters would cause the scattering time of photogenerated carriers to change. While we have not yet correlated shifts in the emission spectra to changes in carrier transport, we are in the process of collecting more data similar to that shown in Figure 6.2 (as well as accompanying diffusion and carrier recombination data).

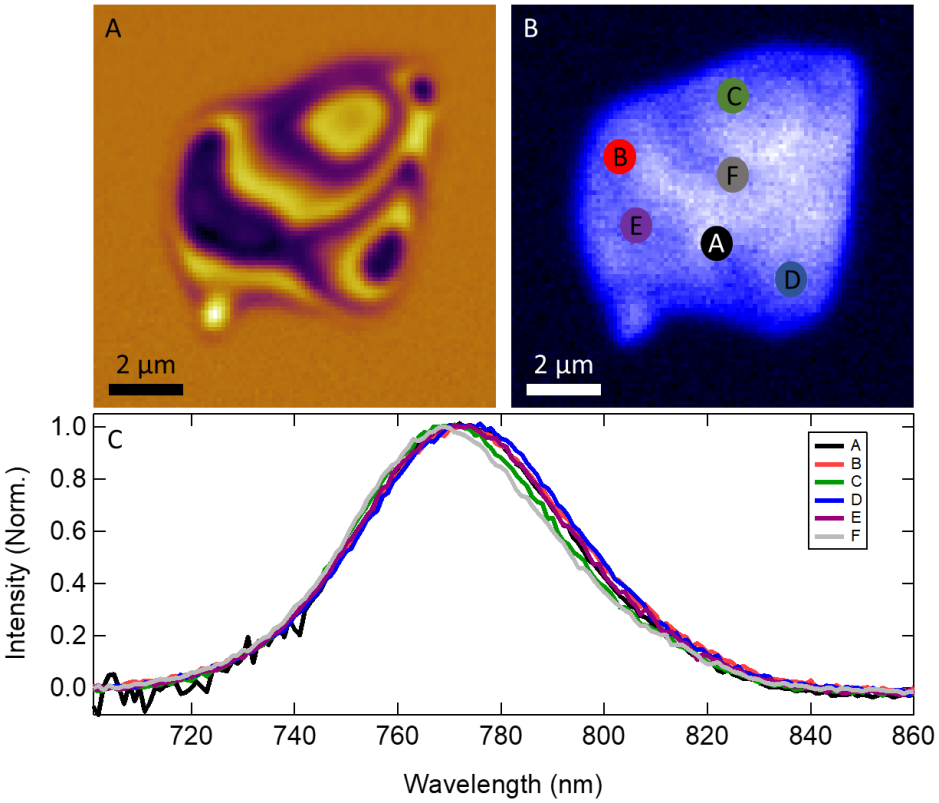

Figure 6.2. Heterogeneous local emission from $MAPbI_3$ crystallite. (A) Pump-probe image of $MAPbI_3$ crystallite. (B) Emission image of $MAPbI_3$ crystallite collected at λ = 772 nm. (C) Emission spectra collected from crystallite shown in panels A, B.

6.2.2 Quantifying the Effect of Synthetic Procedure on Carrier Transport and Recombination Dynamics

While the work in this dissertation has uncovered significant heterogeneity in the photoresponse of perovskite crystallites on the same sample, very little work has been

done in comparing the dynamics seen on samples prepared using different fabrication techniques. It is known in the literature that the methodology used to synthesize perovskites has a tangible effect on their optical properties,[108] quantifying those effects is challenging due to the number of spectroscopic techniques used to characterize these materials. Different spectroscopies each display different dependencies on crystalline quality, grain boundary density, and a host of other sample parameters, making comparisons of measurements made with different techniques difficult to draw and hard to trust.

Most of our work was conducted on thin-film samples prepared by the various solution processed techniques detailed in Chapters 2 - 5. However, alternative methods towards arriving at highly crystalline samples have been reported in the literature, ranging from slow growth[81] (and spin-coating[69]) of large (millimeter-scale) single crystals to chemical vapor deposition of highly crystalline thin-films.[139-140] Our research group currently has access to a home built chemical vapor deposition oven as well as the facilities required for slow growth of large crystallites, opening the possibility for our laboratory to characterize the excited state of single-crystalline perovskite samples prepared in a variety of ways. Using ultrafast microscopy to characterize perovskites with identical stoichiometries that are prepared using a number of different protocols would provide a tangible benefit to not only the perovskite photophysics community at large but for those who endeavour to design more efficient perovskite-based optoelectronic devices.

6.2.3 Determining the Cause of Anisotropic Carrier Diffusion in $MAPbI_3$

Throughout our studies of carrier transport in $MAPbI_3$ we identified multiple domains which displayed anisotropic diffusion of photogenerated carriers. In Figure 6.3 we display data demonstrating this phenomenon. Panel A shows a pump-probe image of a perovskite crystallite with an accompanying SEM image in Panel B. Spatially separated images of the photogenerated carrier cloud taken at increasing temporal delays are shown in Panel C. While initially we believed the anisotropic diffusion we observed to be a consequence of grain boundary or surface roughness effects, correlation of the diffusion measurements with SEM images of the crystallites cast doubt on this conclusion. The data shown in Figure 6.3, as shown in Panel B, was collected from section of a domain with high surface quality and no apparent grain-boundaries within the sampled volume that would have impeded carrier transport in one direction. Despite this, we recover diffusivities in the x- and y- direction differing by nearly 30%

.

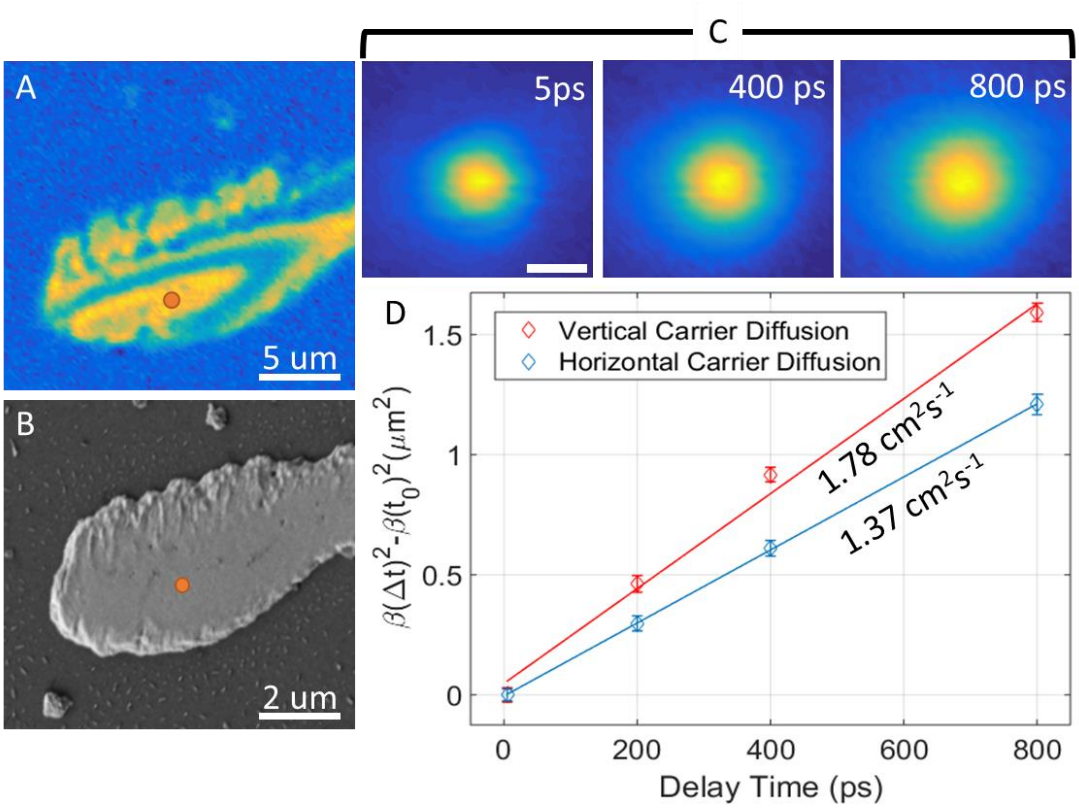

Figure 6.3. Anisotropic diffusion in $MAPbI_3$. (A) Spatially overlapped image of $MAPbI_3$ crystallite. (B) SEM image of crystallite shown in Panel A. (C) Spatially separated images of photogenerated carrier cloud taken at increasing delay times from point denoted by orange circle in Panel A. (D) Carrier diffusion in the x- and y- directions determined from the images shown in Panel C. Panels A, B, and C are reproduced from Figure 1.4.

One potential cause of this anisotropic diffusion could be the tetragonal crystal structure of $MAPbI_3$. Tetragonal crystals have two lattice parameters which are identical to each other and one longer than those two. In $MAPbI_3$ the lattice parameters are $a = b =$ 8.81 Å and c = 12.83 Å.[141] A difference between the lattice parameters of the directions in which charge carriers are diffusing would suggest that carriers traveling in different directions would experience different energetic landscapes, potentially changing their transport properties.

Charge carriers displaying different diffusivity depending on the crystalline axis along which they diffuse would also explain why anisotropic diffusion is seen in some crystals but not others. In the event that the x- and y- axes of the laboratory frame correspond to the *a* and *b* axes of the crystallite, the observed diffusion would be isotropic. However, if the *c* axis of the crystal corresponds to either axis along which diffusion is imaged during our experiments, diffusion in that direction would be altered relative to the other. The inconsistency with which we observe anisotropic diffusion is a logical result, since the absolute orientation of the crystallites is likely randomized across the sample due to the methods by which these materials are manufactured.

REFERENCES CITED

(42) Pankove, J. I. *Optical Processes in Semiconductors*. Dover Publications, Inc.: New York, 1971.

(69) Nie, W.; Tsai, H.; Asadpour, R.; Blancon, J.-C.; Neukirch, A. J.; Gupta, G.; Crochet, J. J.; Chhowalla, M.; Tretiak, S.; Alam, M. A.; et al. High-Efficiency Solution-Processed Perovskite Solar Cells with Milimeter-Scale Grains. *Science* **2015,** *347*, 522-525.

(81) Yang, Y.; Yan, Y.; Yang, M.; Choi, S.; Zhu, K.; Luther, J. M.; Beard, M. C. Low Surface Recombination Velocity in Solution-Grown $CH_3NH_3PbBr_3$ Perovskite Single Crystal. *Nat. Commun.* **2015,** *6:7961*.

(108) Herz, L. M. Charge-Carrier Mobilities in Metal Halide Perovskites: Fundamental Mechanisms and Limits. *ACS Energy Lett.* **2017,** *2*, 1539-1548.

(139) Tavakoli, M. M.; Gu, L.; Gao, Y.; Reckmeier, C.; He, J.; Rogach, A. L.; Yao, Y.; Fan, Z. Fabrication of Efficient Planar Perovskite Solar Cells Using a One-Step Chemical Vapor Deposition Method. *Sci. Rep.* **2015,** *5*, 14083.

(140) Wang, Y.; Guan, X.; Li, D.; Cheng, H.-C.; Duan, X.; Lin, Z.; Duan, X. Chemical Vapor Deposition Growth of Single-Crystalline Cesium Lead Halide Microplatelets and Heterostructures for Optoelectronic Applications. *Nano Research* **2017,** *10*, 1223-1233.

(141) Brivio, F.; Frost, J. M.; Skelton, J. M.; Jackson, A. J.; Weber, O. J.; Weller, M. T.; Goñi, A. R.; Leguy, A. M. A.; Barnes, P. R. F.; Walsh, A. Lattice Dynamics and Vibrational Spectra of the Orthorhombic, Tetragonal, and Cubic Phases of Methylammonium Lead Iodide. *Phys. Rev. B* **2015,** *92*, 144308.

APPENDICES

APPENDIX A

SUPPORTING INFORMATION FOR CHAPTER 3

A.1 Supporting Information for Chapter 3
Calculation of Pump Fluences and Carrier Density

The pump pulse at the sample position is modeled as a two-dimensional Gaussian:

$$G(r) = \frac{I_0 4\ln(2)}{\sigma^2 \pi} \exp\left[-\frac{4r^2 \ln(2)}{\sigma^2} \right] \qquad (3.4)$$

Where I_0 is the measured energy of the pump pulse accounting for the transmittance of the microscope objective at 600 nm, and σ is the full-width at half-maximum of the laser spot at the sample. Reported fluences are calculated with Equation 3.5 assuming r_0 = 0.60*fwhm (1/e width):

$$\frac{\int_0^{2\pi} \int_0^{r_0} G(r)\, r\, \partial r\, \partial \phi}{\int_0^{2\pi} \int_0^{r_0} r\, \partial r\, \partial \phi} \qquad (3.5)$$

Carrier densities are calculated in a similar manner with depth given by the 1/e absorption length (assuming Beer-Lambert absorption).[142]

REFERENCES CITED

(142) Yakunin, S.; Sytnyk, M.; Kriegner, D.; Shrestha, S.; Richter, M.; Matt, G. J.; Azimi, H.; Brabec, C. J.; Stangl, J.; Kovalenko, M. V.; et al. Detection of X-Ray Photons by Solution-Processed Lead Halide Perovskites. *Nat. Photonics* **2015,** *9*, 444-449.

APPENDIX B

SUPPORTING INFORMATION FOR CHAPTER 4

B.1 Transfer Matrix Modeling

The perovskite domain is modeled as a stack of thin slabs (d = 1 nm), each of which is characterized by a phase matrix (Equation 4.3) that accounts for the accumulated phase as the probe field propagates through slab k with refractive index, n_k:

$$U_k = \begin{vmatrix} e^{2i\pi n_k d/\lambda} & 0 \\ 0 & e^{-2i\pi n_k d/\lambda} \end{vmatrix} \qquad (4.3)$$

Reflection and transmission at the interfaces is determined by the refraction matrix (Equation 4.4):

$$V_{k-1,k} = \frac{1}{t_k}\begin{vmatrix} 1 & r_k \\ r_k & 1 \end{vmatrix} \quad (4.4)$$

where $r_k = (n_{k-1} - n_k)/(n_{k-1} + n_k)$ and $t_k = 2n_{k-1}/(n_{k-1} + n_k)$ are the reflection and transmission coefficients. The optical response of the domain is determined by the characteristic matrix, M:

$$M = V_{0,1}U_1V_{1,2}U_2 \ldots V_{j,j+1} = \begin{vmatrix} m_{11} & m_{12} \\ m_{21} & m_{22} \end{vmatrix} \quad (4.5)$$

where the $V_{0,1}$ and $V_{j,j+1}$ refraction matrices describe the air-perovskite and perovskite substrate interfaces, respectively. The refractive index of each slab is modeled by Equation 1 and an exponentially decreasing carrier density according the absorption coefficient of the material. The reflection coefficient of the system described by matrix M is given by the modulus square of the ratio of two matrix elements:

$$R_M = \left|\frac{m_{21}}{m_{11}}\right|^2 \quad (4.6)$$

B.2 Pump-Probe Image Fitting

To extract the material parameters, the following fitting procedure was followed. The ground-state (GS) reflectivity image, pump-probe (PP) reflectivity image, and atomic force micrograph (AFM) of a single perovskite domain were pixel matched and interpolated so that correlated data points from each image lay at the same grid position. The GS reflectivity image is filtered with a median filter to eliminate low frequency scattering background, leaving only the fringes centered at R = 0. The filtered ground state images are fit with the transfer matrix method described above (altered slightly to include a Gaussian filter which mimics the point spread function of our microscope) to extract a scaling factor, which accounts for reduction in amplitude of the Fabry-Perot fringes due the non-ideal finesse of the domains (caused by interface roughness, absorption, bulk scattering, etc.).

PP images are fit using the transfer matrix method (scaled by the GS-determined factor) along with Equation 1 from the main body of this paper. The refractive index change in each layer is determined by Equation 4.1 with τ and n_0 serving as the only fitting parameters. Qualitatively, n_0 determines the position of the modes and τ determines the amplitude. The modeled ground state images shown in Figure 4.1 are reproduced using the ground state refractive index extracted from these pump-probe image fits. Throughout our fitting we assume the absorption cross section at the probe wavelength to be 0.

B.3 Photogenerated Carrier Density Calculations

The pump pulse at the sample position is modeled as a two-dimensional Gaussian:

$$g(r) = \frac{I_0 4\ln(2)}{\sigma^2 \pi} \exp\left[-\frac{4r^2 \ln(2)}{\sigma^2} \right] \qquad (4.7)$$

Where I_0 is the measured energy of the pump pulse, accounting for the transmittance of the microscope objective at 600 nm and reflection of incident pump photons off the perovskite/air interface, and σ is the full-width at half-maximum of the laser spot at the sample. Pulse fluence is calculated as:

$$G(r) = \frac{\int_0^{2\pi} \int_0^{r_0} g(r)\, r\, \partial r\, \partial \phi}{\int_0^{2\pi} \int_0^{r_0} r\, \partial r\, \partial \phi} \qquad (4.8)$$

Where r_0 is the $1/e^2$ width of the pulse. Since images are collected when the probe beam is spatially overlapped with the pump an additional term must be included to account for the number of carriers seen by the probe:[44]

$$N_c = N_R \left[\left(1 + \frac{\sigma_{x,probe}}{\sigma_{x,pump}}\right)^2 \left(1 + \frac{\sigma_{y,probe}}{\sigma_{y,pump}}\right)^2 \right]^{-1/2} \qquad (4.9)$$

Where N_R is the calculated carrier density corrected for reflectivity of the pump pulse and $\sigma_{x/y,pump/probe}$ is the $1/e^2$ widths of the respective pulses. Due to the depth-variant nature of our model, a different carrier density is calculated for each slab of the material assuming Beer's law absorption. Previously reported absorption cross sections at the pump wavelength were used. [54, 143]

B.4 Optical Determination of m* and τ for Silicon

The experiments detailed in the main body of the paper were duplicated on a Si (100) wafer. In the case of samples which are optically thick to the probe pulse, the transfer matrix approach used in the main body of this manuscript is unnecessary and Δn can be solved for explicitly using the Fresnel equations:

$$\Delta n = \left(\frac{\Delta R}{R}\right)\frac{(n_0{}^2-1)\left[n_0{}^2-\sin(\theta)^2\right]^{1/2}}{4n_0\cos(\theta)} \qquad (4.10)$$

Here, θ is the incident angle of the probe pulse and all other variables retain their original meanings from the main body of this manuscript. An ambipolar diffusivity of 9.2 cm^2s^{-1} and refractive index change (determined from ΔR/R measurements[43]) of $\Delta n = 2.98 \times 10^{-3}$ were measured at a carrier density of 6.0 +/- 0.1 × 10^{18} cm^{-3}.

To graphically represent this solution, Equation 4.1 and Equation 4.2 are both recast in terms of τ and m*:

$$\tau = -\left(\frac{2\varepsilon_0 m^* n_0 \Delta n}{e^2 N - 2\Delta n m \varepsilon_0 n_0 \omega^2}\right)^{1/2} \qquad (4.11)$$

$$\tau = \frac{2m^* D_{am}}{K_b T} \qquad (4.12)$$

With both equations expressed in terms of τ they can be plotted simultaneously as shown in Figure 4.5. The intersection of these two lines, with Equation 4.11 shown as a red solid line and Equation 4.12 displayed as a red dashed line, represents the simultaneous solution of the two equations. From these experiments, we determine an optical mass of m* = .15 m_0 and a mean scattering time of τ = 63 fs, both of which compare favorably with known values.[43, 144]

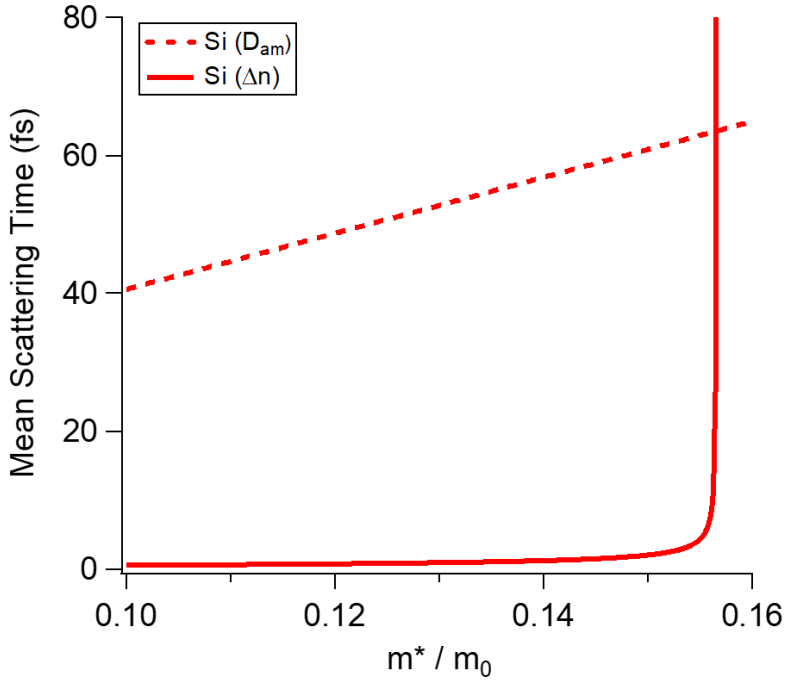

Figure 4.5. Determination of optical mass and scattering time of Si. Optical mass expressed in units of resting electron mass. Scattering time expressed in femtoseconds.

Examination of Figure 4.5 reveals the Drude response to be asymptotic in two limits of the carrier response to the field. In one limit ($\omega^2\tau^2 \gg 1$), the scattering time is poorly determined because the charges do not experience a scattering event during a single optical cycle of the probe (2.67 fs at λ_{probe} = 800 nm). In the other limit ($\omega^2\tau^2 \ll 1$), effective mass is poorly determined because the charges experience many scattering events during a single optical cycle. Most inorganic semiconducting materials fall into the former limit, as shown above for Silicon, where the scattering time is much longer than an optical cycle of visible light. While this allows for explicit determination of the carrier optical mass, as mentioned above the carrier scattering time remains undefined. In all three cases (the short and long scattering time limits as well as the intermediate case of $\omega^2\tau^2 \approx 1$), because

Equation 1 conflates the effects of the carrier optical mass and mean scattering time, a second measurement is required to uniquely determine both parameters.

B.5 Early Time Dynamics of $MAPbBr_3$ and $CsPbBr_3$

For $MAPbI_3$, excitation at 600 nm (2.06 eV) photogenerates carriers with 0.44 eV excess energy above the bandgap (1.62 eV). For $CsPbBrI_2$, excitation at 550 nm (2.25 eV) photogenerates carriers with 0.28 eV excess energy above the bandgap (1.97 eV). For both cases, the moderate excitation densities and the low excess energy relative to the bandgap ensures that the carriers have cooled to the band edge at the delay times probed in the reflectivity images.[74, 145]

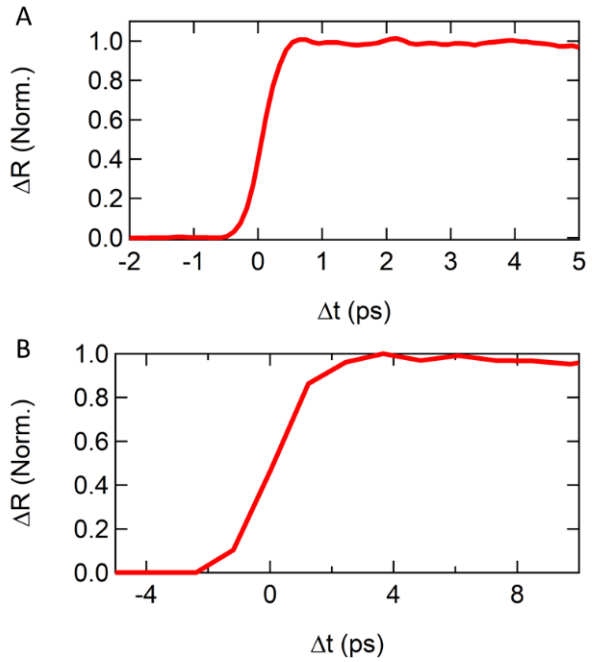

Figure 4.6. Early time kinetics of (A) $MAPbI_3$ and (B) $CsPbBrI_2$ samples showing maximum transient response of each sample at 2 ps and 4 ps, respectively.

B.6 Fluence Dependence of ΔR/R

For $MAPbI_3$, the pump fluence was 13.1 μJ cm^{-2}, corresponding to an average excitation density (at $1/e^2$) of 7.8×10^{17} cm^{-3}. For $CsPbBrI_2$, the pump fluence was 2.8 μJ cm^{-2}, corresponding to an average excitation density (at $1/e^2$) of 8.7×10^{16} cm^{-3}. In both cases, the (normalized) transient reflectivity kinetics were verified to be power independent. The signal magnitude at these excitation densities scale linearly with the pump power, as expected from the Drude response.

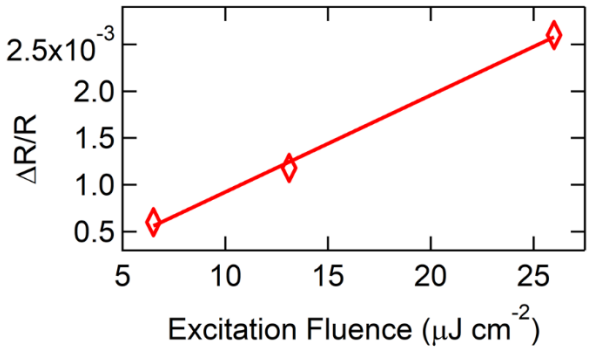

Figure 4.7 Linear dependence of signal magnitude on excitation fluence for $MAPbI_3$.

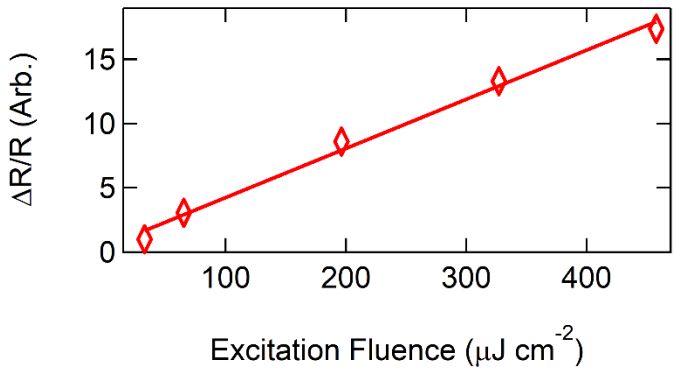

Figure 4.8. Data demonstrating a linear dependence of signal magnitude on excitation fluence at the fluences used in this manuscript for $CsPbBrI_2$.

B.7 Diffusivity Measurements

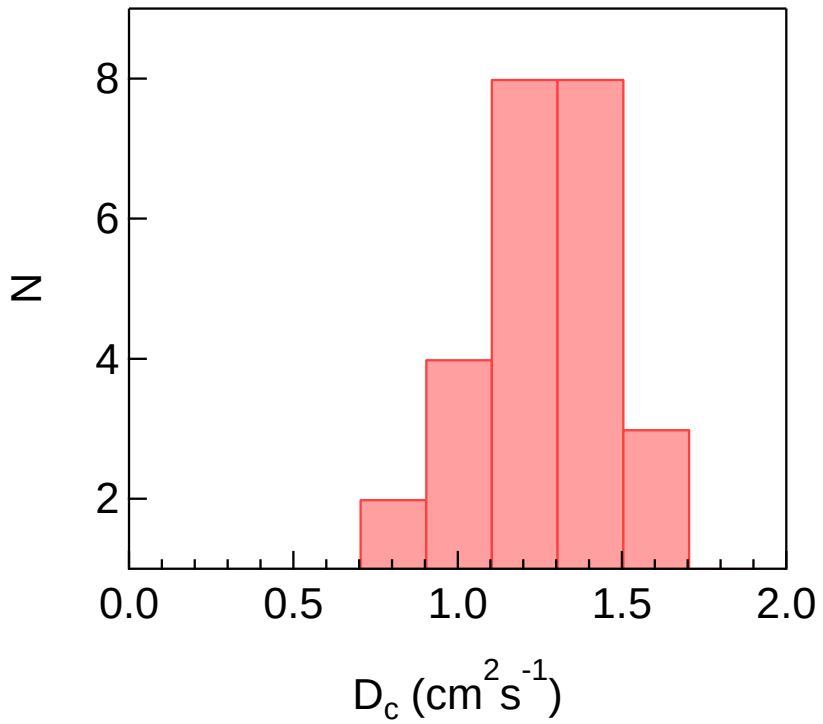

Figure 4.9. Histogram of diffusion measurements collected from individual $MAPbI_3$ domains. The average value of 1.2 cm^2/s is used in the calculation of m* and τ. Measurements reproduced here from Chapter 3.

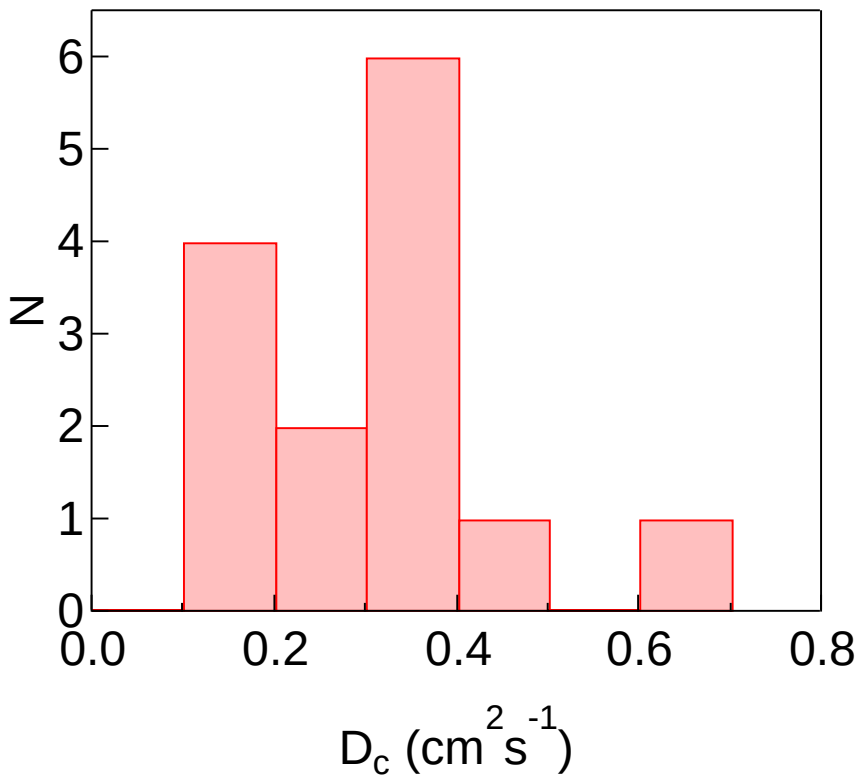

Figure 4.10. Histogram of diffusion measurements collected from individual $CsPbBrI_2$ perovskite domains. The value of 0.31 cm^2/s (used in the calculation of m* and τ) is comprised of 12 measurements, previously reported in Ref. 6, as well as 2 additional measurements which have been collected since.

REFERENCES CITED

(43) Sabbah, A. J.; Riffe, D. M. Measurement of Silicon Surface Recombination Velocity Using Ultrafast Pump–Probe Reflectivity in the near Infrared. *J. Appl. Phys.* **2000,** *88*, 6954-6956.

(44) Sabbah, A. J.; Riffe, D. M. Femtosecond Pump-Probe Reflectivity Study of Silicon Carrier Dynamics. *Phys. Rev. B* **2002,** *66*, 165217.

(54) Kennedy, C. L.; Hill, A. H.; Massaro, E. S.; Grumstrup, E. M. Ultrafast Excited-State Transport and Decay Dynamics in Cesium Lead Mixed Halide Perovskites. *ACS Energy Lett.* **2017,** *2*, 1501-1506.

(74) Fu, J.; Xu, Q.; Han, G.; Wu, B.; Huan, C. H. A.; Leek, M. L.; Sum, T. C. Hot Carrier Cooling Mechanisms in Halide Perovskites. *Nat. Commun.* **2017,** *8*, 1300.

(143) Guerra, J. A.; Tejada, A.; Korte, L.; Kegelmann, L.; Töfflinger, J. A.; Albrecht, S.; Rech, B.; Weingärtner, R. Determination of the Complex Refractive Index and Optical Bandgap of CH3NH3PbI3 Thin Films. *J. Appl. Phys.* **2017,** *121*, 173104.

(144) Riffe, D. M. Temperature Dependence of Silicon Carrier Effective Masses with Application to Femtosecond Reflectivity Measurements. *J. Opt. Soc. Am. B* **2002,** *19*, 1092-1100.

(145) Nah, S.; Spokoyny, B. M.; Soe, C. M. M.; Stoumpos, C. C.; Kanatzidis, M. G.; Harel, E. Ultrafast Imaging of Carrier Cooling in Metal Halide Perovskite Thin Films. *Nano Lett.* **2018,** *18*, 1044-1048.

CUMULATIVE REFERENCES CITED

(1) Shank, C. V.; Yen, R.; Hirlimann, C. Time-Resolved Reflectivity Measurements of Femtosecond-Optical-Pulse-Induced Phase Transitions in Silicon. *Phys. Rev. Lett.* **1983,** *50*, 454-457.

(2) Massaro, E. S.; Hill, A. H.; Grumstrup, E. M. Super-Resolution Structured Pump–Probe Microscopy. *ACS Photonics* **2016,** *3*, 501-506.

(3) Mehl, B. P.; Kirschbrown, J. R.; House, R. L.; Papanikolas, J. M. The End Is Different Than the Middle: Spatially Dependent Dynamics in Zno Rods Observed by Femtosecond Pump-Probe Microscopy. *J. Phys. Chem. Lett.* **2011,** *2*, 1777-1781.

(4) Blake, J. C.; Eldridge, P. S.; Gundlach, L. Spatial Variation in Carrier Dynamics Along a Single Cdsse Nanowire. *Chem. Phys.* **2014,** *442*, 128-131.

(5) Simpson, M. J.; Doughty, B.; Yang, B.; Xiao, K.; Ma, Y.-Z. Spatial Localization of Excitons and Charge Carriers in Hybrid Perovskite Films. *J. Phys. Chem. Lett.* **2015,** *6*, 3041-3047.

(6) Tian, Y.; Merdasa, A.; Peter, M.; Abedellah, M.; Zheng, K.; Jr., C. S. P.; Pullerits, T.; Yartsev, A.; Sundstrom, V.; Scheblykin, I. G. Giant Photoluminescence Blinking of Perovskite Nanocrystals Reveals Single-Trap Control of Luminescence. *Nano Lett.* **2015,** *15*, 1603-1608.

(7) de Quilettes, D. W.; Vorpahl, S. M.; Stranks, S. D.; Nagaoka, H.; Eperon, G. E.; Ziffer, M. E.; Snaith, H. J.; Ginger, D. S. Impact of Microstructure on Local Carrier Lifetime in Perovskite Solar Cells. *Science* **2015,** *348*, 683-686.

(8) Nah, S.; Spokoyny, B.; Stoumpos, C.; Soe, C. M. M.; Kanatzidis, M.; Harel, E. Spatially Segregated Free-Carrier and Exciton Populations in Individual Lead Halide Perovskite Grains. *Nat. Photonics* **2017,** *11*, 285-288.

(9) Hill, A. H.; Smyser, K. E.; Kennedy, C. L.; Massaro, E. S.; Grumstrup, E. M. In *Transient Absorption Imaging of Carrier Dynamics in Disordered Semiconductors*, 2017; pp 101930W-101930W-8.

(10) Kojima, A.; Teshima, K.; Shirai, Y.; Miyasaka, T. Organometal Halide Perovskites as Visible-Light Sensitizers for Photovoltaic Cells. *J. Am. Chem. Soc.* **2009,** *131*, 6050-6051.

(11) Levelized Cost of New Electricity Generating Technologies. https://www.instituteforenergyresearch.org/studies/levelized-cost-of-new-generating-technologies/ (accessed 1/4/2018).

(12) Li, C.-M.; Sjodin, T.; Dai, H.-L. Photoexcited Carrier Diffusion near a Si(111) Surface: Non-Negligible Consequence of Carrier-Carrier Scattering. *Phys. Rev. B* **1997,** *56*, 15252-15255.

(13) Stranks, S. D.; Eperon, G. E.; Grancini, G.; Menelaou, C.; Alcocer, M. J. P.; Leijtens, T.; Herz, L. M.; Petrozza, A.; Snaith, H. J. Electron-Hole Diffusion Lengths Exceeding 1 Micrometer in Organometal Trihalide Perovskite Absorber. *Science* **2013,** *342*, 641-344.

(14) Zhang, W.; Saliba, M.; Moore, D. T.; Pathak, S. K.; Hörantner, M. T.; Stergiopoulos, T.; Stranks, S. D.; Eperon, G. E.; Alexander-Webber, J. A.; Abate, A.; et al. Ultrasmooth Organic-Inorganic Perovskite Thin-Film Formation and Crystallization for Efficient Planar Heterojunction Solar Cells. *Nat. Commun.* **2015,** *6*, 6142.

(15) Guo, Z.; Manser, J. S.; Wan, Y.; Kamat, P. V.; Huang, L. Spatial and Temporal Imaging of Long-Range Charge Transport in Perovskite Thin Films by Ultrafast Microscopy. *Nat. Commun.* **2015,** *6*, 7471.

(16) Christians, J. A.; Manser, J. S.; Kamat, P. V. Multifaceted Excited State of $CH_3NH_3PbI_3$. Charge Separation, Recombination, and Trapping. *J. Phys. Chem. Lett.* **2015,** *6*, 2086-2095.

(17) Manser, J. S.; Kamat, P. V. Band Filling with Free Charge Carriers in Organometal Halide Perovskites. *Nat. Photonics* **2014,** *8*, 737-743.

(18) Im, J.-H.; Jang, I.-H.; Pellet, N.; Grätzel, M.; Park, N.-G. Growth of $CH_3NH_3PbI_3$ Cuboids with Controlled Size for High-Efficiency Perovskite Solar Cells. *Nat. Nanotechnol.* **2014,** *9*, 927-932.

(19) Kim, H.-S.; Im, S. H.; Park, N.-G. Organolead Halide Perovskite: New Horizons in Solar Cell Research. *J. Phys. Chem. C* **2014,** *118*, 5615-5625.

(20) Tan, Z.-K.; Moghaddam, R. S.; Lai, M. L.; Docampo, P.; Higler, R.; Deschler, F.; Price, M.; Sadhanala, A.; Pazos, L. M.; Credgington, D.; et al. Bright Light-Emitting Diodes Based on Organometal Halide Perovskite. *Nat. Nanotechnol.* **2014,** *9*, 687-692.

(21) Zhang, Q.; Ha, S. T.; Liu, X.; Sum, T. C.; Xiong, Q. Room-Temperature near-Infared High-Q Perovskite Whispering-Gallery Planar Nanolasers. *Nano Lett.* **2014,** *14*, 5995-6001.

(22) Fang, Y.; Dong, Q.; Shao, Y.; Yuan, Y.; Huang, J. Highly Narrowband Perovskite Single-Crystal Photodetectors Enabled by Surface-Charge Recombination. *Nat. Photonics* **2015,** *9*, 679-686.

(23) Xing, G.; Matthews, N.; Sun, S.; Lim, S. S.; Lam, Y. M.; Gratzel, M.; Mhaisalkar, S.; T.C., S. Long-Range Balanced Electron- and Hole-Transport Lengths in Organic-Inorganic CH3NH3PbI3. *Science* **2013,** *342*, 344-347.

(24) Lin, Q.; Armin, A.; Nagiri, R. C. R.; Burn, P. L.; Meredith, P. Electro-Optics of Perovskite Solar Cells. *Nat. Photonics* **2014,** *9*, 106-112.

(25) Sun, S.; Salim, T.; Matthews, N.; Duchamp, M.; Boothroyd, C.; Xing, G.; Sum, T. C.; Lam, Y. M. The Origin of High Efficiency in Low-Temperature Solution-Processable Bilayer Organimetal Halide Hybrid Solar Cells. *Energy Environ. Sci* **2014,** *7*, 399-407.

(26) Tian, W.; Zhao, C.; Leng, J.; Cui, R.; Jin, S. Visualizing Carrier Diffusion in Individual Single-Crystal Organolead Halide Perovskite Nanowires and Nanoplates. *J. Am. Chem. Soc.* **2015,** *137*, 12458-12461.

(27) Dong, Q.; Fang, Y.; Shao, Y.; Mulligan, P.; Qiu, J.; Cao, L.; Huang, J. Electron-Hole Diffusion Lengths > 175 Mm in Solution-Grown $CH_3NH_3PbI_3$ Single Crystals. *Science* **2015,** *347*, 967-970.

(28) Grumstrup, E. M.; Gabriel, M. M.; Pinion, C. W.; Parker, J. K.; Cahoon, J. F.; Papanikolas, J. M. Reversible Strain-Induced Electron-Hole Recombination in Silicon Nanowires Observed with Femtosecond Pump-Probe Microscopy. *Nano Lett.* **2014,** *14*, 6287-6292.

(29) Grumstrup, E. M.; Cating, E. M.; Gabriel, M. M.; Pinion, C. W.; Christesen, J. D.; Kirschbrown, J. R.; Vallorz, E. L.; Cahoon, J. F.; Papanikolas, J. M. Ultrafast Carrier Dynamics of Silicon Nanowire Ensembles: The Impact of Geometrical Heterogeneity on Charge Carrier Lifetime. *J. Phys. Chem. C* **2014,** *118*, 8626-8633.

(30) Grumstrup, E. M.; Gabriel, M. M.; Cating, E. M.; Pinion, C. W.; Christesen, J. D.; Kirschbrown, J. R.; Vallorz, E. L.; Cahoon, J. F.; Papanikolas, J. M. Ultrafast Carrier Dynamics in Individual Silicon Nanowires: Characterization of Diameter-Dependent Carrier Lifetime and Surface Recombination with Pump–Probe Microscopy. *J. Phys. Chem. C* **2014,** *118*, 8634-8640.

(31) Wong, C. T. O.; Lo, S. S.; Huang, L. Ultrafast Spatial Imaging of Charge Dynamics in Heterogeneous Polymer Blends. *J. Phys. Chem. Lett.* **2012,** *3*, 879-884.

(32) Gao, B.; Hartland, G. V.; Huang, L. Transient Absorption Spectroscopy of Excitons in an Individual Suspended Metallic Carbon Nanotube. *J. Phys. Chem. Lett.* **2013,** *4*, 3050-3055.

(33) Dai, D. C.; Monkman, A. P. Observation of Superfluorescence from a Quantum Ensemble of Coherent Excitons in a Znte Crystal: Evidence for Spontaneous Bose-Einstein Condensation of Excitons. *Phys. Rev. B* **2011,** *84*, 115206.

(34) Zhang, Q.; Liu, X.; Utama, M. I. B.; Zhang, J.; de la Mata, M.; Arbiol, J.; Lu, Y.; Sum, T. C.; Xiong, Q. Highly Enhanced Exciton Recombination Rate by Strong Electron–Phonon Coupling in Single Znte Nanobelt. *Nano Letters* **2012,** *12*, 6420-6427.

(35) Liu, Q.; Wang, Y.; Sui, N.; Wang, Y.; Chi, X.; Wang, Q.; Chen, Y.; Ji, W.; Zou, L.; Zhang, H. Exciton Relaxation Dynamics in Photo-Excited CsPbI3 Perovskite Nanocrystals. *Sci. Rep.* **2016,** *6*, 29442.

(36) de Jong, E. M. L. D.; Yamashita, G.; Gomez, L.; Ashida, M.; Fujiwara, Y.; Gregorkiewicz, T. Multiexciton Lifetime in All-Inorganic $CsPbBr_3$ Perovskite Nanocrystals. *J. Phys. Chem. C* **2017,** *121*, 1941-1947.

(37) Hoffman, C. A.; Jarašiūnas, K.; Gerritsen, H. J.; Nurmikko, A. V. Measurement of Surface Recombination Velocity in Semiconductors by Diffraction from Picosecond Transient Free-Carrier Gratings. *Appl. Phys. Lett.* **1978,** *33*, 536-539.

(38) Ling, Z. G.; Ajmera, P. K.; Kousik, G. S. Simultaneous Extraction of Bulk Lifetime and Surface Recombination Velocities from Free Carrier Absorption Transients. *J. Appl. Phys.* **1994,** *75*, 2718-2720.

(39) Yu, Z. G.; Krishnamurthy, S.; Guha, S. Photoexcited-Carrier-Induced Refractive Index Change in Small Bandgap Semiconductors. *J. Opt. Soc. Am. B* **2006,** *23*, 2356-2360.

(40) Piatkowski, P.; Cohen, B.; Javier Ramos, F.; Di Nunzio, M.; Nazeeruddin, M. K.; Gratzel, M.; Ahmad, S.; Douhal, A. Direct Monitoring of Ultrafast Electron and Hole Dynamics in Perovskite Solar Cells. *Phys. Chem. Chem. Phys.* **2015,** *17*, 14674-14684.

(41) Elliot, R. J.; Gibson, A. F. *An Introduction to Solid State Physics and Its Applications*. The Macmillan Press Ltd.: United Kingdom, 1974.

(42) Pankove, J. I. *Optical Processes in Semiconductors*. Dover Publications, Inc.: New York, 1971.

(43) Sabbah, A. J.; Riffe, D. M. Measurement of Silicon Surface Recombination Velocity Using Ultrafast Pump–Probe Reflectivity in the near Infrared. *J. Appl. Phys.* **2000,** *88*, 6954-6956.

(44) Sabbah, A. J.; Riffe, D. M. Femtosecond Pump-Probe Reflectivity Study of Silicon Carrier Dynamics. *Phys. Rev. B* **2002,** *66*, 165217.

(45) Bennett, B. R.; Soref, R. A.; Alamo, J. A. D. Carrier-Induced Change in Refractive Index of InP, GaAs and InGaAsP. *IEEE J. Quantum Electron.* **1990,** *26*, 113-122.

(46) Henry, C. H.; Logan, R. A.; Bertness, K. A. Spectral Dependence of the Change in Refractive Index Due to Carrier Injection in GaAs Lasers. *J. Appl. Phys.* **1981,** *52*, 4457-4461.

(47) Berggren, K. F.; Sernelius, B. E. Band-Gap Narrowing in Heavily Doped Many-Valley Semiconductors. *Phys. Rev. B* **1981,** *24*, 1971-1986.

(48) Klingshirn, C. *Semiconductor Optics*. 2nd ed.; Springer: Berlin, 2005.

(49) Price, M. B.; Butkus, J.; Jellicoe, T. C.; Sadhanala, A.; Briane, A.; Halpert, J. E.; Broch, K.; Hodgkiss, J. M.; Friend, R. H.; Deschler, F. Hot-Carrier Cooling and Photoinduced Refractive Index Changes in Organic-Inorganic Lead Halide Perovskites. *Nat. Commun.* **2015,** *6*, 8420.

(50) Hecht, E. *Optics*. Pearson Education: San Francisco, CA, 2002.

(51) Born, M.; Wolf, E. *Principles of Optics*. Pergamon Press: London, 1959.

(52) Feneberg, M.; Osterburg, S.; Lange, K.; Lidig, C.; Garke, B.; Goldhahn, R.; Richter, E.; Netzel, C.; Neumann, M. D.; Esser, N.; et al. Band Gap Renormalization and Burstein-Moss Effect in Silicon- and Germanium-Doped Wurtzite Gan up to 10^{20} Cm^{-3}. *Phys. Rev. B* **2014,** *90*, 075203.

(53) Hill, A. H.; Smyser, K. E.; Kennedy, C. L.; Massaro, E. S.; Grumstrup, E. M. Screened Charge Carrier Transport in Methylammonium Lead Iodide Perovskite Thin Films. *J. Phys. Chem. Lett.* **2017,** *8*, 948-953.

(54) Kennedy, C. L.; Hill, A. H.; Massaro, E. S.; Grumstrup, E. M. Ultrafast Excited-State Transport and Decay Dynamics in Cesium Lead Mixed Halide Perovskites. *ACS Energy Lett.* **2017,** *2*, 1501-1506.

(55) Sze, S. M. *Physics of Semiconductor Devices*. 3rd ed.; Wiley: New York, 2006.

(56) Shi, D.; Adinolfi, V.; Comin, R.; Yuan, M.; Alarousu, E.; Buin, A.; Chen, Y.; Hoogland, S.; Rothenberger, A.; Katsiev, K.; et al. Low Trap-State Density and Long Carrier Diffusion in Organolead Trihalide Perovskite Single Crystals. *Science* **2015,** *347*, 519-522.

(57) Savenije, T. J.; Carlito S. Ponseca, J.; Kunneman, L.; Abdellah, M.; Zheng, K.; Tian, Y.; Zhu, Q.; Canton, S. E.; Scheblykin, I. G.; Pullerits, T.; et al. Thermally Activated Exciton Dissociation and Recombination Control the Carrier Dynamics in Organometal Halide Perovskite. *J. Phys. Chem. Lett.* **2014,** *5*, 2189-2194.

(58) Chen, Q.; Zhou, H.; Song, T.-B.; Luo, S.; Hong, Z.; Duan, H.-S.; Dou, L.; Liu, Y.; Yang, Y. Controllable Self-Induced Passivation of Hybrid Lead Iodide Perovskites toward High Performance Solar Cells. *Nano Lett.* **2014,** *14*, 4158-4163.

(59) Draguta, S.; Thakur, S.; Morozov, Y. V.; Wang, Y.; Manser, J. S.; Kamat, P. V.; Kuno, M. Spatially Non-Uniform Trap State Densities in Solution-Processed Hybrid Perovskite Thin Films. *J. Phys. Chem. Lett.* **2016,** *7*, 715-721.

(60) Upadhya, P. C.; Martinez, J. A.; Li, Q.; Wang, G. T.; Swartzentruber, B. S.; Taylor, A. J.; Prasankumar, R. P. Space-and-Time-Resolved Spectroscopy of Single Gan Nanowires. *Appl. Phys. Lett.* **2015,** *106*, 5.

(61) Gabriel, M. M.; Grumstrup, E. M.; Kirschbrown, J. R.; Pinion, C. W.; Christesen, J. D.; Zigler, D. F.; Cating, E. E. M.; Cahoon, J. F.; Papanikolas, J. M. Imaging Charge Separation and Carrier Recombination in Nanowire P-I-N Junctions Using Ultrafast Microscopy. *Nano Lett.* **2014,** *14*, 3079-3087.

(62) Yu, K.; Devadas, M. S.; Major, T. A.; Lo, S. S.; Hartland, G. V. Surface Plasmon Polariton Propagation and Coupling in Gold Nanostructures. *J. Phys. Chem. C* **2014,** *118*, 8603-8609.

(63) Cui, Q.; Ceballos, F.; Kumar, N.; Zhao, H. Transient Absorption Microscopy of Monolayer and Bulk Wse2. *ACS Nano* **2014,** *8*, 2970-2976.

(64) Wong, C. Y.; Cotts, B. L.; Wu, H.; Ginsberg, N. S. Exciton Dynamics Reveal Aggregates with Intermolecular Order at Hidden Interfaces in Solution-Cast Organic Semiconducting Films. *Nat. Commun.* **2015,** *6:594*.

(65) Xiao, Z.; Dong, Q.; Bi, C.; Shao, Y.; Yuan, Y.; Huang, J. Solvent Annealing of Perovskite-Induced Crystal Growth for Photovoltaic-Device Efficiency Enhancement. *Adv. Mater.* **2014,** *26*, 6503-6509.

(66) Im, J.-H.; Luo, J.; Franckevicius, M.; Pellet, N.; Gao, P.; Moehl, T.; Zakeeruddin, S. M.; Nazeeruddin, M. K.; Gratzel, M.; Park, N.-G. Nanowire Perovskite Solar Cell. *Nano Lett.* **2015,** *15*, 2120-2126.

(67) Lee, M. M.; Teuscher, J.; Miyasaka, T.; Murakami, T. N.; Snaith, H. J. Efficient Hybrid Solar Cells Based on Meso-Superstructured Organometal Halide Perovskites. *Science* **2012,** *338*, 643-647.

(68) Liu, J.; Gao, C.; He, X.; Ye, Q.; Ouyang, L.; Zhuang, D.; Liao, C.; Mei, J.; Lau, W. Improved Crystallization of Perovskite Films by Optimized Solvent Annealing for High Efficiency Solar Cell. *ACS Appl. Mater. Interfaces* **2015,** *7*, 24008-24015.

(69) Nie, W.; Tsai, H.; Asadpour, R.; Blancon, J.-C.; Neukirch, A. J.; Gupta, G.; Crochet, J. J.; Chhowalla, M.; Tretiak, S.; Alam, M. A.; et al. High-Efficiency Solution-Processed Perovskite Solar Cells with Milimeter-Scale Grains. *Science* **2015,** *347*, 522-525.

(70) Wu, X.; Trinh, M. T.; Niesner, D.; Zhu, H.; Norman, Z.; Owen, J. S.; Yaffe, O.; Kudisch, B. J.; X.Y.Zhu. Trap States in Lead Iodide Perovskites. *J. Am. Chem. Soc.* **2015,** *137*, 2089-2096.

(71) Deschler, F.; Price, M.; Pathak, S.; Klintberg, L. E.; Jarausch, D.-D.; Higler, R.; Huttner, S.; Leijtens, T.; Stranks, S. D.; Snaith, H. J.; et al. High Photoluminescence Efficiency and Optically Pumped Lasing in Soulution-Processed Mixed Halide Perovskite Semiconductors. *J. Phys. Chem. Lett.* **2014,** *5*, 1421-1426.

(72) Chen, K.; Barker, A. J.; Morgan, F. L. C.; Halptert, J. E.; Hodgkiss, J. M. The Effect of Carrier Thermalization Dynamics on Light Emission and Amplification in Organometal Halide Perovskites. *J. Phys. Chem. Lett.* **2015,** *6*, 153-158.

(73) Gong, T.; Nighan, W. L.; Fauchet, P. M. Hot-Carrier Coulomb Effects in GaAs Investigated by Femtosecond Spectroscopy around the Band Edge. *Appl. Phys. Lett.* **1990,** *57*, 2713-2715.

(74) Fu, J.; Xu, Q.; Han, G.; Wu, B.; Huan, C. H. A.; Leek, M. L.; Sum, T. C. Hot Carrier Cooling Mechanisms in Halide Perovskites. *Nat. Commun.* **2017,** *8*, 1300.

(75) Ponseca, C. S.; Savenije, T. J.; Abdellah, M.; Zheng, K.; Yartsev, A.; Pascher, T.; Harlang, T.; Chabera, P.; Pullerits, T.; Stepanov, A.; et al. Organometal Halide Perovskite Solar Cells Rationalized: Ultrafast Charge Generation, High and Microsecond-Long Balanced Mobilities, and Slow Recombination. *J. Am. Chem. Soc.* **2014,** *136*, 5189-5192.

(76) Stamplecoskie, K. G.; Manser, J. S.; Kamat, P. V. Dual Nature of the Excited State in Organic-Inorganic Lead Halide Perovskites. *Energy Environ. Sci.* **2015,** *8*, 208-215.

(77) Aspnes, D. E. Recombination at Semiconductor Surfaces and Interfaces. *Surf. Sci.* **1983,** *132*, 406-421.

(78) Ziang, X.; Shifeng, L.; Laixiang, Q.; Shuping, P.; Wei, W.; Yu, Y.; Li, Y.; Zhijian, C.; Shufeng, W.; Honglin, D.; et al. Refractive Index and Extinction Coefficient of CH3NH3PbI3 Studied by Spectroscopic Ellipsometry. *Opt. Mater. Express* **2014,** *5*, 29-43.

(79) Yang, Y.; Ostrowski, D. P.; France, R. M.; Zhu, K.; van de Lagemaat, J.; Luther, J. M.; Beard, M. C. Observation of a Hot-Phonon Bottleneck in Lead-Iodide Perovskites. *Nat. Photonics* **2016,** *10*, 53-59.

(80) Yang, J.; Wen, X.; Xia, H.; Sheng, R.; Ma, Q.; Kim, J.; Tapping, P.; Harada, T.; Kee, T. W.; Huang, F.; et al. Acoustic-Optical Phonon up-Conversion and Hot-Phonon Bottleneck in Lead-Halide Perovskites. *Nat. Commun.* **2017,** *8*, 14120.

(81) Yang, Y.; Yan, Y.; Yang, M.; Choi, S.; Zhu, K.; Luther, J. M.; Beard, M. C. Low Surface Recombination Velocity in Solution-Grown $CH_3NH_3PbBr_3$ Perovskite Single Crystal. *Nat. Commun.* **2015,** *6:7961*.

(82) Reid, O. G.; Yang, M.; Kopidakis, N.; Zhu, K.; Rumbles, G. Grain-Size-Limited Mobility in Methylammonium Lead Iodide Perovskite Thin Films. *ACS Energy Lett.* **2016,** *1*, 561-565.

(83) Grancini, G.; Viola, D.; Gandini, M.; Altamura, D.; Pogna, E. A. A.; D'Innocenzo, V.; Bargigia, I.; Giannini, C.; Cerullo, G.; Petrozza, A. Lattice Distortions Drive Electron–Hole Correlation within Micrometer-Size Lead-Iodide Perovskite Crystals. *ACS Energy Lett.* **2016,** *2*, 265-269.

(84) Grumstrup, E. M.; Gabriel, M. M.; Cating, E. M.; Pinion, C. W.; Christesen, J. D.; Kirschbrown, J. R.; Vallorz, E. L.; Cahoon, J. F.; Papanikolas, J. M. Ultrafast Carrier Dynamics in Individual Silicon Nanowires: Characterization of Diameter-Dependent Carrier Lifetime and Surface Recombination with Pump-Probe Microscopy. *J. Phys. Chem. C* **2014,** *118*, 8634-8640.

(85) Smith, L. M.; Wake, D. R.; Wolfe, J. P.; Levi, D.; Klein, M. V.; Klem, J.; Henderson, T.; Morkoç, H. Picosecond Imaging of Photoexcited Carriers in Quantum Wells: Anomalous Lateral Confinement at High Densities. *Phys. Rev. B* **1988,** *38*, 5788-5791.

(86) Stewart, R. J.; Grieco, C.; Larsen, A. V.; Maier, J. J.; Asbury, J. B. Approaching Bulk Carrier Dynamics in Organo-Halide Perovskite Nanocrystalline Films by Surface Passivation. *J. Phys. Chem. Lett.* **2016,** *7*, 1148-1153.

(87) Savenije, T. J.; Ferguson, A. J.; Kopidakis, N.; Rumbles, G. Revealing the Dynamics of Charge Carriers in Polymer:Fullerene Blends Using Photoinduced Time-Resolved Microwave Conductivity. *J. Phys. Chem. C* **2013,** *117*, 24085-24103.

(88) Chen, Y.; Yi, H. T.; Wu, X.; Haroldson, R.; Gartstein, Y. N.; Rodionov, Y. I.; Tikhonov, K. S.; Zakhidov, A.; Zhu, X. Y.; Podzorov, V. Extended Carrier Lifetimes and Diffusion in Hybrid Perovskites Revealed by Hall Effect and Photoconductivity Measurements. *Nat. Commun.* **2016,** *7*, 12253.

(89) S. Chapman, T. G. C. *Mathematical Theory of Non-Uniform Gases*. 3rd ed.; Cambridge University Press: 1970.

(90) Fletcher, N. H. The High Current Limit for Semiconductor Junction Devices. *Proceedings of the IRE* **1957,** *45*, 862-872.

(91) Akiyama, H.; Matsusue, T.; Sakaki, H. Carrier Scattering and Excitonic Effects on Electron-Hole-Pair Diffusion in Nondoped and P -Type-Modulation-Doped GaAs/Al(X)Ga(1-X)as Quantum-Well Structures. *Phys. Rev. B* **1994,** *49*, 14523-14530.

(92) Zhu, D. X.; Dubovitsky, S.; Steier, W. H.; Burger, J.; Tishinin, D.; Uppal, K.; Dapkus, P. D. Ambipolar Diffusion Coefficient and Carrier Lifetime in a Compressively Strained InGaAsP Multiple Quantum Well Device. *Appl. Phys. Lett.* **1997,** *71*, 647-649.

(93) Frost, J. M.; Butler, K. T.; Brivio, F.; Hendon, C. H.; van Schilfgaarde, M.; Walsh, A. Atomistic Origins of High-Performance in Hybrid Halide Perovskite Solar Cells. *Nano Lett.* **2014,** *14*, 2584-2590.

(94) Giorgi, G.; Fujisawa, J.-I.; Segawa, H.; Yamashita, K. Small Photocarrier Effective Masses Featuring Ambipolar Transport in Methylammonium Lead Iodide Perovskite: A Density Functional Analysis. *J. Phys. Chem. Lett.* **2013,** *4*, 4213-4216.

(95) Savenije, T. J.; Ponseca, C. S.; Kunneman, L.; Abdellah, M.; Zheng, K.; Tian, Y.; Zhu, Q.; Canton, S. E.; Scheblykin, I. G.; Pullerits, T.; et al. Thermally Activated Exciton

Dissociation and Recombination Control the Carrier Dynamics in Organometal Halide Perovskite. *J. Phys. Chem. Lett.* **2014,** *5*, 2189-2194.

(96) Zhu, H.; Miyata, K.; Fu, Y.; Wang, J.; Joshi, P. P.; Niesner, D.; Williams, K. W.; Jin, S.; Zhu, X.-Y. Screening in Crystalline Liquids Protects Energetic Carriers in Hybrid Perovskites. *Science* **2016,** *353*, 1409-1413.

(97) Silard, A. P.; Duta, M. J. Majority Carrier Diffusion Coefficients in Degenerately Doped Silicon. *J. Appl. Phys.* **1987,** *62*, 3809-3812.

(98) Yakunin, S.; Sytnyk, M.; Kriegner, D.; Shrestha, S.; Richter, M.; Matt, G. J.; Azimi, H.; Brabec, C. J.; Stangl, J.; Kovalenko, M. V.; et al. Detection of X-Ray Photons by Solution-Processed Lead Halide Perovskites. *Nat. Photonics* **2015,** *9*, 444-449.

(99) Beal, R. E.; Slotcavage, D. J.; Leijtens, T.; Bowring, A. R.; Belisle, R. A.; Nguyen, W. H.; Burkhard, G. F.; Hoke, E. T.; McGehee, M. D. Cesium Lead Halide Perovskites with Improved Stability for Tandem Solar Cells. *J. Phys. Chem. Lett.* **2016,** *7*, 746-51.

(100) Akbulatov, A. F.; Luchkin, S. Y.; Frolova, L. A.; Dremova, N. N.; Gerasimov, K. L.; Zhidkov, I. S.; Anokhin, D. V.; Kurmaev, E. Z.; Stevenson, K. J.; Troshin, P. A. Probing the Intrinsic Thermal and Photochemical Stability of Hybrid and Inorganic Lead Halide Perovskites. *J. Phys. Chem. Lett.* **2017,** *8*, 1211-1218.

(101) Dastidar, S.; Li, S.; Smolin, S. Y.; Baxter, J. B.; Fafarman, A. T. Slow Electron–Hole Recombination in Lead Iodide Perovskites Does Not Require a Molecular Dipole. *ACS Energy Lett.* **2017,** *2*, 2239-2244.

(102) Niezgoda, J. S.; Foley, B. J.; Chen, A. Z.; Choi, J. J. Improved Charge Collection in Highly Efficient $CsPbBrI_2$ Solar Cells with Light-Induced Dealloying. *ACS Energy Lett.* **2017,** *2*, 1043-1049.

(103) Nam, J. K.; Chai, S. U.; Cha, W.; Choi, Y. J.; Kim, W.; Jung, M. S.; Kwon, J.; Kim, D.; Park, J. H. Potassium Incorporation for Enhanced Performance and Stability of Fully Inorganic Cesium Lead Halide Perovskite Solar Cells. *Nano Lett.* **2017,** *17*, 2028-2033.

(104) Frohlich, H. Introduction to the Theory of the Polaron. In *Polarons and Excitons*, Kuper, C. G.; Whitfield, G. D., Eds. Plenium Press: New York, 1962; pp 1-22.

(105) Galkowski, K.; Mitioglu, A.; Miyata, A.; Plochocka, P.; Portugall, O.; Eperon, G. E.; Wang, J. T.-W.; Stergiopoulos, T.; Stranks, S. D.; Snaith, H. J.; et al. Determination of the Exciton Binding Energy and Effective Masses for Methylammonium and Formamidinium Lead Tri-Halide Perovskite Semiconductors. *Energy Environ. Sci.* **2016,** *9*, 962-970.

(106) Sharma, V.; Aharon, S.; Gdor, I.; Yang, C.; Etgar, L.; Ruhman, S. New Insights into Exciton Binding and Relaxation from High Time Resolution Ultrafast Spectroscopy of $CH_3NH_3PbI_3$ and $CH_3NH_3PbBr_3$ Films. *J. Mater. Chem. A* **2016,** *4*, 3546-3553.

(107) Katsidis, C. C.; Siapkas, D. I. General Transfer-Matrix Method for Optical Multilayer Systems with Coherent, Partially Coherent, and Incoherent Interference. *Appl. Opt.* **2002,** *41*, 3978-3987.

(108) Mitsas, C. L.; Siapkas, D. I. Generalized Matrix Method for Analysis of Coherent and Incoherent Reflectance and Transmittance of Multilayer Structures with Rough Surfaces, Interfaces, and Finite Substrates. *Appl. Opt.* **1995,** *34*, 1678-1683.

(109) Herz, L. M. Charge-Carrier Mobilities in Metal Halide Perovskites: Fundamental Mechanisms and Limits. *ACS Energy Lett.* **2017,** *2*, 1539-1548.

(110) Miyata, K.; Meggiolaro, D.; Trinh, M. T.; Joshi, P. P.; Mosconi, E.; Jones, S. C.; De Angelis, F.; Zhu, X.-Y. Large Polarons in Lead Halide Perovskites. *Sci. Adv.* **2017,** *3*.

(111) Frost, J. M. Calculating Polaron Mobility in Halide Perovskites. *Phys. Rev. B* **2017,** *96*, 195202.

(112) Emin, D. Optical Properties of Large and Small Polarons and Bipolarons. *Phys. Rev. B* **1993,** *48*, 13691-13702.

(113) Sendner, M.; Nayak, P. K.; Egger, D. A.; Beck, S.; Muller, C.; Epding, B.; Kowalsky, W.; Kronik, L.; Snaith, H. J.; Pucci, A.; et al. Optical Phonons in Methylammonium Lead Halide Perovskites and Implications for Charge Transport. *Mater. Horizons* **2016,** *3*, 613-620.

(114) Karakus, M.; Jensen, S. A.; D'Angelo, F.; Turchinovich, D.; Bonn, M.; Cánovas, E. Phonon–Electron Scattering Limits Free Charge Mobility in Methylammonium Lead Iodide Perovskites. *J. Phys. Chem. Lett.* **2015,** *6*, 4991-4996.

(115) Miyata, A.; Mitioglu, A.; Plochocka, P.; Portugall, O.; Wang, J. T.-W.; Stranks, S. D.; Snaith, H. J.; Nicholas, R. J. Direct Measurement of the Exciton Binding Energy and Effective Masses for Charge Carriers in Organic-Inorganic Tri-Halide Perovskites. *Nat. Phys.* **2015,** *11*, 582-587.

(116) Tanaka, K.; Takahashi, T.; Ban, T.; Kondo, T.; Uchida, K.; Miura, N. Comparative Study on the Excitons in Lead-Halide-Based Perovskite-Type Crystals $CH_3NH_3PbBr_3$ $CH_3NH_3PbI_3$. *Solid State Commun.* **2003,** *127*, 619-623.

(117) Yang, Z.; Surrente, A.; Galkowski, K.; Miyata, A.; Portugall, O.; Sutton, R. J.; Haghighirad, A. A.; Snaith, H. J.; Maude, D. K.; Plochocka, P.; et al. Impact of the Halide Cage on the Electronic Properties of Fully Inorganic Cesium Lead Halide Perovskites. *ACS Energy Lett.* **2017,** *2*, 1621-1627.

(118) Madelung, O. *Semiconductors: Data Handbook.* 3rd ed.; Springer - Verlag Berlin Heidelberg: 2004.

(119) Fu, Y.; Rea, M. T.; Chen, J.; Morrow, D. J.; Hautzinger, M. P.; Zhao, Y.; Pan, D.; Manger, L. H.; Wright, J. C.; Goldsmith, R. H.; et al. Selective Stabilization and Photophysical Properties of Metastable Perovskite Polymorphs of $CsPbI_3$ in Thin Films. *Chem. Mater.* **2017,** *29*, 8385-8394.

(120) Neukirch, A. J.; Nie, W.; Blancon, J.-C.; Appavoo, K.; Tsai, H.; Sfeir, M. Y.; Katan, C.; Pedesseau, L.; Even, J.; Crochet, J. J.; et al. Polaron Stabilization by Cooperative Lattice Distortion and Cation Rotations in Hybrid Perovskite Materials. *Nano Lett.* **2016,** *16*, 3809-3816.

(121) Smilga, A. V. On the Polaron Mass at Finite Temperatures. *J. Phys. Condens. Matter* **1991,** *3*, 915.

(122) Ahrenkiel, R. K. Studies of the Polaron Mobility in Agbr at High Temperatures. *Phys. Rev.* **1969,** *180*, 859-863.

(123) Bonn, M.; Miyata, K.; Hendry, E.; Zhu, X. Y. Role of Dielectric Drag in Polaron Mobility in Lead Halide Perovskites. *ACS Energy Lett.* **2017,** *2*, 2555-2562.

(124) Egger, D. A.; Bera, A.; Cahen, D.; Hodes, G.; Kirchartz, T.; Kronik, L.; Lovrincic, R.; Rappe, A. M.; Reichman, D. R.; Yaffe, O. What Remains Unexplained About the Properties of Halide Perovskites? *Adv. Mater.* **2018**, 1800691.

(125) Guerra, J. A.; Tejada, A.; Korte, L.; Kegelmann, L.; Töfflinger, J. A.; Albrecht, S.; Rech, B.; Weingärtner, R. Determination of the Complex Refractive Index and Optical Bandgap of CH3NH3PbI3 Thin Films. *J. Appl. Phys.* **2017,** *121*, 173104.

(126) Riffe, D. M. Temperature Dependence of Silicon Carrier Effective Masses with Application to Femtosecond Reflectivity Measurements. *J. Opt. Soc. Am. B* **2002,** *19*, 1092-1100.

(127) Nah, S.; Spokoyny, B. M.; Soe, C. M. M.; Stoumpos, C. C.; Kanatzidis, M. G.; Harel, E. Ultrafast Imaging of Carrier Cooling in Metal Halide Perovskite Thin Films. *Nano Lett.* **2018,** *18*, 1044-1048.

(128) Hill, A. H.; Kennedy, C. L.; Massaro, E. S.; Grumstrup, E. M. Perovskite Carrier Transport: Disentangling the Impacts of Effective Mass and Scattering Time through Microscopic Optical Detection. *J. Phys. Chem. Lett.* **2018**, 2808-2813.

(129) Zhu, H.; Miyata, K.; Fu, Y.; Wang, J.; Joshi, P. P.; Niesner, D.; Williams, K. W.; Jin, S.; Zhu, X. Y. Screening in Crystalline Liquids Protects Energetic Carriers in Hybrid Perovskites. *Science* **2016,** *353*, 1409-1413.

(130) Elbaz, G. A.; Straus, D. B.; Semonin, O. E.; Hull, T. D.; Paley, D. W.; Kim, P.; Owen, J. S.; Kagan, C. R.; Roy, X. Unbalanced Hole and Electron Diffusion in Lead Bromide Perovskites. *Nano Lett.* **2017,** *17*, 1727-1732.

(131) Wei, H.; Fang, Y.; Mulligan, P.; Chuirazzi, W.; Fang, H.-H.; Wang, C.; Ecker, B. R.; Gao, Y.; Loi, M. A.; Cao, L.; et al. Sensitive X-Ray Detectors Made of Methylammonium Lead Tribromide Perovskite Single Crystals. *Nat. Photonics* **2016,** *10*, 333.

(132) Brennan, M. C.; Herr, J. E.; Nguyen-Beck, T. S.; Zinna, J.; Draguta, S.; Rouvimov, S.; Parkhill, J.; Kuno, M. Origin of the Size-Dependent Stokes Shift in CsPbBr3 Perovskite Nanocrystals. *J. Am. Chem. Soc.* **2017,** *139*, 12201-12208.

(133) Wang, L.; Wang, K.; Zou, B. Pressure-Induced Structural and Optical Properties of Organometal Halide Perovskite-Based Formamidinium Lead Bromide. *J. Phys. Chem. Lett.* **2016,** *7*, 2556-2562.

(134) Stranks, S. D.; Burlakov, V. M.; Leijtens, T.; Ball, J. M.; Goriely, A.; Snaith, H. J. Recombination Kinetics in Organic-Inorganic Perovskites: Excitons, Free Charge, and Subgap States. *Phys. Rev. Appl.* **2014,** *2*, 034007.

(135) Zhao, T.; Shi, W.; Xi, J.; Wang, D.; Shuai, Z. Intrinsic and Extrinsic Charge Transport in $CH_3NH_3PbI_3$ Perovskites Predicted from First-Principles. *Sci. Rep.* **2016,** *6*, 19968.

(136) Endres, J.; Egger, D. A.; Kulbak, M.; Kerner, R. A.; Zhao, L.; Silver, S. H.; Hodes, G.; Rand, B. P.; Cahen, D.; Kronik, L.; et al. Valence and Conduction Band Densities of States of Metal Halide Perovskites: A Combined Experimental–Theoretical Study. *J. Phys. Chem. Lett.* **2016,** *7*, 2722-2729.

(137) Huang, X.; Paudel, T.; Dowben, P.; Dong, S.; Tsymbal, E. Electronic Structure and Stability of the $CH_3NH_3PbBr_3$ (001) Surface. *Phys. Rev. B* **2016,** *94*.

(138) Amat, A.; Mosconi, E.; Ronca, E.; Quarti, C.; Umari, P.; Nazeeruddin, M. K.; Grätzel, M.; De Angelis, F. Cation-Induced Band-Gap Tuning in Organohalide Perovskites: Interplay of Spin–Orbit Coupling and Octahedra Tilting. *Nano Lett.* **2014,** *14*, 3608-3616.

(139) Stoumpos, C. C.; Kanatzidis, M. G. The Renaissance of Halide Perovskites and Their Evolution as Emerging Semiconductors. *Accounts of Chemical Research* **2015,** *48*, 2791-2802.

(140) Manser, J. S.; Christians, J. A.; Kamat, P. V. Intriguing Optoelectronic Properties of Metal Halide Perovskites. *Chem. Rev.* **2016,** *116*, 12956-13008.

(141) Beimborn, J. C.; Hall, L. M. G.; Tongying, P.; Dukovic, G.; Weber, J. M. Pressure Response of Photoluminescence in Cesium Lead Iodide Perovskite Nanocrystals. *J. Phys. Chem. C* **2018,** *122*, 11024-11030.

(142) Singh, J. *Excitation Energy Transfer Processes in Condensed Matter: Theory and Applications*. Plenum Press: New York, 1994.

(143) Tavakoli, M. M.; Gu, L.; Gao, Y.; Reckmeier, C.; He, J.; Rogach, A. L.; Yao, Y.; Fan, Z. Fabrication of Efficient Planar Perovskite Solar Cells Using a One-Step Chemical Vapor Deposition Method. *Sci. Rep.* **2015,** *5*, 14083.

(144) Wang, Y.; Guan, X.; Li, D.; Cheng, H.-C.; Duan, X.; Lin, Z.; Duan, X. Chemical Vapor Deposition Growth of Single-Crystalline Cesium Lead Halide Microplatelets and Heterostructures for Optoelectronic Applications. *Nano Research* **2017,** *10*, 1223-1233.

(145) Brivio, F.; Frost, J. M.; Skelton, J. M.; Jackson, A. J.; Weber, O. J.; Weller, M. T.; Goñi, A. R.; Leguy, A. M. A.; Barnes, P. R. F.; Walsh, A. Lattice Dynamics and Vibrational Spectra of the Orthorhombic, Tetragonal, and Cubic Phases of Methylammonium Lead Iodide. *Phys. Rev. B* **2015,** *92*, 144308.